

# An observational study of dust nucleation in Mira (*o* Ceti):

## I. Variable features of AlO and other Al-bearing species

T. Kamiński<sup>1</sup>, K.T. Wong<sup>2</sup>, M. R. Schmidt<sup>3</sup>, H.S.P. Müller<sup>4</sup>, C.A. Gottlieb<sup>5</sup>, I. Cherchneff<sup>6</sup>,  
K.M. Menten<sup>2</sup>, D. Keller<sup>2</sup>, S. Brünken<sup>4</sup>, J.M. Winters<sup>7</sup>, N.A. Patel<sup>5</sup>

<sup>1</sup> ESO, Alonso de Cordova 3107, Vitacura, Casilla 19001, Santiago, Chile, e-mail: tkaminsk@eso.org,

<sup>2</sup> Max-Planck-Institut für Radioastronomie, Auf dem Hügel 69, 53121 Bonn, Germany

<sup>3</sup> Nicolaus Copernicus Astronomical Center, Polish Academy of Sciences, Rabiańska 8, 87-100 Toruń

<sup>4</sup> I. Physikalisches Institut, Zülpiher Strasse 77, 50937 Köln, Germany

<sup>5</sup> Harvard-Smithsonian Center for Astrophysics, 60 Garden Street, Cambridge, MA, USA

<sup>6</sup> Departement Physik, Universität Basel, Klingelbergstrasse 82, 4056, Basel, Switzerland

<sup>7</sup> IRAM, 300 rue de la Piscine, Domaine Universitaire de Grenoble, 38406, St. Martin d'Hères, France

Received; accepted

### ABSTRACT

**Context.** Dust is efficiently produced by cool giant stars, but the condensation of inorganic dust is poorly understood. Observations of key aluminum bearing molecules around evolved stars has allowed us to investigate the nucleation of alumina ( $\text{Al}_2\text{O}_3$ ) dust in the gas.

**Aims.** Identify and characterize aluminum bearing species in the circumstellar gas of Mira (*o* Ceti) in order to elucidate their role in the production of  $\text{Al}_2\text{O}_3$  dust.

**Methods.** Multiepoch spectral line observations at (sub-)millimeter, far-infrared, and optical wavelengths including: maps with ALMA which probe the gas distribution in the immediate vicinity of the star at  $\sim 30$  mas; observations with ALMA, APEX, and *Herschel* in 2013–2015 for studying cycle and inter-cycle variability of the rotational lines of Al bearing molecules; optical records as far back as 1965 to examine variations in electronic transitions over time spans of days to decades; and velocity measurements and excitation analysis of the spectral features which constrain the physical parameters of the gas.

**Results.** Three diatomic molecules AlO, AlOH, and AlH, and atomic Al I are the main observable aluminum species in Mira, although a significant fraction of aluminum might reside in other species that have not yet been identified. Strong irregular variability in the (sub-)millimeter and optical features of AlO (possibly the direct precursor of  $\text{Al}_2\text{O}_3$ ) indicates substantial changes in the excitation conditions, or varying abundance that is likely related to shocks in the star. The inhomogeneous distribution of AlO might influence the spatial and temporal characteristics of dust production.

**Conclusions.** We are unable to quantitatively trace aluminum depletion from the gas, but the rich observational material constrains time dependent chemical networks. Future improvements should include spectroscopic characterization of higher aluminum oxides, coordinated observations of dust and gas species at different variability phases, and tools to derive abundances in shock excited gas.

**Key words.** Stars: mass-loss - Stars: AGB and post-AGB - circumstellar matter - Submillimeter: stars - Astrochemistry

## 1. Introduction

Evolved stars are primary producers of dust in galaxies. They are sources of both carbonaceous dust, originating mainly from carbon-rich asymptotic giant branch (AGB) stars, and inorganic dust, formed in oxygen-rich environments of M-type AGB stars and their massive analogs – red supergiants. Despite the important role of dust in a broad range of astrophysical phenomena, the formation of stardust is poorly understood. In general, dust formation proceeds along a chain of chemical reactions starting from small gas-phase molecules which form successively larger species (Cherchneff 2013). These large molecules grow, form clusters, and end as macroscopic complexes. The formation of inorganic (silicate and alumina) dust is likely to start from oxides. Because the nucleation occurs at rather high temperatures ( $\sim 1100$ – $1700$  K), these oxides must be refractory. After ruling out more abundant elements (Si, Fe, and Mg) and under the assumption of thermodynamic equilibrium (TE), it was proposed that oxides of titanium ( $\text{TiO}$ ,  $\text{TiO}_2$ ) and of aluminum

(AlO) are the gas-phase species that can potentially initiate the formation of critical clusters (seeds) in O-rich environments (Gail & Sedlmayr 1998; Jeong et al. 2003). The widely known “silicates”, which determine the observed properties of warm and cold dust in circumstellar shells, are important for grain growth at lower temperatures (a few hundred K) and condense on the seeds formed at higher temperatures. This TE prediction, however, is challenged by strong non-equilibrium effects characterizing the dynamic atmospheres of AGB stars where the condensation takes place (Cherchneff 2006). The importance of Ti and Al oxides in grain formation is reinforced by meteorite studies, which show that these oxides are present in presolar grains (i.e. grains thought to represent pristine stardust, Nittler et al. 2008). The meteoritic studies demonstrate that aluminum oxides are at the core of a few silicate grains originating from AGB stars, but it is definitely not a common feature among those grains (e.g. Vollmer et al. 2006; Nguyen et al. 2016).

Most theoretical studies of the dust condensation in circumstellar material assumed chemical equilibrium in the gas (e.g. Sharp & Huebner 1990). Some alternative chemical stud-

Send offprint requests to: T. Kamiński

ies of the circumstellar envelopes went beyond this assumption and more realistic non-equilibrium models paved the way toward a better understanding of circumstellar chemistry. They include the presence of shocks which substantially change our view of the chemistry in the envelopes of pulsating giants (e.g. Willacy & Cherchneff 1998; Cherchneff 2006). Recent models highlight the chief role of Al oxides as a separate form of warm dust in AGB stars (Gobrecht et al. 2016). An observational verification of the nucleation and chemical reactions leading to the formation of critical clusters is still very much desired. With modern instruments and by combining data from different wavelength regimes, such a verification is now possible (e.g. Kamiński et al. 2013,a).

Here, we make an attempt to trace Al-bearing species in the gas phase around Mira in different phases and different pulsation cycles. Using techniques of mainly optical and submillimeter-wave (submm) spectroscopy, we investigate the link between these species and the formation of metal-oxide grains. Mira was chosen because of (i) the wealth of optical data that was collected over a long period of time and (ii) relatively high brightness of spectral lines at millimeter (mm) and submm wavelengths. Because in many respects Mira is the prototypical M-type AGB star, understanding Mira has direct implications for understanding the entire class it represents. The numerous studies of dust formation of Mira provide a basis and a rich context for our study, thereby allowing more conclusive interpretations. In this paper – being the first of a series – we focus on aluminum-bearing species and their role in the formation of dust in innermost parts of the Mira’s envelope. The forthcoming papers will investigate the impact of titanium-, silicon-, and iron-bearing species on the nucleation process using similar methods as those presented here.

The paper is organized as follows. In the remainder of Sect. 1, we provide further introductory material on *o* Ceti, structure, chemistry, and dust formation in the envelopes of Mira variables. Next, we present and analyze the observational material in two parts. Sections 2–3 focus on mm/submm and far-infrared (FIR) data, mainly of AlO and AlOH. Section 4 presents visual spectroscopy of *o* Ceti which yields information primarily on AlI, AlO, and AlH. In Sect. 5, results are discussed within the context of the circumstellar chemistry and dust formation.

### 1.1. *o* Ceti

Mira has a well documented history of light variations. The visual magnitude changes by up to  $8^{\text{mag}}$ , i.e. in some maxima Mira is  $\sim 1600$  times brighter than the minima. These light variations are partially caused by changes in the effective temperature of the pulsating photosphere but, even more importantly, the fluxes change owing to variable opacity caused by metal oxides which have strong bands at optical wavelengths (Reid & Goldston 2002). The variable temperature and dynamical processes lead to non-equilibrium chemistry and variable abundances of these oxides (e.g. Cherchneff 2006). Complex dynamics and chemistry are heavily contributing to the spectacular light changes in Miras.

Mira’s companion, Mira B, is likely a white dwarf (but a main-sequence star was also postulated by several authors; see Ireland et al. 2007; Sokoloski & Bildsten 2010, and references therein). At an orbit of radius  $\sim 90$  AU (projected distance  $0''.5$ ) and a period of  $\sim 600$  yr (Ireland et al. 2007), the companion is accreting material from the wind of Mira A (Mohamed & Podsiadlowski 2012). The accretion process gives rise to ultraviolet (UV) and X-ray radiation, including emis-

sion in highly-ionized species, e.g. of N v (Reimers & Cassatella 1985). Because Mira B is embedded in the dusty wind which absorbs most of the energetic photons in the direction of the cool giant (Ireland et al. 2007), the harsh radiation does not affect the inner wind of Mira A (within, say, 10 AU) but may be responsible for dissociation of molecules in the immediate vicinity of Mira B (cf. Nhung et al. 2016). Also, Mira B is not expected to have a significant dynamic influence on the inner wind of Mira A (Matthews et al. 2015).

An important parameter for our analysis is the radius of *o* Ceti. The size of the photosphere of a Mira variable varies considerably with wavelength owing to different dominant sources of opacity (cf. Stewart et al. 2013). Also, the size changes with phase mainly owing to pulsations in the fundamental mode which change the physical extent of the atmosphere (e.g. Woodruff et al. 2004; Ireland et al. 2011). Furthermore, the temperature changes as a combined result of expansion/contraction and the propagation of shock waves, influencing the gas excitation and thus the opacity. Photospheric sizes have been derived by different authors using a myriad of observational techniques. The smallest radius we found in the literature,  $12.19 \pm 0.02$  mas, was determined near the maximum visual light at  $\sim 2 \mu\text{m}$  (Perrin et al. 2004). From *K*-band IR data, a radius of  $14.8 \pm 0.6$  mas was found (Stewart et al. 2013) which is similar to  $14.3$ – $14.4$  mas observed at  $0.94 \mu\text{m}$  (Woodruff et al. 2004; Wittkowski et al. 2016); at shorter wavelengths, near  $0.701 \mu\text{m}$  and  $0.45 \mu\text{m}$ , the continuum source was measured to be a disk of a radius of  $26$ – $28$  mas (Haniff et al. 1992) and  $35 \pm 10$  mas (Labeyrie et al. 1977), respectively. All these values are considerably smaller than the radius of  $47 \pm 7$  mas determined at  $4.93 \mu\text{m}$  and at  $\varphi = 0.2$ – $0.3$  (Stewart et al. 2013). Most recently, also the millimeter photosphere of Mira has been resolved giving a radius of  $R_{\text{mm,ph}} = 23$  mas near visual phase 0.5 (i.e. when the atmosphere is more extended than at maximum) (Vlemmings et al. 2015; Matthews et al. 2015; Wong et al. 2016). Reid & Menten (2007) measured a radius of the radio photosphere at 43 GHz of 26 mas at phase 0.05. Throughout this paper, we adopt  $R_{\star} \equiv 14.4$  mas as the stellar radius and the characteristic distance scale. This is equivalent to  $2.4 \times 10^{13}$  cm or  $331 R_{\odot}$  at the distance of 107 pc to the star (Knapp et al. 2003). The temperature of the star changes within about<sup>1</sup> 2900–3200 K and its bolometric luminosity is of about  $9000 L_{\odot}$  (Woodruff et al. 2004; Perrin et al. 2004).

### 1.2. The atmosphere and circumstellar envelope of Mira

The complex kinematic and dynamical structure of the atmosphere and circumstellar envelope of Mira has a crucial bearing on the analysis and discussion in this work. The complex velocity fields of Mira variables have been studied observationally at optical and infrared wavelengths but the greatest successes were achieved by observations of the infrared ro-vibrational lines of CO (e.g. Hinkle 1978; Hinkle et al. 1984; Nowotny et al. 2010). Theoretical effort has also been done to understand the structure of Mira variables and a number of models have satisfactorily reproduced some observational data (e.g. Ireland et al. 2011; Höfner 2008; Gobrecht et al. 2016). The deepest parts of the atmosphere are dynamically most influenced by the stellar pulsation and the associated shock wave that is created in each cycle. The shock is radiative and ionizing, so that in its wake intense emission lines of high excitation, such as hydrogen recombination lines, are formed. The temperatures within the shock are el-

<sup>1</sup> Arkharov et al. (2005) suggest a range 2200–3000 K.

evated to 35 000 K (Fox et al. 1984). The shock propagates outward and eventually reaches the upper atmosphere. Because a large part of the shock's energy is radiated away and because of the expansion, the shock slows down in progressively higher parts of the atmosphere. Its influence on the velocity field can be traced up to approximately  $3-4 R_\star$ , where its velocity is a few  $\text{km s}^{-1}$ . This region, which we call hereafter the *extended atmosphere*, shows the highest temporal variations in the kinematics of gas. The radial velocity of high-excitation lines, such as those of the  $\Delta v = 3$  band of CO, vary with a full amplitude of  $20-30 \text{ km s}^{-1}$  in *o* Ceti. The motions include infall with velocities of up to  $13 \text{ km s}^{-1}$ . Alumina dust is observed in Mira stars at  $\sim 2 R_\star$ , i.e. within this dynamically active region. The part of the extended atmosphere up to  $\sim 2 R_\star$  is known for a high-opacity molecular layer of CO and  $\text{H}_2\text{O}$  which has been resolved in NIR interferometric observations (e.g. Perrin et al. 2004; Wittkowski et al. 2016). It is also the region where the variable SiO masers are observed. In Mira, the maser rings are of radii of  $2.0-2.8 R_\star$  (Cotton et al. 2006; Reid & Menten 2007).

Above the extended atmosphere, starting at about  $4 R_\star$ , is the zone of silicate-dust formation that is probably somewhat affected by the outward and inward movements. Once (silicate) dust of high opacity is formed, the radiation pressure from the star can accelerate the envelope to form a steady wind. It is often assumed that above  $10 R_\star$  the outflow is fully accelerated. No short-term velocity changes are expected for features arising in the wind.

These three regions are characterized by kinetic gas temperatures of about 2000–4500 K (photosphere and just above it), 800–1200 K (the silicate dust formation zone), and  $\lesssim 500$  K in the extended wind (cf. Nowotny et al. 2010). At these temperatures, the two inner regions are warm enough to cool down radiatively through electronic transitions of neutral atoms and ions and through electronic and rovibrational bands of refractory molecules. The material in the wind is expected to cool down through low-excitation emission lines in the optical, especially in resonance lines of alkali metals and pure rotational lines of molecules.

*Absorption* lines in *o* Ceti change their radial velocity by up to  $12 \text{ km s}^{-1}$  in the optical (Joy 1954)<sup>2</sup>, and are displaced symmetrically around the stellar (center-of-mass) velocity by  $24 \text{ km s}^{-1}$  in the infrared (Hinkle et al. 1984). Optical lines are thought to generally trace higher parts of the stellar atmosphere compared to infrared lines of similar excitation, an effect caused by increased continuum opacity at optical wavelengths (through the Rayleigh scattering; Willson et al. 1982). *Emission* lines, mainly optical ones, vary in position as well but they are always shifted toward the blue, by as much as  $16-18 \text{ km s}^{-1}$  (Joy 1926, 1954). They are thought to be excited by and located close to a shock front (Willson et al. 1982; Richter & Wood 2001; Richter et al. 2003). Because the front always moves outwards, the lines appear only at negative (or zero) velocities with respect to the star, i.e. they are always blueshifted. The shock is directly responsible for a temperature inversion which allows us to see emission features even when the gas is seen against the stellar disk.

The wind of Mira has been extensively observed in the classical pure rotational lines of CO (e.g. Ryde & Schöier 2001; Ramstedt et al. 2014; Nhung et al. 2016). The terminal veloc-

ity of the wind,  $v_\infty$ , is usually quoted as about  $5 \text{ km s}^{-1}$ , but velocities as low as  $2.5 \text{ km s}^{-1}$  have been suggested in the literature (Ryde & Schöier 2001). From observations of multiple lines of CO up to  $J_{\text{up}}=16$ , we constructed a model of the Mira's wind which strongly disfavors the low terminal velocity and here we adopt  $v_\infty=5 \text{ km s}^{-1}$ , equivalent to  $1.5 R_\star \text{ yr}^{-1}$ . On the basis of the same model and literature data (e.g. Gerard & Bourgois 1993), we also adopt the stellar center-of-mass velocity of  $V_{\text{LSR,sys}}=46.8 \pm 0.5 \text{ km s}^{-1}$  in the local standard of rest, which is equivalent to  $V_{h,\text{sys}}=57.0 \text{ km s}^{-1}$  in the heliocentric rest frame.

The mass-loss rate of *o* Ceti,  $\sim 2 \times 10^{-7} M_\odot \text{ yr}^{-1}$  (Ryde & Schöier 2001; Young 1995), is typical for Mira stars but the distribution of rates has a large scatter so that some sources can differ by more than one order of magnitude above and below the value derived for *o* Ceti (Young 1995).

### 1.3. Dust formation in *o* Ceti and other Mira variables

A relation between dust formation and pulsation cycle of Mira stars is not well established – it is unclear whether dust formation occurs within certain phases of a given cycle or takes place independent of it. In general, individual cycles are characterized by somewhat different amplitude and shape of the light curve and there is a possibility that the rate of dust production may change from cycle to cycle. Temporal variations in the emission of the innermost dust shells have been reported in the infrared for some objects, including *o* Ceti (see e.g. Lopez et al. 1997; Lobel et al. 2000). They suggest that dust production itself may indeed be variable. For the Mira variable IK Tau, theoretical models show that dust formation is time-dependent and occurs at specific pulsation phases in the shocked upper atmosphere, i.e.  $\varphi=0.8-1.0$  for alumina and  $\varphi=0.5-1.0$  for silicates (Gobrecht et al. 2016).

Mira variables have been categorized depending on the type of spectral features observed at mid-infrared (MIR) wavelengths. These include: (I) a broad feature of  $\text{Al}_2\text{O}_3$  (corundum), (II) a mix of alumina and silicate features, or (III) a dominant silicate feature (Lorenz-Martins & Pompeia 2000; Little-Marenin & Little 1990). These three types are thought to be an evolutionary sequence, where objects with alumina-dominated dust are less evolved stars with dust production initiated recently, and group III has a long history of dust production. [More recent studies suggest that the three groups reflect different regimes of mass-loss rates, with group I representing very low rates (e.g. Karovicova et al. 2013).] *o*-Ceti's MIR spectrum is dominated by the silicate feature (e.g. Lobel et al. 2000), placing it in the third group, i.e. among the most evolved objects in the sequence. It is thought that this group of stars, including Mira, forms alumina dust at high temperatures close to the star ( $2-3.5 R_\star$ ,  $\sim 30-50 \text{ mas}$  in *o* Ceti, Bester et al. 1991; Degiacomi et al. 1992; Lopez et al. 1997) but most of the mass of dust is built up farther from the photosphere, in the form of silicate grains ( $\geq 200 \text{ mas}$  in *o* Ceti); the silicate dust may partially form on the seeds provided by the  $\text{Al}_2\text{O}_3$  clusters. Therefore, although their MIR spectra are dominated by the silicate feature, Mira variables are still thought to be efficient producers of alumina-based solids. This is also consistent with popular hypotheses on the dust-nucleation sequence in evolved stars. It has been confirmed observationally by infrared interferometric techniques that the alumina dust forms closer to the photosphere than silicates (e.g. Zhao-Geisler et al. 2012; Karovicova et al. 2013). Recent theoretical models agree with those observational findings and show that alumina dust forms at radii  $\lesssim 2 R_\star$  and the silicate dust is present at radii  $\geq 4 R_\star$  (Gobrecht et al. 2016).

<sup>2</sup> Joy (1926) first suggested an amplitude of  $12 \text{ km s}^{-1}$  which however was revoked in his later paper in favor of an amplitude of  $4.5 \text{ km s}^{-1}$ . Measurement presented later in our work, however, support amplitudes above  $4.5 \text{ km s}^{-1}$ .

#### 1.4. Which Al-bearing species are important?

In order to trace the species containing Al in the envelope of Mira, we first identify the most likely carriers on the basis of previous observations of cool circumstellar envelopes and chemical models. Gobrecht et al. (2016) consider Al, AlH, AlO, AlOH, AlO<sub>2</sub>, AlCl, Al<sub>2</sub>, and Al<sub>2</sub>O to be important species for Al gas-phase chemistry. In addition, AlF and AlNC were observed in the carbon star IRC+10216 (Ziurys et al. 1994, 2002), and AlS and AlCN are potentially interesting carriers as well (cf. Tenenbaum & Ziurys 2010). Of these, homonuclear Al<sub>2</sub> is not easily observable. Similarly, the main isomers of AlO<sub>2</sub> and Al<sub>2</sub>O are linear and their rotational lines are not observable. We found no high-resolution spectroscopic studies of gas-phase forms of higher Al oxides that would allow us to identify their spectral features. This poses a serious shortcoming for our current study. Other molecules listed here have been observed at visual (AlH, AlO) or mm/submm (AlO, AlOH, AlCl, AlF, AlNC) wavelengths around cool evolved stars. From these, only the optical electronic bands of AlO have been reported to date in Mira.

Atomic aluminum is present mainly in the stellar photosphere where thermal equilibrium holds. For an effective temperature of 2200–3000 K of Mira, equilibrium calculations indicate that atomic aluminum is mainly in the neutral and singly-ionized forms (cf. Tenenbaum & Ziurys 2010).

Because Mira is thought to be a low-mass star ( $\sim 1 M_{\odot}$ , Ireland et al. 2011), one does not expect the rare unstable isotope of <sup>26</sup>Al to be present in its atmosphere and circumstellar environment (Karakas & Lattanzio 2003). Therefore, no rare isotopologues were targeted in this study.

## 2. Millimeter to FIR observations

In search for the Al-bearing species, we observed Mira in a broad wavelength range, from mm to FIR wavelengths. Additionally, optical observations are presented in Sect. 4.

### 2.1. APEX/FLASH

Mira was observed in 13–14 August 2013 and 30 June–8 July 2014 using the dual-band FLASH+ receiver at APEX. Multiple frequency setups were used with the primary aim to detect rotational transitions of AlO (and lines of CO in the first excited vibrational state). FLASH+ has two frequency units (covering the 345 and 460 GHz atmospheric bands) and separates the upper and lower side bands (USB and LSB), what produces four spectra in a single observation. This allowed us to observe ten different frequency ranges within the 345 GHz and 460 GHz atmospheric windows, each 4 GHz wide, at the spectral resolution of 38 kHz (in the 345 GHz band) and 76 kHz (in the 460 GHz band). Observational details including central frequencies, integration times, rms-noise levels, and exact dates of observations are given in Table A.1 (Appendix A.1).

All observations were performed with a wobbler which was switched by 1'. The data were calibrated with the default APEX pipeline (Polehampton & Hafok 2013) and are here presented in the antenna brightness temperature ( $T_A^*$ ) or converted to main-beam brightness temperature ( $T_{mb}$ ), as indicated in each case. Baselines of low order were subtracted from the spectra. All spectra presented here were smoothed to resolutions which allow more readily presentation.

### 2.2. APEX/HET230

Spectra were also acquired in the 1-mm band with the SHeFI (HET230) instrument at APEX. These observations were obtained between 3 and 23 December 2013 in two setups and were intended to detect (i) two lines of TiO centered at 222.7 GHz (in LSB), and (ii) lines of AlO and vibrationally excited CO, with the band centered at 229.8 GHz (in USB). The second setup was re-observed in 9–12 June 2015. The HET230 instrument produces one single-sideband spectrum. The XFFTS spectrometer produced spectra at a resolution of 76 kHz.

Two frequency ranges, centered on 229.800 GHz and 344.454 GHz, were each observed twice, 20 and 11 months apart with APEX (cf. Table A.1). A detailed technical analysis of the data, summarized in Appendix A.2, have shown that some of the AlO lines covered are variable.

**Herschel/HIFI** In the search for the Al-bearing species, we browsed the archives of the Herschel Space Observatory (*Herschel*) for observations of Mira obtained with the HIFI instrument. Publicly available observations were mostly performed within the HIFISTARS project (PI: V. Bujarrabal), but some additional data were acquired within the Performance-Verification (PV) of HIFI. We used the processed data from the HIFISTARS' User Provided Data Products Release<sup>3</sup> or – in the case of the PV data – the pipeline-processed spectra which were corrected for baseline and converted to  $T_{mb}$  units. Here, we analyze only one spectrum which covers the  $N=29-28$  line of AlO.

### 2.3. ALMA

The most sensitive submm observations of Mira to date are those obtained by ALMA at multiple epochs in 2014 and 2015. The earliest ALMA data for Mira were obtained within the ALMA 2014 Long Baseline Campaign Science Verification (hereafter, SV data) (ALMA Partnership et al. 2015). The data are described in detail in Wong et al. (2016)<sup>4</sup>. One spectrum which covers the AlO  $N=6-5$  line was observed on 29 October and 1 November 2014 in the “continuum mode”, i.e. with a poor spectral resolution of 20.5 km s<sup>-1</sup>. These high angular-resolution observations with a beam of about 34×24 mas are the most detailed observations of Mira to date.

The first ALMA observations at submm frequencies were reported in Ramstedt et al. (2014). They covered two frequency ranges within ALMA Band 7 at about 330.25–334.00 and 342.35–346.09 GHz that included the  $N=9-8$  line of AlO. From the ALMA archive, we extracted the raw data obtained with the 12-m array only and reduced them with the standard pipeline. The observations were obtained twice, on 24 Feb. 2014 and 3 May 2014, in nearly the same frequency setup but with different array configurations resulting in spatial resolutions (synthesized beams) of 1'59×0'48 and 0'51×0'37, respectively, at the frequency of the AlO line. Unlike in Ramstedt et al. (2014), we imaged the data from different dates separately. The flux levels of continuum and line emission differ in both datasets indicating variability at a level above the flux calibration uncertainties. The first dataset was calibrated using observations of the primary flux calibrator, Ganymede, with a model flux accurate to <5%, while the second used the secondary calibrator J0334-401 whose flux is monitored at about 15% accuracy. The calibration of phase and amplitude in the data used for the analysis here were fur-

<sup>3</sup> <http://herschel.esac.esa.int/UserProvidedDataProducts.shtml>

<sup>4</sup> see also [https://casaguides.nrao.edu/index.php?title=ALMA2014\\_L](https://casaguides.nrao.edu/index.php?title=ALMA2014_L)

**Table 1.** Transitions of AIO and AIOH covered by APEX, *Herschel*, and ALMA observations.

Transition $N_{\text{up}} - N_{\text{low}}$	$\langle \nu \rangle^a$ (GHz)	$\Sigma S_i \mu^2$ (D <sup>2</sup> )	$E_u$ (K)	Date of observations	Vis. phase	Telesc.	Beam <sup>b</sup> ( $''$ )	$I(T_{\text{mb}})^c$ (K km s <sup>-1</sup> )	Flux $\pm 1\sigma$ (Jy km s <sup>-1</sup> )
AIO									
6–5	229.67025503	1522.89	38.65	6–23 Dec. 2013	0.5	APEX	27.2	<0.035	<1.02
6–5	229.67025503	1522.89	38.65	29 Oct./1 Nov. 2014	0.5	ALMA	0.029	24591.6 <sup>d</sup>	0.89 $\pm$ 0.02
6–5	229.67025503	1522.89	38.65	9–12 Jun. 2015	0.1	APEX	27.2	0.076	2.21 $\pm$ 0.72
8–7	306.19734234	2030.60	66.20	7–8 Jul. 2014	0.1	APEX	20.4	0.079	2.34 $\pm$ 0.65
9–8	344.45177512	2284.46	82.73	Feb. 2014	0.7	ALMA	0.88	16.79 <sup>d</sup>	1.25 $\pm$ 0.09
9–8	344.45177512	2284.46	82.73	May 2014	0.9	ALMA	0.43	119.28 <sup>d</sup>	2.16 $\pm$ 0.29
9–8	344.45177512	2284.46	82.73	12–15 June 2014	1.0	ALMA	0.33	291.31 <sup>d</sup>	3.05 $\pm$ 0.03
9–8	344.45177512	2284.46	82.73	Aug. 2013/Jul. 2014	0.1/0.1	APEX	18.1	0.114	3.41 $\pm$ 0.81
9–8	344.45177512	2284.46	82.73	21 July 2015	0.2	ALMA	0.15	1838.58 <sup>d</sup>	3.84 $\pm$ 0.02
11–10	420.93832496	2792.05	121.30	13–14 Aug. 2013	0.1	APEX	14.8	0.408	11.8 $\pm$ 3.0
12–11	459.16920150	3040.87	143.33	14 Aug. 2013	0.1	APEX	13.6	<0.140	<4.03
13–12	497.38987615	3300.05	167.20	1–8 Jul. 2014	0.1	APEX	12.5	0.413	11.9 $\pm$ 2.3
29–28	1106.98018793	7362.47	798.08	20 Jul. 2010	0.7	HSO	19.2	0.160	57.1 $\pm$ 19.0
AIOH									
11–10	346.15555028	71.39	99.69	Aug. 2013/Jul. 2014	0.1/0.1	APEX	18.0	0.059	1.77 $\pm$ 0.49
13–12	409.03103805	84.36	137.45	13–14 Aug. 2013	0.1	APEX	15.3	0.105	3.02 $\pm$ 0.97
15–14	471.87557840	97.35	181.23	14 Aug. 2013	0.1	APEX	13.2	0.180	5.18 $\pm$ 1.54
18–17	566.07395655	116.81	258.21	19 Feb. 2010	0.3	HSO	38.3	<0.072	<22.48
21–20	660.17593148	136.28	348.75	20 Jul. 2010	0.7	HSO	32.4	<0.074	<23.10
22–21	691.51905756	142.77	381.93	20 Jul. 2010	0.7	HSO	31.1	<0.128	<39.96
33–32	1035.29846577	214.16	846.08	3 Feb. 2010	0.2	HSO	20.6	<0.275	<85.93
35–34	1097.57173239	227.13	949.93	20 Jul. 2010	0.7	HSO	19.4	0.315	98.4 $\pm$ 22.9

**Notes.** <sup>(a)</sup> Weighted mean frequency of the hyperfine components, i.e.  $\langle \nu \rangle = \Sigma \nu_i S_i / \Sigma S_i$ , where  $S_i$  is the component strength. <sup>(b)</sup> For non-circular beams a geometric mean of the minor and major axes is given. <sup>(c)</sup> Integrated intensity of the line or  $3\sigma$  upper limit in  $T_{\text{mb}}$  or  $T_b$  units. <sup>(d)</sup> Brightness temperature calculated from flux within the Rayleigh-Jeans approximation.

ther improved by a self-calibration procedure performed on the cumulative continuum emission. The spectra were recorded at a resolution equivalent to about 0.43 km s<sup>-1</sup>.

ALMA observed Mira again in Band 7 on 12, 14, and 15 June 2014 in the same antenna configuration reaching an angular resolution of 0 $''$ .34 $\times$ 0 $''$ .32 in the combined data. The observations are described in Planesas et al. (2016). Four spectral ranges were observed: 330.4–330.7 and 345.6–345.9 GHz – at a velocity resolution of 0.1 km s<sup>-1</sup> – and 331.1–332.8 and 343.7–345.5 GHz, at a velocity resolution of about 13.6 km s<sup>-1</sup>. One of the latter ranges – observed with the low spectral resolution – covers the  $N=9\rightarrow 8$  line of AIO. We imaged the data combining visibilities from the three dates. The data were calibrated in flux using observations of J0334-401, J0238+166, and J2258-279, whose fluxes are known to within 15%. Further flux equalization between the three datasets was performed by setting the flux of the phase calibrator, J0217+0144, to the same average level.

Mira was observed by ALMA again in Band 7 on 21 July 2015 reaching the best resolution and sensitivity so far at these wavelengths. Because these data were originally collected for the purpose of our study here, they are described in greater detail than the earlier ALMA observations. The spectra cover four ranges, 342.1–344.0, 344.1–346.0, 354.2–356.1, and 356.1–358.0 GHz at a resolution of 0.98 km s<sup>-1</sup>. The spectrum covers the  $N=9\rightarrow 8$  line of AIO. The observations with 42 antennas of the 12-m array arranged on baselines between 15 and 1574 m resulted in an angular resolution of about 0 $''$ .158 $\times$ 0 $''$ .127 near the line of AIO. The observations were arranged into two consecutive execution blocks, each  $\sim$ 1.1-h long. The calibra-

tors were J0224+0659 for bandpass, J0217+0144 for phase, and J0238+166 for flux calibration. For the second execution, the flux-calibration scan failed and the bandpass calibrator was used for flux calibration instead. Its fluxes were assumed to be the same as in the first execution calibrated with J0238+166. We checked that the flux calibration in the two blocks was consistent and the data were combined. In order to improve the complex gain calibration of Mira images, we performed extra optimization of phase and amplitude using an iterative self-calibration procedure performed on channels dominated by continuum emission. The procedure increased the signal-to-noise of the data by a factor of a few.

All the ALMA data were imaged with Briggs weighting with the robust parameter set to 0.5. However, for reference, we also produced images with uniform and natural weighting to increase the nominal angular resolution or sensitivity, respectively.

### 3. Results of submm/FIR observations

#### 3.1. Identification of AIO

Most of the APEX spectral ranges were arranged to cover lines of AIO resulting in observations of six different transitions. Three transitions were also covered by ALMA and *Herschel*, most of them serendipitously. Two lines were observed in multiple epochs each. All the covered lines of AIO, with their spectroscopic parameters and measured intensities, are listed in Table 1. The line frequencies were taken from Yamada et al. (1990).

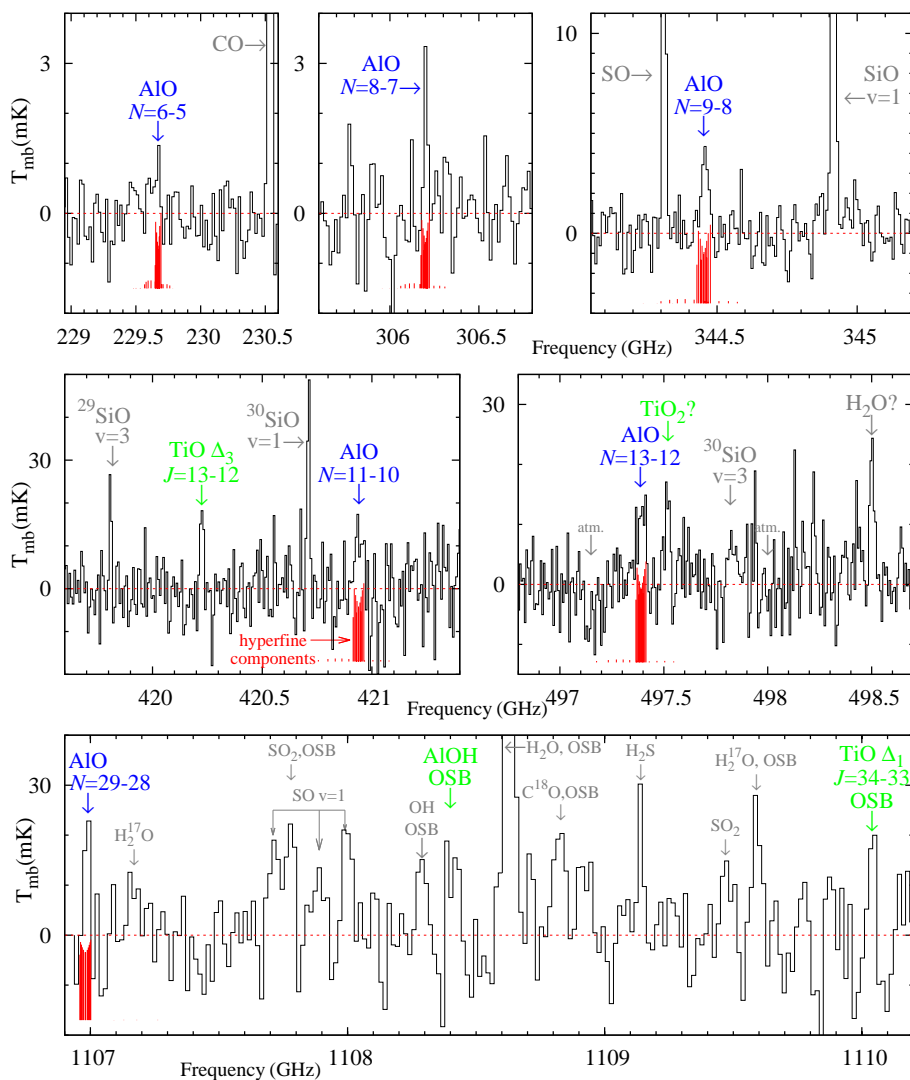


**Fig. 1. Top and middle panels:** Five lines of AIO observed in the submillimeter-wave, single sideband spectra of Mira obtained in 2013–2015 with APEX. The features of AIO are broader (FWHM) than most other lines owing to unresolved hyperfine splitting (the components are shown as red bars). **Bottom:** An archival spectrum of Mira obtained with *Herschel* in July 2010, where one other transition of AIO was observed. This double side-band spectrum contains a large number of emission lines from different species in two overlapping frequency ranges. This spectrum is smoothed to a lower resolution than in the APEX spectra shown in the upper panels.

The  $N=6\rightarrow5$  line was first covered in 2013 by APEX spectra but was not detected. When the observation was repeated with APEX in 2015, the line was detected and the emission peak was significantly above the corresponding rms noise levels of the earlier APEX attempt. As argued in Sect. 3.6, the ‘emergence’ of the line must be due to intrinsic variability of the source. The line was also observed in 2014 with ALMA within the SV observations at the high angular resolution but at the poor spectral resolution. Table 1 presents the line intensities corresponding to a region where the *absolute* intensity was above the  $3\times$  rms noise level in the profile-integrated map.

The rotational transitions from  $N_{up}=8, 9, 11, 12, 13$  were observed with APEX in several runs between 2013 and 2014. All but  $12\rightarrow11$  were firmly detected. The  $9\rightarrow8$  line was observed twice in that period, 11 months apart, and showed identical intensity in both APEX spectra (and they were combined, Sect. A.2). The same  $9\rightarrow8$  transition was observed with ALMA at four different epochs and showed clear changes in the integrated flux (Table 1). The variability is discussed in later sections.

One extra transition of AIO,  $N=29\rightarrow28$ , was covered close to the edge of a spectrum from *Herschel*/HIFI. This line was detected using the same instrumental setup as in VYCMa (Alcolea et al. 2013). The AIO emission is detected in Mira at a level of about  $3\sigma$  and is clearly apparent after smoothing the

spectrum to a resolution of a few  $\text{km s}^{-1}$ . The position of the feature agrees very well with that of the stellar radial velocity.

Most of the detected lines are shown in Figs. 1 and 2. Because the rotational lines of AIO have considerable hyperfine splitting their FWHMs are broader (typically  $\Delta\nu=60$  MHz in the submm region) than those of other thermal lines originating from the same region of the envelope. This is clearly observed in our submm spectra of Mira (Fig. 1). The  $N=29\rightarrow28$  line in the FIR *appears* narrower than those at lower frequencies owing to smaller hyperfine splitting of this high-frequency line. The positions and widths of lines leave little doubt that they belong to AIO. Our APEX observations covered a substantial range of frequencies within the available 345 and 460 GHz atmospheric windows, which combined with the *Herschel* FIR spectra allowed us to perform a comprehensive identification of spectral features. As a result we can confidently state that none of the detected transitions assigned to AIO is significantly contaminated by other species observed in Mira.

With the observations in hand, in the following sections we attempt to characterize the AIO-containing gas that gives rise to the rotational emission.



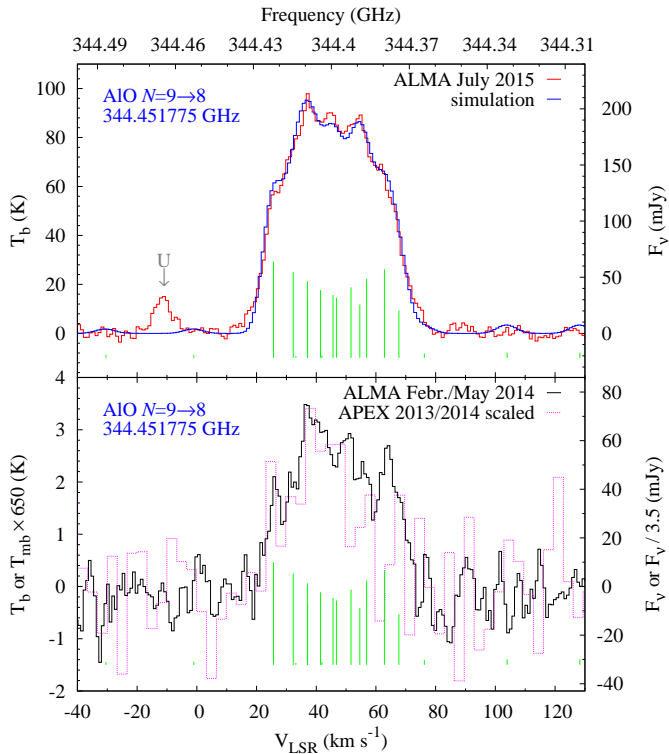


**Fig. 2.** **Top:** The AIO  $N=9\rightarrow8$  spectrum observed with ALMA on 12 July 2015 (red line). This is the best-quality (S/N and spectral resolution) spectrum of this transition to date. It was extracted from a region where profile-integrated flux is above the  $3\times$ rms noise level. Our simulation of the profile is drawn in blue (see text for details). The green vertical bars mark individual hyperfine components with the height of the bars corresponding to the relative line strength,  $S_i$ , at  $V_{\text{LSR}}$  of  $46.9\text{ km s}^{-1}$ . **Bottom:** The profiles of the same line in the APEX (magenta) and ALMA data from Feb. and May 2014 (black). Both spectra were smoothed for clarity. The APEX spectrum is scaled in intensity units.

### 3.2. Location and extent of the AIO emission

The high angular resolution of the ALMA SV observations of the  $N=6\rightarrow5$  line provide the most detailed view of the AIO spatial structure. Figure 3 presents a map of the continuum-subtracted and profile-integrated flux in the line (the appearance of the region depends on the details of data processing as explained in Appendix B). These observations resolved the stellar radio photosphere (Matthews et al. 2015; Wong et al. 2016) and we definitely observe AIO absorption toward the resolved stellar disk. It is represented by the negative signal in Fig. 3. The absorption against the stellar disk must be formed in gas with an excitation temperature lower than that of the mm-wave photosphere, i.e. below 2600 K (Wong et al. 2016).

The absorption region is surrounded by patchy emission with the strongest discrete components located approximately 63 mas east and 42 mas north from the stellar center, i.e. very near the edge of the mm-wave photosphere ( $2R_{\text{mm,ph}}=51.2\times41.0\text{ mas}$  or  $2.9\text{--}4.4R_\star$ ). Toward the southwest, we see only weak AIO emission, if at all. The S/N of the map is not good enough to state precisely how far from the stellar disk the AIO emission spreads out but all emission above three times the map rms noise level is encompassed by a circle of a  $\sim 100\text{ mas}$  radius.

In order to increase the dynamic range of the observations and infer the overall distribution of the AIO gas, we created a radial profile of the AIO region by averaging the map in the full

azimuthal angle around the position of the continuum peak. The profile, shown in Fig. 4, demonstrates that the brightness nearly follows a power-law distribution and rises just next to the edge of the radio photosphere (the effect is smeared by the restoring beam). It can be traced as far as 150 mas ( $10R_\star$ ) from the star center. Some bumps seen at larger radii are unlikely to be real.

The minimum and maximum fluxes of the AIO( $6\rightarrow5$ ) emission are  $-73.4$  and  $+153.8\text{ mJy/beam km s}^{-1}$ . The emission above the  $3\sigma$  noise level occupies a solid angle about 27 times larger than that of absorption below the  $-3\sigma$  level. This dominance of emission over absorption should produce a net pure emission feature if the source was not spatially resolved. Indeed, the  $N=9\rightarrow8$  transition of AIO when observed with ALMA at  $\sim 5$  times lower angular resolution than the SV data appears as an emission region, i.e. no negative component is apparent (Fig. 5). A Gaussian fit to the profile-integrated map of AIO( $9\rightarrow8$ ) gives a source size of  $123\times74\text{ mas}$  ( $\pm 6\text{ mas}$ ) at  $\text{PA}=95^\circ.1\pm 5^\circ.3$ . As can be seen in Fig. 5, the emission center is offset from the center of the submm-wave continuum by  $40.2\pm 2.3\text{ mas}$  ( $2.8R_\star$ ) toward the northeast ( $\text{PA}=45^\circ\pm 3^\circ$ ). What we observe in  $N=9\rightarrow8$  is likely a combination of emission and absorption similar to that seen in  $N=6\rightarrow5$ . Indeed, the SV  $N=6\rightarrow5$  data smoothed to the resolution of the  $N=9\rightarrow8$  data from 2015 show almost exactly the same morphology and relative offset of the net AIO emission with respect to continuum. The AIO peak in the smoothed data is at an offset of  $33.2\pm 0.9\text{ mas}$  ( $2.3R_\star$ ) along a PA of  $42^\circ\pm 2^\circ$ . This comparison suggests that the overall distribution of the emission clumps did not change considerably over the nine months between the observations and at the different phases (0.5 vs. 0.2). We also note that the emission area of the  $6\rightarrow5$  line is equivalent to a Gaussian source with a FWHM of 107 mas which is very close to the geometric mean of the size we determined for the  $9\rightarrow8$  line,  $\text{FWHM}=95\text{ mas}$ . The latter line is observed at a S/N of 140 so we recover essentially all of its emission. That they cover the same effective area implies that we recover most of the emission in  $N=6\rightarrow5$ , even though it is observed at a lower S/N of 20 (when smoothed to the same angular resolution). The two transitions have  $E_u$  values that differ by only about 44 K and thus should not show drastically different morphologies.

In the ALMA data for the  $N=9\rightarrow8$  line from February, May, and June 2014, the angular resolution is not good enough to fully resolve the binary and the location of AIO emission with respect to Mira A alone cannot be investigated in detail. Nevertheless, simple single-component fits to AIO emission and to the combined continuum of Mira A and B<sup>5</sup> imply that the AIO emission in June 2014 was located  $30\pm 4\text{ mas}$  northeast ( $\text{PA}=44^\circ.5\pm 7^\circ.2$ ) off the continuum peak. The size of the AIO emission in this dataset is  $149.9(\pm 9.7)\times 117.5(\pm 12.5)\text{ mas}$  and the source is elongated along a PA of  $129^\circ\pm 7^\circ$ .

In the data from May 2014, at an even poorer angular resolution, the offset is also present and is measured to be  $51\pm 28\text{ mas}$  at  $\text{PA}=14^\circ\pm 23^\circ$ . The source size is  $176(\pm 22)\times 85(\pm 29)\text{ mas}$  at  $\text{PA}=94^\circ\pm 12^\circ$ . The angular resolution and S/N of the data from February are too poor to put any reliable constraints on the size and location of AIO.

It can be concluded that the general distribution of the AIO gas around the stellar disk did not change considerably over the entire period of the ALMA observations discussed here (29 Oct. 2014–21 July 2015) with the net emission being strongest at 30–50 mas ( $2.0\text{--}3.5R_\star$ ) northeast from the star and with its longer

<sup>5</sup> The cumulative continuum flux is largely dominated by the A component as their submm flux ratio is 13.5 (Planesas et al. 2016).

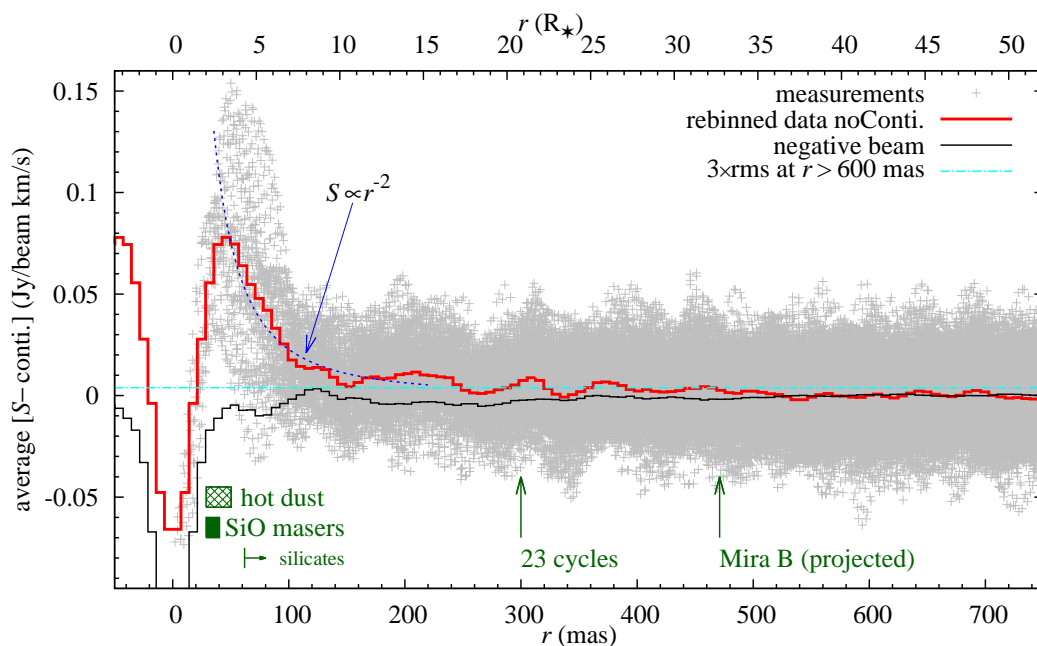


**Fig. 4.** The gray points are brightness measurements,  $S = \int S_\nu d\nu$ , of the AIO(6→5) line with ALMA plotted against the distance from the continuum peak. (They represent values of each pixel of the integrated-intensity map plotted against the radial distance of the pixel with respect to the star.) The red line is a binned average of those measurements mirrored around zero. The cyan dash-dot horizontal line marks the  $3\times\text{rms}$  level measured beyond  $0''.6$ . The AIO emission can be traced above this  $3\times\text{rms}$  level up to about 400 mas and the overall profile is well reproduced by a power law, with an example drawn with a dashed curve. Drawn with a black line is the azimuthally averaged dirty beam which was scaled and inverted in intensity to show the errorbeam structures corresponding to the strongest observed component of the profile. At the bottom of the plot, in green, are shown some characteristic locations within the envelope: the region closest to the star where hot dust has been observed in minimum (inner edge) and maximum light (outer edge) (Degiacomi et al. 1992); the range of SiO maser rings (Cotton et al. 2006); the innermost radius where silicate dust is observed in Mira stars marked as “silicates” (Karovicova et al. 2013; Wong et al. 2016); the radius at which the wind arrives after 23 cycles (or 20.8 yr) at the terminal wind speed of  $5 \text{ km s}^{-1}$ ; and the projected location of Mira B.

axis extending approximately along a PA of  $90^\circ$ – $130^\circ$ . The typical size of the emission region is  $(120\text{--}175)\times(75\text{--}120)$  mas.

Among all the species observed with ALMA longest baselines so far (Wong et al. 2016), only one weak line of SO ( $^3\Sigma^-7_8 - 7_7$  with  $E_u=81 \text{ K}$  near  $214.33 \text{ GHz}$ ) exhibits a morphology similar to that of AIO. The similarity of AIO emission to the spatial distribution of SO might suggest a similar excitation mechanism.

### 3.3. Analysis of the spectral profiles of AIO

The spectral resolution of the ALMA SV data of the  $N=6\rightarrow5$  line is rather poor and the entire line is only covered by seven resolution elements. Nonetheless, it still reveals interesting information about AIO around Mira A. We extracted spectra from the continuum-subtracted cube within three apertures with the size of the synthesized beam centered at (i) the absorption minimum, (ii) maximum emission east from the stellar disk and (iii) north from it. The absorption trough and eastern emission reach their extrema at exactly the same velocity of  $53.4\pm0.5 \text{ km s}^{-1}$ , while the northern emission peaks at  $42.4\pm0.4 \text{ km s}^{-1}$ . We next find that in a net spectrum averaged over the entire AIO(6→5) region, i.e. including emission and absorption, the profile is centered at the same velocity as the northern emission,  $42.0\pm0.5 \text{ km s}^{-1}$  (the errors given here are  $1\sigma$  uncertainties of a Gaussian fit). The shift between the bulk of emission and the northern emission with respect to absorption and eastern emission of  $11 \text{ km s}^{-1}$  is much smaller than one resolution element of  $20.4 \text{ km s}^{-1}$ . With such a coarse binning and our modest S/N, these results are tentative, but we believe that there is an actual shift.

Our highest-quality spectrum of the  $N=9\rightarrow8$  line is the one acquired with ALMA on 12 July 2015 and is shown in the top panel of Fig. 2. The spectral resolution and S/N ratio are sufficient to observe a multi-peak structure of the AIO profile imposed by the numerous overlapping hyperfine components. The hyperfine structure and intrinsic broadening form a profile with FWHM of  $45 \text{ km s}^{-1}$ . We performed a simple simulation of the profile where each hyperfine component was represented by a Gaussian of intensity proportional to the component’s strength,  $S_i$ . The central velocity was derived by cross-correlating the spectrum with the simulation in the `rv.fxor` task of IRAF and additional  $\chi^2$  model testing was performed in CASIS<sup>6</sup>. This yielded a radial velocity  $V_{\text{LSR}}=46.9\pm0.1 \text{ km s}^{-1}$  and intrinsic line width (FWHM) in the range  $8\text{--}14 \text{ km s}^{-1}$ . The simulation reproduces the observed profile satisfactorily as shown in Fig. 2. The central velocity of  $N=9\rightarrow8$  is consistent to within the uncertainties with the center-of-mass velocity of Mira of  $V_{\text{LSR,sys}}=46.8\pm0.5 \text{ km s}^{-1}$ .

All other ALMA and APEX spectra of the  $N=9\rightarrow8$  transition have too poor spectral resolution or S/N for a detailed analysis. Nevertheless, their positions and widths are generally consistent with what we have derived from the ALMA 2015 data. Two of the profiles are shown in Fig. 2. The shape of the profile from combined ALMA observations from February and May 2014 displays sub-peaks that appear sharper than in 2015. This may indicate that the intrinsic broadening was smaller in 2014.

<sup>6</sup> <http://cassis.irap.omp.eu/>



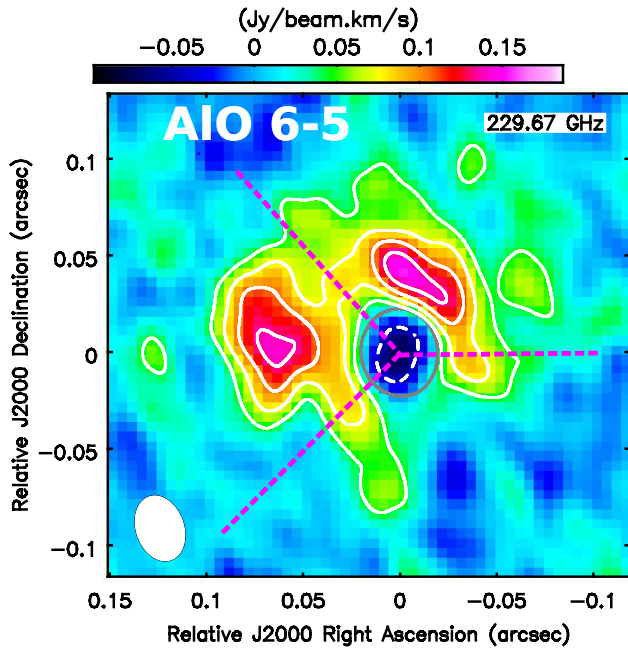


**Fig. 3.** The integrated-intensity map of AIO emission in the  $N=6\rightarrow5$  transition as observed with ALMA with a beam of  $34\times24$  mas, shown as a white ellipse. White contours are drawn at  $-3$  (dashed), 3, 4, 5, 6 times the map rms noise level of  $15\text{ mJy/beam km s}^{-1}$ . For comparison, the continuum emission is shown with a gray contour at 50% of its peak emission which represents the extend of the beam-smeared radio photosphere. The dashed lines (magenta) show the directions of spatial cuts which are presented in Fig. 9. The map was produced by using data processed in CLEAN after continuum subtraction.

### 3.4. Interpretation

The AIO observations can all be understood in a scenario in which inhomogeneously distributed AIO gas is infalling on the star: the strong northern emission component of  $N=6\rightarrow5$  has nearly the same radial velocity as the star because it is located primarily in the plane of the sky and its motions are dominated by the tangential component. The redshifted absorption must be in front of the stellar disk and provides the strongest support for the infall interpretation; the eastern emission of AIO  $6\rightarrow5$ , which also seems to be redshifted, must then be located closer to us than the star. However, we cannot entirely exclude here, that the velocity field may show an irregular pattern and that the individual clumps move randomly, with some moving out from the star while others fall on it. Then, the location of the emitting regions along the line of sight cannot be defined by the radial motions alone. (The redshifted absorption would, invariably, indicate infall motions in the part of the envelope seen against the stellar photosphere.)

The large broadening of  $8\text{--}14\text{ km s}^{-1}$  is likely related to the projected velocity dispersion within the AIO envelope. The maximum radial velocity probed by the emission in a spherically symmetric infalling (or outflowing) envelope of a radius  $r$  seen partially against a stellar disk of a radius  $R_\star$  is  $V_{r,\text{max}} = V_{\text{max}} \sqrt{1 - \sin^2(R_\star/r)}$ . The expected projected velocity dispersion is twice that figure. We observe the AIO emission at radii of  $3\text{--}5.5 R_\star$  (Sect. 3.2) for which the velocity dispersion simplifies to  $V_{r,\text{max}} \approx V_{\text{max}}$ . This means that the observed maximum radial velocity is already a good measure of the maximum deprojected velocity. From this, we imply that the AIO gas captured by the

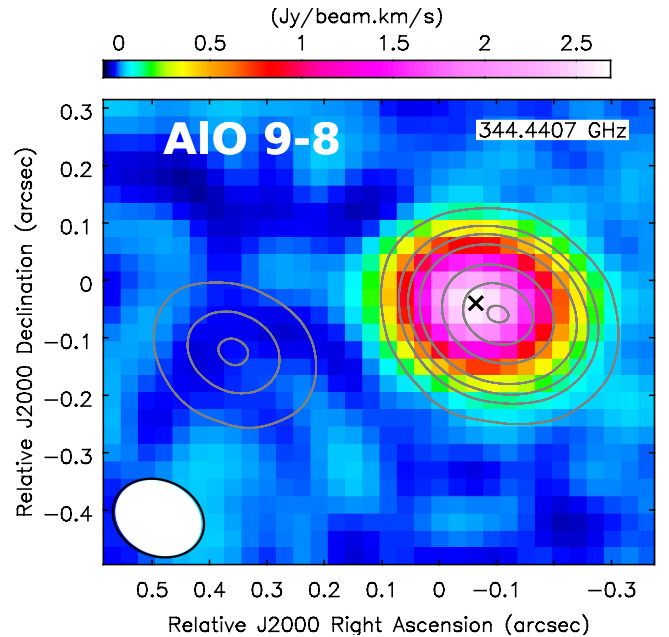


**Fig. 5.** The same as Fig. 3, but for the  $N=9\rightarrow8$  transition of AIO observed with a lower angular resolution of  $163\times132$  mas. Note that the map shows a region of the sky  $\sim 4$  times larger than in Fig. 3 and also encompasses Mira B (left continuum source). Gray contours show continuum emission of the binary at levels of 2.5, 5, 10, 30, 60, and 90% of the maximum. The center of the AIO emission, marked with a black cross, does not coincide with that of the continuum of Mira A.

observations is most likely infalling on Mira with a typical velocity of about  $4\text{--}7\text{ km s}^{-1}$ . If we are only seeing random clumps which do not reach the maximum possible velocity allowed by the dynamic process responsible for the motion, then the range of  $4\text{--}7\text{ km s}^{-1}$  is only a lower limit on the maximum velocity. We note, however, that the detailed model of Mira's envelope of Wong et al. (2016), constrained by high-quality ALMA data, also includes infall motions with an amplitude of  $7\text{ km s}^{-1}$ .

### 3.5. Excitation analysis and abundance determinations

The physical conditions of the AIO-bearing gas were constrained by using a population-diagram (Goldsmith & Langer 1999). All our measurements, corrected for the beam filling factor, are shown in Fig. 6. The scatter in point positions is large even for a single transition which was measured several times. We interpret this scatter as a consequence of true variability of the emission and discuss it in more detail in Sect. 3.6. First, we treat the upper limits and the two measurements of  $N=9\rightarrow8$  with the lowest fluxes, both from the Ramstedt et al. dataset, as outliers and will ignore them for now. We obtain a linear fit to the remaining points using a weighted least-square regression procedure. This yielded the excitation temperature of  $T_{\text{ex}} = 329 \pm 51\text{ K}$  and a column density of  $N(\text{AIO}) = (4.0 \pm 0.6) \times 10^{15}\text{ cm}^{-2}$ . The linear fit is shown in Fig. 6.

The derived  $T_{\text{ex}}$  and  $N(\text{AIO})$  are subject to many uncertainties (cf. Mangum & Shirley 2015). In our simple excitation analysis, it was assumed that the lines are optically thin and arise in isothermal gas under local thermodynamic equilibrium (LTE) conditions. To correct the measurements for beam filling factors, we assumed a source size equal to a circular Gaussian of  $0''.12$  FWHM. This is the typical size we found in Sect. 3.2.

An important difficulty in analyzing the AIO data is a possible violation of the Boltzmann distribution in level populations.

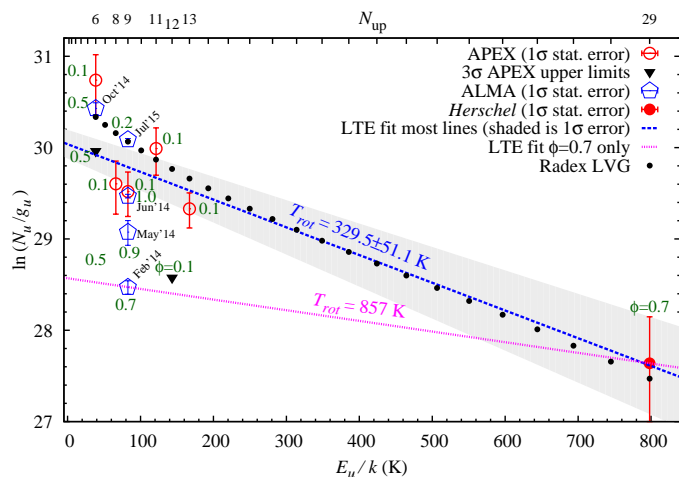


**Fig. 6.** Population diagram for AIO. Circles and pentagons represent detected lines, while triangles mark upper limits. The dashed blue line is the LTE linear fit to most of the detected lines (see text). The dotted magenta line is a fit to the two points with  $\phi=0.7$ . Black filled circles correspond to a non-LTE RADEX model with nearly the same parameters as constrained in the LTE fit and with  $H_2$  density of  $10^9 \text{ cm}^{-3}$ . Numbers in green show the visual phase corresponding to the datapoints.

Even if only the APEX data collected before 2015 are taken into account, it is clear that under thermal equilibrium the  $N=12 \rightarrow 11$  line ( $E_u=143.3 \text{ K}$ ) should have been detected significantly above the noise level. We can reject any possibility that this line was not detected owing to instrumental or data-reduction problems. Because the observation of  $N=12 \rightarrow 11$  was nearly simultaneous with the observation of the  $11 \rightarrow 10$  line, which has a similar value of  $E_u$  and which was detected with the same instrument, the only explanation of the observations is that the excitation of the AIO gas violates the assumption of LTE. The population of rotational levels may be strongly influenced by optical/IR excitation. This scenario is supported by the presence of AIO bands in optical spectra of Mira and their irregular variability (Sect. 4). In the face of these arguments, the excitation temperature we obtain is ill-defined and does not have to be equal to the local kinetic temperature. Indeed, for the bulk of AIO gas located within a radius of  $\sim 70 \text{ mas}$  (Sect. 3.2), models of Mira’s envelope predict a kinetic temperature above about  $900 \text{ K}$  (Ireland et al. 2011, o54 models) or above  $570 \text{ K}$  (Wong et al. 2016).

We tested some of the assumptions of our population-diagram analysis by performing additional calculations with the radiative-transfer code RADEX (van der Tak et al. 2007) which applies the escape-probability formulation to solve the radiative transfer problem in one dimension under non-LTE conditions (statistical equilibrium is assumed). It still assumes a homogeneous and isothermal medium, but takes into account the line opacity effects. We used it in a mode that is equivalent to the large-velocity-gradient (LVG) method for a spherical envelope. To account for collisions of AIO with molecular hydrogen, we used the scaled collision-rate coefficients derived for SiO and He (Dayou & Balança 2006) in the form in which they appear in the LAMDA database<sup>7</sup>. All the observed AIO lines become thermalized for hydrogen densities exceeding  $\log(n/\text{cm}^3)=8$ . At higher  $H_2$  densities and at the kinetic temperature and column density derived from the population-diagram analysis, we find that all the observed lines are optically thin with an optical depth of  $\tau=0.1\text{--}0.4$ . In Fig. 6, we present a RADEX model with a

slightly higher column density,  $N(\text{AIO})=6 \cdot 10^{15} \text{ cm}^{-2}$ , which fits the fluxes of our best ALMA measurements very well.

A severe shortcoming of the rotational-diagram analysis is the sparse coverage of  $E_u$ , especially for higher rotational transitions. Our temperature fit relies strongly on the *Herschel* measurement at the high-energy end. Without this single observational point, the excitation temperature would be poorly constrained ( $194 \pm 143 \text{ K}$ ) for the selected measurements. Furthermore, if we assume that the line fluxes change regularly with phase, the *Herschel* measurement at  $\phi=0.7$  does not match most of the other considered points collected mainly close to the visual maximum. There is only one other measurement of AIO emission at  $\phi=0.7$  which was obtained with ALMA in February 2014 and was discarded in our earlier analysis because its fluxes were significantly below all other measurements. Combining the two measurements yielded an excitation temperature of  $857 \text{ K}$  and a column density of  $2 \cdot 10^{15} \text{ cm}^{-2}$ . While the column density is practically the same as that obtained in our earlier approach, the excitation temperature is significantly higher and is closer to the kinetic temperature expected in a region near radii of  $3 R_\star$ . If we now naively assume this is the actual excitation temperature at phase 0.7 and the temperature does not change significantly with phase, one needs two orders of magnitude higher column density of AIO to explain most of the measurements obtained near maximum light in the mm and submm range. This interpretation of our data would indicate significant changes in the amount of AIO with phase. We, however, disfavor this scenario because the line variability is not correlated with phase (see below) and hydrodynamic models predict drastic changes in gas temperature close to the star (e.g. Ireland et al. 2011).

**Abundance** The derived AIO column density should be corrected for the effect from absorption (less than 5% of the derived  $N(\text{AIO})$ ) and increased by AIO residing behind the radio photosphere (at most 10%). These corrections are much smaller than the uncertainties in the estimated value of  $N(\text{AIO})$ . We use the value of  $N(\text{AIO})=5 \cdot 10^{15} \text{ cm}^{-2}$ , as the most representative, i.e. time- and area<sup>8</sup>-averaged column density. Its full uncertainty – including that of the source size, actual temperature, radiative transfer details, data processing – is at least an order of magnitude. A calculation of a realistic abundance of AIO from this figure requires knowing the distribution and density of hydrogen. This information is not available from observations. It is even unknown whether hydrogen is mainly in the molecular or atomic form (see discussion in Wong et al. 2016). One can attempt to calculate the abundance using the density profiles of theoretical and semi-empirical models of Mira’s environment but those usually assume spherical symmetry and differ in the absolute density scales at a given radius by orders of magnitude. For instance, for the hydrodynamic CODEX models of the o54 series<sup>9</sup> of Ireland et al. (2011), we get average  $H_2$  column densities of the order of  $10^{22}\text{--}10^{24} \text{ cm}^{-2}$  which give an AIO abundance of the order of  $10^{-7}\text{--}10^{-9}$ . Referring to the semi-empirical model of Wong et al. (2016), we obtain an AIO abundance of  $5 \cdot 10^{-10}$ . These values are significantly lower than the cosmic elemental abundance of aluminum with respect to hydrogen of  $3 \times 10^{-6}$  (or twice that value with respect to molecular hydrogen). If our cal-

<sup>8</sup> Meaning the area in which  $S_\nu$  is above the  $3\sigma$  noise level.

<sup>9</sup> This series was constructed to fit the physical parameters of o Ceti. We converted the mass densities to number densities assuming a composition of 30% He and 70% of  $H_2$ . The  $H_2$  column density was calculated for twice the distance from the radio photosphere to  $90 \text{ mas}$ .

<sup>7</sup> <http://home.strw.leidenuniv.nl/~moldata/>

culations are correct, a significant fraction of Al, at least ~90%, is locked in species other than AIO.

### 3.6. AIO variability at submm wavelengths

It should be noted that our excitation analysis has the complication that we combined data from different epochs but we have provided proof that the emission is likely variable at least in some of the lines. The current data suggest that the emission region does not change much in shape and size on a timescale of years, but the absolute flux in some lines vary considerably. This is best illustrated in the population diagram in Fig. 6. The magnitude of the variability indicated by the spread in the measurements of each of the  $N=6\rightarrow5$  and  $9\rightarrow8$  transitions is a factor a few or more, which can strongly influence the temperature determination. It is not known whether the variability is due to changes in the excitation temperature or the column density of AIO.

The variability of AIO lines may be a phenomenon related to that observed in SiO masers in Mira variables. The two lowest rotational lines of SiO  $v=1$  and  $v=2$  near 43 and 86 GHz show variability that correlates closely with phase. The maximum maser emission occurs near visual phases 0.05–0.2 (0.13 for *o* Ceti) and thus coincides with the maximum of infrared light curves (Pardo et al. 2004). This correlation is likely to be related to radiative pumping through vibrational bands of SiO in the near-infrared (Martinez et al. 1988; Cho et al. 1996; Pardo et al. 2004). The SiO amplitude changes from cycle to cycle, in particular for *o* Ceti. Higher rotational lines of SiO at mm and submm wavelengths vary strongly with phase too. In the first systematic study of this phenomenon, Gray et al. (1999) found some lines to disappear completely for phases in a range 0.4–0.7. Interestingly and contrary to SiO masers, radio maser emission of OH seems to show variability that anti-correlates with optical light variations (Gerard & Bourgois 1993) so there may be different phenomena driving variable line emission.

Our submm observations of AIO provide poor coverage of the stellar variability phase (see Table 1) because most of the observations were conducted near optical maxima, i.e. near visual phase 0.1. All but one spectrum obtained near this phase resulted in an AIO detection, but the two single-dish observations obtained at a later phase near 0.5 did not show AIO emission. At still later phases of 0.7 and 0.9, the very sensitive ALMA observations showed lower intensity than measurements at phases 0.1–0.2. One can claim that there is a general trend of AIO intensity decreasing with phase which would correspond to what is observed for the mm/submm masers of SiO. However, the pattern of AIO variability in Mira seems very erratic. There are multiple exceptions that differ from the above trend: (i) the  $N=29\rightarrow28$  line observed with *Herschel* was detected at a very late phase of 0.7 (visual light minimum); (ii) the  $N=12\rightarrow11$  line was not detected although it was observed near infrared maximum (phase 0.1) simultaneously with other AIO lines which were detected; and (iii) the  $N=6\rightarrow5$  line observed with ALMA and APEX shows very consistent intensities although probed at phases of 0.1 and 0.5. Also, the  $9\rightarrow8$  line observed in August 2014 ( $\varphi=0.1$ ), June 2014 ( $\varphi=0.0$ ), and July 2014 ( $\varphi=0.1$ ) shows excellent agreement although it was measured in different cycles. For comparison, the SiO maser lines hardly ever have the same flux in different cycles.

Although we took every precaution to use the best possible data, our picture of the variability in AIO transitions may be slightly distorted by instrumental and calibration issues. Better phase coverage and observations in multiple cycles are needed to

obtain more conclusive variability studies of submm AIO lines in Mira. However, erratic variability is also observed in the optical bands of AIO discussed in Sect. 4.1.1.

### 3.7. Identification and analysis of AIOH

Rotational lines of AIOH were measured accurately in the laboratory (Apponi et al. 1993) but it has only been identified in the circumstellar envelope of the red supergiant VY CMa (Tenenbaum & Ziurys 2010; Kamiński et al. 2013b). Our APEX observations covered three transitions of AIOH ( $J=11\rightarrow10$ ,  $13\rightarrow12$ ,  $15\rightarrow14$ ) and the collected *Herschel*/HIFI spectra covered five more transitions ( $18\rightarrow17$ ,  $21\rightarrow20$ ,  $22\rightarrow21$ ,  $33\rightarrow32$ , and  $35\rightarrow34$ ). Only three were found,  $J=13\rightarrow12$ ,  $15\rightarrow14$ , and  $35\rightarrow34$ , at an integrated intensity  $3\sigma$ – $5\sigma$  above the corresponding noise levels. The hyperfine splitting in the rotational lines of AIOH is smaller than that of AIO, and the width of the lines does not provide additional support for the identification as it was the case for AIO. Nevertheless, the identification is likely correct as there are no other good candidate carriers that would explain these features in a consistent manner. All AIOH observations are summarized in Table 1. Unfortunately, none of the sensitive ALMA observations covered AIOH.

Combined into a rotational diagram, the emission features imply a temperature of  $1960\pm170$  K (assuming a source size of  $0''.2$ ). Upper limits on the non-detected lines are consistent with this fit. The derived excitation temperature is high but is plausible in this source if the gas is located close to the pulsating photosphere of Mira. The drastically different temperatures for AIO and AIOH gas (330 K vs. 1960 K) are rather surprising. In the models of IK Tau of Gobrecht et al. (2016), AIO is converted in AIOH at late pulsation phases close to the star, making then AIOH the prevalent Al-bearing species at large radii. The bulk of gas containing AIOH should therefore appear cooler than the gas abundant in AIO. Our results suggest this is not the case in *o* Ceti but non-thermal level population and line variability may influence our analysis of AIOH, just as discussed for AIO in Sect. 3.5.

Because of the many uncertainties in the AIOH excitation and the unknown spatial origin of its emission, we did not derive the molecular abundances. It is important for Al chemistry in Mira, but a quantitative analysis will require more observations.

### 3.8. Other Al-bearing species in submm spectra

We searched for other Al-bearing species in the submm spectra of Mira using the standard spectral line catalogs (Pickett et al. 1998; Müller et al. 2005). The only other Al-bearing molecules observed so far in circumstellar environments are AlCl and AlF. Multiple transitions with  $E_u > 162$  K of AlCl and  $E_u > 44$  K of AlF were covered by the most sensitive APEX, ALMA, and *Herschel* observations, but none was firmly detected. We also covered but did not detect lines of AlCN, AlNC, and AlS. In Sect. 4.2, we report that AlH was observed in Mira at optical wavelengths, but no pure rotational transitions were covered (Goto & Saito 1995). An observation of this molecule at submillimeter wavelengths is challenging, because the lowest transition near 387 GHz is within a deep telluric water band. In the current data, AIO and AIOH are the most prominent mm/submm tracers of Al in *o* Ceti.

## 4. Optical spectroscopy of Al-bearing species

The optical spectra of material surrounding cool evolved stars contain useful information about gas-phase species thought to



be important for dust condensation, as has been shown in Kamiński et al. (2013) and Kamiński et al. (2013a) for VY CMa. In the following, we present results of our search of those species in multi-epoch spectra of Mira.

Of primary interest is AIO because it is the direct gas-phase precursor of alumina dust,  $\text{Al}_2\text{O}_3$  (Sarangi & Cherchneff 2015; Gobrecht et al. 2016). The electronic  $^2\Sigma^+B-^2\Sigma^+X$  system of AIO has been reported to show anomalous behavior in optical spectra of Mira variables. Not only do the strengths of the absorption bands change with phase and from cycle to cycle, but the absorption bands were observed to turn into emission features in several sources, including Mira (Keenan et al. 1969; Garrison 1997, and references therein). Here, we investigate the behavior of the optical bands of AIO in Mira using long-term spectroscopic data with the aim of identifying patterns which would allow us to establish the origin of AIO. We then used the same observational material to investigate the presence of spectral signatures of other interesting species, including AIOH, AlH, and AlI-III.

#### 4.1. Optical observations

In order to investigate the time variation of the optical bands of AIO in the spectrum of Mira, we performed an extensive search for archival spectra and literature data. We searched through all major public archives for optical spectra covering any sequence of the  $B-X$  system. Only spectra at high and intermediate resolutions turned out to be useful in our analysis. A resolution better than  $R \approx 5000$  was needed to disentangle the bandheads from nearby spectral features of other species and to investigate the shape of the rotational profile of the bands. Consequently, most of the collected data are from echelle spectrographs. The high-resolution spectra we have collected are listed in Table 2. A major portion was acquired in spectropolarimetric mode and in these cases the total-power (Stokes  $I$ ) data were analyzed. Whenever possible, we used reduced (“pipelined”) data products offered by some of the archives, while in the remaining cases the data reduction was performed manually with IRAF using standard reduction techniques (e.g. Willmarth & Barnes 1994). Particular care was taken to obtain good wavelength calibration. Exposures from the same night were averaged. Most of the spectra in our sample are not calibrated in flux. Although most of the echelle spectra were corrected for a blaze response function, the slope of the pseudo-continuum in most of the spectra is unknown at wavelength ranges covering multiple orders. Visual magnitudes for each observed spectrum are available from the densely-spaced observations of the American Association of Variable Star Observers (AAVSO). The nearest measurement for the given date is included in Table 2, as well as information on the spectral coverage (ignoring gaps in some of the echelle spectra) and resolution, references to papers describing the observing run or the name of the principal investigator of the observing project if no literature reference could be identified.

The oldest spectra we were able to access in digitized form are scanned spectral plates from the Dominion Astronomical Observatory. In addition to these, we found reproductions (scanned GIF files of paper copies) of Mira spectra covering the AIO band in Joy (1926) (later reproduced in Baxandall (1928) and Merrill et al. (1962)) and Keenan et al. (1969), which show two-dimensional plates. Additionally, Garrison (1997) showed an extracted one-dimensional spectrum. Further useful information on the appearance of AIO bands in Mira is found in Keenan et al. (1969), Kipper & Kipper (1979), and Garrison et al. (1999).

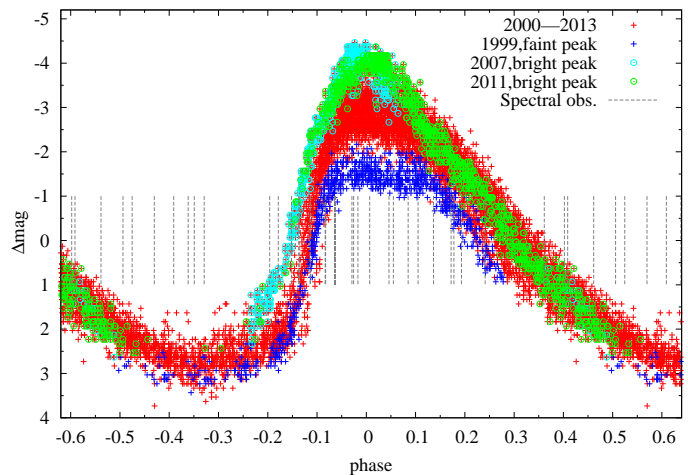


**Fig. 7.** Phased AAVSO light curve of Mira in 1999–2013. The faint-maximum cycle of 1999 and the two recent cycles with bright maxima (2007 and 2011) are shown with blue, green, and cyan symbols, respectively. The dates of spectroscopic observations (Table 2) are marked with vertical bars. For some dates, the corresponding bars appear twice in the graph, i.e. at  $\varphi$  and  $\varphi \pm 1$ .

Table 2 also lists the phase corresponding to the given observing date. Although the shape of the Mira’s visual light curve deviates strongly from a sinusoidal pattern and its period is known to change by a few days on time scales of years (Templeton & Karovska 2009), we use a simple sine function to define the phase for data since 1999, with a period of 333 days (cf. Templeton & Karovska 2009) and date of maximum on JD=2452161.0. The date of maximum was measured for the 2001 cycle which showed a very well defined maximum. Such a parametrization of the stellar periodicity is also consistent with our sinusoidal fit to the AAVSO visual data for 1999–2013. The shape of the phased light curve within that time span together with the markings representing the coverage of the collected visual spectroscopy (Table 2), are shown in Fig. 7. The maxima occur close to phase  $\varphi=0$ , while – due to an asymmetry of the actual light curve – the minima occur at  $\varphi \approx -0.33=0.67$ . Using *JHKL* photometry from Shenavrin et al. (2011) and Whitelock et al. (2000), we found that the near-infrared fluxes (*JHKL*) peak at  $\varphi = 0.17 \pm 0.05$  on our periodicity scale.

We also searched through the archives for near-infrared spectra of Mira that covered the  $A-X$  band of AIO (cf. Kamiński et al. 2015; Banerjee et al. 2012). We found only one spectrum with a sufficient spectral resolution,  $R=37\,600$ , that was obtained on 26 August 2001 ( $\varphi=0.96$ ) with the NIRSPEC instrument on Keck by A. Nelson. A simulation of the  $A-X$  system by a similar method as in Kamiński et al. (2015) revealed that the (4,0) band with heads at 1225 and 1243 nm is the strongest near-infrared band for a broad range of excitation temperatures. We reduced and inspected only the part of the Keck spectrum that covers the (4,0) band. We found no signatures of the electronic system of AIO. However, it should be noted that the spectrum was acquired only three days before optical observations with HIDES in which the AIO bands of the  $B-X$  system were very strong. This leads us to a conclusion that the NIR system is not particularly useful for studies of AIO in *o* Ceti. Indeed, the NIR band is expected to be much weaker than the optical bands (Patrascu et al. 2015).

**Table 2.** High-resolution optical spectra of Mira collected from archives.

Instrument	Telescope/observatory	Date	JD	Nominal <i>R</i>	Spectral coverage start (Å)    end (Å)		Vis. phase	Vis. mag	Reference or project PI	Notes
McKellar Spectrograph	Dominion Obs. 1.2m	1965-12-14	2439108.7	21000	3900	5100	0.94	3.5	PI: E. Griffin	<sup>a</sup>
ELODIE	OHP	1998-11-07	2451124.0	42000	4000	6800	0.89	7.0	1	<sup>b</sup>
Echelle Hi-Res Spectrogr.	Mt. Ekar 182 cm, Asiago	1999-02-11	2451221.2	20000	4600	9470	0.18	6.0	2	<sup>c</sup>
ELODIE	OHP	1999-09-29	2451450.0	42000	4000	6800	0.86	7.0	1	<sup>b</sup>
ELODIE	OHP	1999-12-16	2451528.9	42000	4000	6800	0.10	3.4	1	<sup>b</sup>
HIDES	Okayama-NAOJ 188cm	2001-08-29	2452151.3	95000	4620	5820	0.97	3.2	3	
FEROS	ESO MPI 2.2 m	2004-10-02	2453280.3	48000	3600	9200	0.36	7.2	4	<sup>d</sup>
SARG	TNG	2005-12-11	2453716.4	11800	5000	8000	0.67	9.0	PI: E. Verdugo	<sup>e</sup>
ESPaDOnS	CFHT 3.6m	2006-08-14	2453962.1	68000	3690	10480	0.41	7.2	PI: Dinh-V.-Trung	<sup>f</sup>
SOPHIE	OHP 1.93m	2007-01-12	2454113.3	75000	3870	6940	0.86	5.6	PI: D. Gillet	<sup>b</sup>
SOPHIE	OHP 1.93m	2007-01-20	2454121.2	75000	3870	6940	0.89	4.3	PI: D. Gillet	<sup>b</sup>
SOPHIE	OHP 1.93m	2007-01-30	2454131.2	75000	3870	6940	0.92	3.3	PI: D. Gillet	<sup>b</sup>
ISIS	WHT, INT la Palma	2007-07-31	2454312.7	4500	3650-4560	6630-7300	0.46	8.5	PI: F. Leone	<sup>f</sup>
MMCS	ZEISS-2000, Terskol Astr. Obs.	2007-08-15	2454327.5	13000	3970	7485	0.51	8.3	PI: O. Andriyenko	
NARVAL	2m TBL, Pic du Midi	2007-09-04	2454348.7	65000	3700	10480	0.57	8.8	5	<sup>f</sup>
		2008-01-20	2454486.3				0.98	3.6		
		2008-02-10	2454507.3				0.05	4.2		
		2008-08-29	2454708.7				0.65	9.2		
		2009-02-26	2454889.3				0.19	5.1		
		2009-07-24	2455037.6				0.64	9.2		
		2009-09-23	2455098.5				0.82	8.8		
		2009-10-03	2455107.4				0.85	8.0		
		2009-10-25	2455130.5				0.92	4.7		
		2009-11-24	2455160.3				0.01	3.5		
		2009-12-10	2455176.3				0.05	4.0		
		2009-12-20	2455186.3				0.08	4.2		
		2010-01-06	2455203.4				0.14	4.6		
		2010-01-18	2455215.3				0.17	4.7		
		2010-02-10	2455238.3				0.24	5.4		
HARPS	ESO 3.6m	2012-08-09	2456148.4	115000	3780-5300	5340-6910	0.97	3.7	PI: F. Leone	<sup>f</sup>

**References.** (1) Alvarez et al. (2001); (2) Tomasella et al. (2010); (3) Kimata & Izumiura (2003); (4) Zamanov et al. (2006); (5) Fabas et al. (2011).

**Notes.** <sup>(a)</sup> Scanned plate. <sup>(b)</sup> Archive product. <sup>(c)</sup> Interorder gaps above 6880Å. <sup>(d)</sup> Interorder gaps above 8530Å. <sup>(e)</sup> Underexposed in blue part. <sup>(f)</sup> Spectropolarimetric observation.

#### 4.1.1. Observed variations in the B-X band of AIO

We were able to identify features in the AIO  $B-X$  system involving the vibrational levels up to at least  $v_{\text{up}}=3$  in the upper electronic state in all the collected high- and mid-resolution spectra of Mira. The main bandheads appear in absorption, occasionally in emission, and as a combination of absorption and emission features. Examples of emission- and absorption-dominated spectra are shown in Fig. 8. Independent of whether they appear in emission or in absorption, the bandheads are rather weak, but the characteristic shape of the band is readily recognizable in the spectra.

The collected spectra are sufficient to study the long-term variability within the bands which is not feasible with the current mm and submm data. Results of this analysis are presented separately for spectra dominated by absorption and emission in Sects. 4.1.2 and 4.1.2. All spectra covering the AIO sequences  $\Delta v=2, 1, 0, -1$  are shown in the spectral atlas in Figs. C.2–C.5.

#### 4.1.2. Absorption in AIO

The  $\Delta v=-2$  sequence, located near 5340 Å, and all negative sequences at longer wavelengths – although covered by many of our spectra – are too weak for variability studies. The  $\Delta v=-1$  sequence near 5080 Å is dominated by absorption features which show definite variability. Episodes when AIO absorption becomes weaker than normal were identified. The weakest absorption band was observed on 2012-08-09. The weakening of those bands is not correlated with phase or time. The apparent weakening of those absorption features may be due to an overlying AIO emission component of variable intensity. A presence of such a component is evident in the higher progressions,  $\Delta v=0$  and 1. Bands within the  $\Delta v=0$  sequence are weak but still definitely present.

We used the spectra of the  $\Delta v=-1$  sequence, which is longward of 5080 Å and is not contaminated or just weakly so by emission, to measure the representative velocities of the absorbing AIO gas. First, we measured the velocity of the spectrum from 2010-02-10 by cross-correlating it with a simulated spectrum of the absorption. The cross-correlation algorithm `rv.fxcor` implemented in IRAF was used (e.g. Alpaslan 2009) and the simulated spectrum was calculated in an analogous way as in Kamiński et al. (2013). The typical velocity for our sample of spectra is  $57.5 \text{ km s}^{-1}$  with the highest measured deviations from this value of  $+2.0$  and  $-1.4 \text{ km s}^{-1}$ , and a standard deviation of  $1.0 \text{ km s}^{-1}$ . The phases corresponding to the spectra densely cover the full pulsation cycle and hence  $V_h=57.5 \pm 2.0 \text{ km s}^{-1}$  characterizes the full dispersion well. The central velocity is consistent with the center-of-mass velocity of Mira ( $V_{h,\text{sys}}=57.0 \pm 0.5 \text{ km s}^{-1}$ ) and the central velocity of the submm emission of AIO in pure rotational lines ( $V_{h,\text{sys}}=57.1 \text{ km s}^{-1}$ , Sect. 3.3). The variations in velocity that we measured are small but greater than our uncertainties.

A rare event recorded in the AIO spectra is the appearance of extra absorption components that are strongly redshifted. This is observed in the (1,0) and (2,1) heads of  $\Delta v=+1$  in 24 July, 23 September, and 3 October 2009 (but not 23 days later) – see Fig. C.3. In the same spectra, the (0,0) band is unusually broad, the (0,1) bands are slightly broader than usual, and there are no unusual changes in the other sequences. The extra absorption components therefore involve only  $v_{\text{low}}=0$  and 1 levels, suggesting that they arise in material cooler than that producing usual absorption bands of AIO and observed in progressions involving higher- $v_{\text{low}}$ . Similar apparent broadening or splitting of spectral

features is simultaneously observed for other species, including Al I (Sect. 4.3). In the profile of the AIO (2,1) band, we measured that, in addition to the usual component very close to stellar center-of-mass velocity, there are extra components at heliocentric velocities of about  $+95 \text{ km s}^{-1}$  and possibly at  $+140 \text{ km s}^{-1}$ . Such high velocities reaching  $80 \text{ km s}^{-1}$  with respect to the star are surprising, but not impossible in this source. The motions are likely not associated directly with the usual pulsation-driven shock wave, because they are absent in most of the cycles covered by our spectra.

The usual absorption profiles of AIO also show considerable variability in their widths. We infer the intrinsic Doppler broadening as the kernel width that we used to convolve our simulated spectrum to fit the observed features. When the bands are strong, their half-width is nearly  $30 \text{ km s}^{-1}$ , as in 2001-08-29 ( $\varphi=0.97$ ). Such a high velocity dispersion in Mira can only be explained as arising in the shock wake. Macroturbulence is expected to be greatly enhanced behind a shock (cf. Gillet et al. 1998), however, the broad profile may also be an opacity effect which we were not able to simulate with our simple tools. In a great majority of our spectra the absorption is narrower, often comparable to the instrumental profile of a few  $\text{km s}^{-1}$ . (It cannot be measured accurately owing to a much lower S/N of these narrow and weak features.) This may indicate that the AIO absorbing gas is present both in the shocked gas and in material that had time to dissipate the shock energy.

We could not constrain precisely the rotational temperature of the gas from the shapes of the bands. The major difficulty is how to define the level of the local pseudocontinuum underlying the bands. Another obstacle is the presence of numerous atomic absorption features that distort the band shape. Our simulation of the bandheads are nevertheless consistent with the observations within a broad range of rotational temperatures from a few hundred to  $\sim 1500 \text{ K}$ . The vibrational temperature, although variable, is likely equal to a few hundred K.

**Spatial origin of AIO absorption** Because of the complex behavior of the AIO features, we shall consider several locations of the absorbing AIO gas. If the absorption was produced in the accelerated wind seen in front of the stellar disk, the features would be blueshifted by the magnitude of the wind terminal velocity, i.e. by  $-5 \text{ km s}^{-1}$  from the stellar velocity (Sect. 1.2). Such a large offset is not observed. In addition, features arising in a homogeneous, stationary wind would not show temporal velocity variations contrary to what we have measured. Therefore, the AIO absorption features do not come from the fully-accelerated wind, and must arise closer to the star at radii  $\lesssim 5 R_\star$  (cf. Nowotny et al. 2010).

We also exclude the possibility that the AIO absorption is formed in the photosphere on the basis of the low amplitude of the velocity variations in the AIO features. Rovibrational lines  $\Delta v=3$  of CO which are observed in absorption in Mira are believed to be formed in the stellar photosphere. They show velocity variations with an amplitude of  $24 \text{ km s}^{-1}$  (Hinkle et al. 1984) which are much higher than what we have measured for the AIO absorption bands. Similarly, high-excitation atomic lines show considerable shifts with phase. By cross-correlating the spectra in the region between 4035 and 4095 Å, that is dominated by numerous sharp absorption lines, we determined that the relative displacements between different dates reach  $9.4 \text{ km s}^{-1}$ . (This value is higher than the maximal displacements found by Joy (1954), but is smaller than those in Joy (1926)). The amplitude of velocity changes for atomic lines is known to be correlated



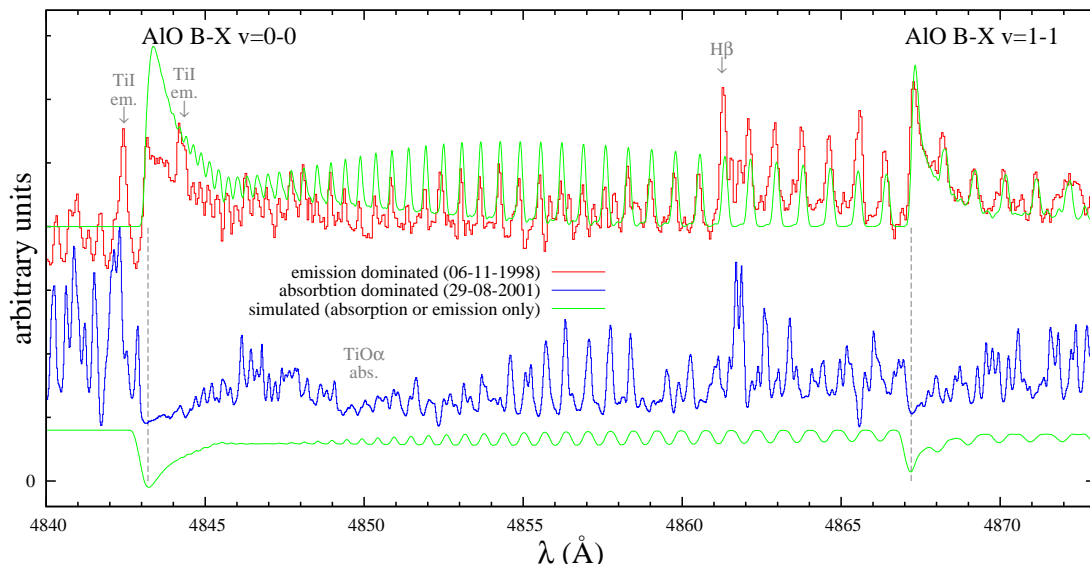


**Fig. 8.** Sample optical spectra of AIO in two epochs (red and blue), covering the heads of the (0,0) and (1,1) bands and their rotational combs. Simple simulations (green) illustrate the location of the emission and absorption components. Many spectral features are of atomic origin. The reason for the poor correspondence of the observation and simulation at the (0,0) bandhead of AIO is the lack of an underlying absorption feature in the simulation and a limited correction for optical thickness, which is highest near the head. All spectra covering these and other bands of AIO at different dates are shown in Figs. C.2–C.5.

with the brightness of the cycle’s maximum (Joy 1954) and since we covered cycles with very bright maxima (e.g. 2007) as well as faint minima (1998/99), the low amplitude of AIO displacements indicates that the AIO gas is nearly stationary, independent of this inter-cycle effect. The AIO-bearing gas therefore must be located high enough above the pulsating atmosphere to not be influenced by the regular high-amplitude motions, say at  $>2.5 R_{\star}$ .

We conclude that the visual absorption features must arise between the photosphere and the fully accelerated wind, or roughly between  $2.5$  and  $5 R_{\star}$ . The kinetic temperature in this region is  $\sim 1000$  K (as in the CODEX models of Ireland et al. 2011) which is consistent with our rough constraints on the rotational temperature of AIO as traced by the  $B$ – $X$  band. It is very likely that the electronic bands are formed in the same AIO gas as that observed in pure rotational transitions at mm and submm wavelengths. The variable nature of the electronic absorption is consistent with the observation that the AIO gas is clumpy, as seen in the  $N=6 \rightarrow 5$  line with ALMA. The observed variability can arise as clumps of different opacity pass in front of the stellar disk.

#### 4.1.3. Emission in AIO

Our spectroscopic records contain two episodes of emission-dominated profiles of AIO on: (i) 1998-11-06 with strong emission in the  $\Delta v=0$  and  $+1$  sequences, and (ii) 2007-09-04 with the strongest emission signatures in the  $\Delta v=1$  band. Much weaker, but still easily recognizable emission was seen in a sequence of spectra registered immediately after the 1998-11-06 ( $\varphi=0.9$ ) flare, i.e. on 1999-02-11 ( $\varphi=0.2$ ) and 1999-09-28 ( $\varphi=0.9$ ). Chronologically the next spectrum, from 1999-12-16, shows very weak absorption bands, but the absorption profile is definitive only in the spectrum from 2001-08-29 ( $\varphi=1.0$ ). For the AIO flaring event which was most evident on 2007-09-04 ( $\varphi=0.6$ ), the emission was observed mainly in the  $\Delta v=+1$  sequence, and was preceded and followed by spectra with emission nearly filling the absorption bands. From these two events, we

conclude that bright, easily observable emission in AIO bands may appear at any phase, may last for at least one year, and is not necessarily limited to a single cycle. This behavior is different than that observed in most atomic/ionic lines which show regular changes in intensity with peaks near  $\varphi=0.9$ – $0.1$  and minima near  $\varphi=0.6$  (Richter & Wood 2001). The two strong emission episodes took place at phases 0.9 and 0.6, i.e. near maximum and minimum visual light. This erratic variability resembles that of pure rotational lines of AIO observed at mm and submm wavelengths (Sect. 3.6).

The central velocities of the AIO emission component could only be measured for the 1998-11-06 and 2007-09-04 spectra. On the earlier date, not only the bandheads are useful for velocity measurements but also the individual features of the rotational comb far from the head are very well reproduced by our simulation and constrain the radial velocity (Fig. 8). The velocity of the band is  $V_b = 53.8 \pm 0.5 \text{ km s}^{-1}$ . The central velocity of the emission seen on 2007-09-04 is less certain but our best estimate is  $56 \pm 2 \text{ km s}^{-1}$ . The AIO emission therefore appears stationary or blueshifted by at least  $3 \text{ km s}^{-1}$  with respect to the stellar velocity ( $57.0 \pm 0.5 \text{ km s}^{-1}$ ). We believe that the underlying absorption is too weak to influence the position measurements we have performed. Although the AIO-emission episodes are too rare to form definitive statements, the kinematical characteristics resemble that observed in most atomic/ionic optical emission lines which also always appear blueshifted (Richter & Wood 2001). The atomic features are thought to be associated with a shock propagating outward in the stellar atmosphere. Low-excitation atomic lines show low velocity displacements of a few  $\text{km s}^{-1}$ , while emission features requiring high excitation can be shifted by as much as  $20 \text{ km s}^{-1}$ . We conclude that the visual emission of AIO arises when the shock front reaches the higher parts of the stellar atmosphere where the shock-imposed gas motions are small, thereby explaining the small shift of only  $3 \text{ km s}^{-1}$ .

The intrinsic broadening of the emission features is small. To reproduce the rotational comb of the AIO emission observed on 06-11-1998, we convolved the simulated spectrum with a Gaus-

sian of FWHM of  $8 \text{ km s}^{-1}$ , a value that is comparable to the resolution of the spectrum. The measured width is also consistent with that derived for the submm lines of AIO (Sect. 3.3).

#### 4.1.4. Excitation mechanism of electronic AIO bands in Mira

The upper electronic state of the  ${}^2\Sigma^+B - {}^2\Sigma^+X$  system of AIO is 28 800 K above the ground and therefore is most likely excited by shocks. Excitation temperatures of the order of  $10^4$  K are definitely possible in Miras since strong emission in recombination lines of hydrogen are observed on every cycle. Richter et al. (2003) were able to model weak and episodic emission of Fe II ( $E_u=32\,570$  K) and [Fe II] (63 950 K) on the assumption that the upper levels are excited in the shock at a radius  $\sim 1.5 R_*$ . The gas giving rise to the AIO emission might be excited in a similar way, but probably at slightly higher distances from the star. Also, if AIO emission is associated with the shock, then its presence for more than one cycle, as in 1998/1999, may indicate that the emission arises in gas of very low density that is not able to efficiently cool down only through radiation in a single period (cf. Richter et al. 2003).

Analogous to the shock-excited lines of Fe II, AIO emission is sporadic. One may speculate that the AIO bands show an emission component only when the shock reaches the AIO material that is usually seen in Mira only in the absorption bands. It is unclear why this occurs only occasionally. The episodic emission in Fe II and [Fe II] lines was linked to a shock wave that is stronger than typical and is associated with cycles that show bright maxima (Richter et al. 2003). However, as we discuss in Sect. 5.3, it is doubtful whether there is a link between the occurrence of AIO emission and bright-maxima cycles. Hydrodynamic pulsation models calculated for long time series show, however, that the positions of shock fronts and the extend of shocked gas change chaotically in Mira stars (Ireland 2011).

The absorption by AIO is most likely a result of resonant scattering of stellar light off the circumstellar gas. The gas is clumpy (Sect. 3.2) and the observed variability may be explained by different clumps passing in front of the stellar disk. Most of the time, however, the gas is stationary with respect to the center-of-mass velocity what suggests it may be located in a region sometimes referred to as a MOLsphere (Tsuji 2000) or may correspond to the "warm molecular layer" the existence of which was proposed before e.g. by Willacy & Cherchneff (1998) and Woitke et al. (1999). Interferometric observations in the infrared support the existence of such a molecular layer (Wittkowski et al. 2016, and references therein). The vibrational temperature derived from the AIO bands in *absorption* of a few hundred K is in agreement with such a location. The *emission* episodes would then be associated with events when, for some reason, the volume of AIO gas gets larger than usual so its apparent size is bigger than the stellar disk and scattered emission dominates the band appearance. This scenario is more speculative than direct shock excitation, but if it is correct it would still indicate that AIO is located in the upper atmosphere of Mira.

There must be a difference in the vibrational temperature that characterizes the absorbing and emitting gas because we observe discrepancies in the relative strengths of emission and absorption in different sequences and bands. It is also evident that the excitation conditions of the emitting gas change with time. For instance, on 2007-09-04 when the  $\Delta v=+1$  bandheads appeared as strong emission features, the corresponding  $\Delta v=0, +2$  bands showed cancel-out bands. On 1998-11-06, in turn, AIO flared in the  $\Delta v=0$  and  $+1$  sequences but this time the  $\Delta v=0$  sequence was by far the stronger one. In other words, the  $v_{\text{up}}=0-v_{\text{low}}$  progres-

sion of the emission system peaked for  $v_{\text{low}}=0$  on 1998-11-06, and for  $v_{\text{low}}=1$  on 2007-09-04, suggesting a higher vibrational temperature of the emitting gas in 2007.

We conclude that the most likely excitation mechanism of the gas that leads to the emission episodes is shocks which occasionally reach the AIO gas which we usually see only in absorption and in the mm/submm rotational lines, and which resides at a few stellar radii from the star. We interpret the appearance of AIO emission as a result of changes in excitation, but changes in abundance (either due to formation or destruction of AIO) and relocation of gas within the envelope cannot be excluded.

#### 4.2. Electronic systems of other Al-bearing molecules

**AIOH** The submm detection of AIOH in Mira (Sect. 3.7) encouraged us to look for electronic transitions of this molecule. We could not find in the literature the spectroscopic constants nor even approximate positions of electronic bands of AIOH in the optical. However, a few electronic systems of AIOH are known in the ultraviolet, i.e. close to 2395 Å and 2495 Å (Pilgrim et al. 1993; Li et al. 2003). Spectra of Mira B acquired by the International Ultraviolet Explorer (IUE) between 1979 and 1983 and by the Hubble Space Telescope (HST) in 1995 (Reimers & Cassatella 1985; Karovska et al. 1997) covered this wavelength range and show broad absorption features at the expected location of the AIOH bands. The absorption structures are not identified in the original studies and are too broad to belong to atomic transitions. Moreover, they are unlikely to be blends of known atomic lines as most strong multiplets were identified in the spectra. Furthermore, we find the same wide features in some of the archival UV spectra obtained by HST/STIS (1999 and 2004) and Galaxy Evolution Explorer (GALEX; 2006), available through the MAST archive<sup>10</sup>. Although both Mira A and B were located in the instruments apertures, it is the B component that was thought to be the major source of the continuum at these wavelengths. If AIOH is the carrier of the broad features, the gas would have to be located between us and Mira B so at least  $0''.48$  or  $8 \times 10^{14}$  cm away from Mira A. This would indicate that some aluminum is locked into AIOH at quite large distances from the pulsating atmosphere. To verify this finding will require a dedicated study of the electronic bands of AIOH in Mira.

**AlH** We were surprised to see an identification of an AlH band near 4242 Å in the historical spectral plates of Mira presented in Merrill et al. (1962, their Figs. 9 and 10), because hydrides are generally thought to be rare in spectra of giants. However, AlH has been reported in emission in another Mira variable,  $\chi$  Cyg, near minimum light (Herbig 1956; Herbig & Zappala 1968). The emission in the spectral region between 3066 Å and 4412 Å in  $\chi$  Cyg was limited to a specific range of rotational lines belonging to the (0,0), (1,0) and (1,1) bands of the  $A^1\Pi - X^1\Sigma$  system. Many of our spectra of  $\alpha$  Ceti cover these three bands and there is a great number of absorption lines in this spectral region which coincide with the positions of AlH lines in Szajna & Zachwieja (2009). A detailed simulation of the A–X band was obtained in *pgopher* (Western 2014) using the spectroscopic constants from Szajna & Zachwieja (2009). Each band consists of well separated rotational lines and the shapes of individual lines are nearly indistinguishable from atomic features in the observed spectra. The density of lines in this spectral region is very high and, in principle, chance coincidences may occur for many of the lines.

<sup>10</sup> <http://archive.stsci.edu>

We found, however, that for each strong transition of AlH there is a corresponding absorption feature in the spectra of Mira with a perfectly matching radial velocity, leaving little doubt that AlH is present in *o* Ceti. The AlH bands appear in absorption in all our spectra and the features seem to be slightly stronger with respect to the local continua near minimum visual light. The AlH bands were not found to turn into emission features in the 19 spectra we examined, indicating that Mira is unlikely to undergo AlH-flaring episodes such as those reported for  $\chi$  Cyg.

The line positions of AlH vary slightly with time. We investigated the temporal variations quantitatively using cross-correlation techniques and band simulations at different excitation temperatures. The most blueshifted spectrum of the (1,0) band was observed on 2009-07-24 ( $\varphi=0.6$ ) with  $V_h=55.2\pm0.7$  km s<sup>-1</sup> and the highest velocity of 59.2 km s<sup>-1</sup> was measured in the spectrum from 2009-10-03 ( $\varphi=0.9$ ). Such low variations of the radial motions of  $\pm 2$  km s<sup>-1</sup> with respect to the center-of-mass velocity, signify that the absorbing gas must be located in the parts of Mira's atmosphere that do not participate in the high-amplitude pulsation motions such as those observed in CO  $\Delta v=3$  lines (Hinkle et al. 1984). The AlH gas may be partially placed in the same layer where we observe AlO in absorption.

We were not able to constrain precisely the rotational temperature of AlH, because (i) the line ratios are greatly affected by the shape of the local pseudo-continua and (ii) of the presence of other unidentified lines in these spectral regions. However, our rough estimates suggest a few hundred K, consistent with AlH being located in the outer atmosphere of Mira, i.e.  $2.5-4 R_\star$ .

Another known electronic system of AlH,  $C^1\Pi - X^1\Sigma$ , is located in the UV range near 2240 Å (Szajna & Zachwieja 2010), but we found no evidence for it in the UV spectra of Mira from IUE, HST, and GALEX.

### 4.3. Atomic aluminum

**AlI absorption:** We examined the behavior of the resonance doublet  $3p^2P-4s^2S$  of AlI at 3944.01 and 3961.5 Å (i.e. in between the two strong H&K lines of Ca II) which is covered by many of our spectra. These are shown in a time sequence in Fig. C.1. Unlike most lines of neutral atoms in Mira's spectrum, lines of AlI show strong and very broad absorption profiles. The large width of these lines in *o* Ceti and other Mira variables was noticed previously by Joy (1954) and Merrill et al. (1962). The profiles change dramatically in shape and depth over time. Typically, they are triangular in shape and considerably sharper than a Lorentzian profile; the full base-widths are  $<2.5$  Å, but the actual width is likely higher as the observed pseudocontinuum is below the true continuum level. Often, close to minimum light ( $\varphi \sim 0.6$ ), the lines turn into parabolic features which can be as broad as 10 Å (full width in the stronger  $\lambda 3961$  line). On occasion (e.g. on 2009-07-24 & 2009-09-23), they appear as multi-component irregular absorption features. The blue and red wings show strong asymmetries independent of the overall shape of the AlI profile whether parabolic or sharp.

In stars of spectral types G–K, the blue resonance lines of AlI are formed just above the photosphere (Mauas et al. 2002). No detailed models exist for stars of later spectral types but one might expect that in M-type stars the lines form very close to the photosphere as well. The large apparent width of the lines support this expectation. The AlI lines are broadened mainly by the radiative and van der Waals effects (cf. Mauas et al. 2002), where the latter is dependent on the local density. The large width of the

observed AlI lines in Mira requires high local densities such as those expected close to the photosphere. The observed absorption is therefore a signature of photospheric AlI. The occasional broadening and reshaping of these spectral features may be associated with a shock passing the photosphere. We were able to reproduce the observed shape of the AlI features with stationary model atmospheres of MARCS (Gustafsson et al. 2008) after increasing the continuum opacity in the spectral range investigated<sup>11</sup>, thus assuring us that the AlI features form close to the photosphere. Although we attempted to derive the AlI abundances with model atmospheres, we encountered problems in the definition of the true continuum level and all opacity sources in this spectral region. As a result, we were unable to determine a reliable quantitative estimate of the Al abundance.

**AlI emission:** In at least six out of the 23 spectra that covered the AlI lines, weak emission components in the cores of the absorption profiles were identified. The emission is blueshifted with respect to the center of the absorption profile. On dates when the absorption profiles are very narrow, a separate emission line is not seen, but an emission component that partially fills the core of the absorption profile is implied from the asymmetry of the feature. We measured the location of the emission peaks for three dates when the emission component was well separated from the absorption wings, but did not correct for the underlying and highly asymmetric absorption profile:  $V_h=+37$  km s<sup>-1</sup> on 2007-01-30 ( $\varphi = 0.92$ );  $+57$  km s<sup>-1</sup> on 2007-09-04 ( $\varphi = 0.57$ ); and  $+47$  km s<sup>-1</sup> on 2008-08-29 ( $\varphi = 0.65$ ), where the formal uncertainties in the centroid positions are less than 1 km s<sup>-1</sup>. The measurements may be affected by a shift caused by the underlying absorption core. To show displacements of up to 20 km s<sup>-1</sup> from the center-of-mass velocity, the blueshifted emission must arise next to the shock when it is still deep in the stellar atmosphere. The displacements are comparable to or even higher than the blueshift observed in CO  $\Delta v=3$  lines ( $\Delta V_{\text{blue}} \approx 13$  km s<sup>-1</sup>) which is usually associated with the deepest observable layers of the star (Hinkle et al. 1984; Nowotny et al. 2010). Because the details of the excitation mechanism that gives rise to the emission is not known, we are unable to assess the amount of material responsible for the emission.

We did not identify either absorption or emission features that might suggest there is a substantial amount of atomic Al in the outer atmosphere and wind of Mira, implying that Al is locked in molecules (and dust) above the photosphere.

**AlII and AlIII** We also searched in the optical spectra for ionic forms of Al. The lowest-excitation line of AlII covered by our spectra has  $E_{\text{low}}=83\,800$  K. A very weak absorption line is found at the expected wavelength  $\lambda_{\text{lab}}=4663.05$  Å but shifted to the stellar radial velocity. This line is expected to be weak owing to a small Einstein coefficient,  $A_{\text{up,low}} \approx 10^5$  s<sup>-1</sup>, and very large excitation potential. With the local spectral line density, it is very likely that the observed feature belongs to another atomic ion. Indeed, in the atlas of Arcturus (Hinkle et al. 2000), the line is identified as belonging to Fe II. The feature changes its velocity systematically with a highest excursion toward the blue of  $\Delta V=-7$  km s<sup>-1</sup> near  $\varphi=0.6$ . The next lowest-excitation line of AlII covered in our spectra has  $E_{\text{low}}=120\,000$  K and  $A_{\text{up,low}}$  that is two orders of magnitude larger. Despite the much larger  $A_{\text{up,low}}$ , there is

<sup>11</sup> The extra opacity was introduced to explain the profiles of the H&K lines of Ca II. The problem of missing opacity around the lines in G and K giants was identified by Short & Lester (1994, 1996).

nothing conspicuous near its location ( $\lambda_{\text{lab}}=4663.05 \text{ \AA}$ ). The line may require too high an excitation to be effectively populated. The best test for the presence of Al II would be an observation of the resonance line with the rest wavelength of  $2669.1 \text{ \AA}$ . Al-though it was covered in several UV spectra in the literature or available in the archives, the line does not seem to be present. Reimers & Cassatella (1985) identified one weak emission feature of the resonance doublet of Al III, at  $1854.7/1862.6 \text{ \AA}$ , in their IUE spectra. Whether this feature arises near Mira A or B is questionable and so is the identification. We conclude that our observational material and the literature data are not suitable to trace the ionic forms of Al in Mira, and their contribution to the total aluminum content are likely insignificant.

## 5. Summary and discussion

### 5.1. Currently accessible Al-bearing species

In the previous sections, we have attempted to identify the main gas-phase carriers of Al in the circumstellar environment of Mira. We found neutral atomic aluminum, Al I, in the photosphere and occasionally being excited above the photosphere. The molecules AlH, AlO, and AlOH are present mostly above the photosphere, in a region where the formation of alumina dust is thought to take place ( $\gtrsim 2 R_*$ ). There is a tentative indication that AlOH may extend farther from the star and is present in the wind seen against the UV continuum of the companion. Of all these species, we were able to derive quantitative information on the amount of AlO. The observed features are variable in intensity and show modest changes in their Doppler shifts. We excluded the possibility that other simple Al-bearing species are easily accessible for mm-wave observations, such as AlF, AlCl, AlCN, AlNC, and AIS. The contribution of gas-phase Al<sub>2</sub>, AlO<sub>2</sub>, and Al<sub>2</sub>O to the total content of Al in the envelope of Mira remains unknown.

The observability of a given species alone does not directly imply that it has a high abundance, especially with data obtained at different sensitivities. Our observations show, however, that AlH, AlO, AlOH, and Al I are viable species for tracing gas-phase aluminum in circumstellar envelopes. Their relative emission distributions and time variability provide important observational constraints that can be directly compared to chemical models. For example, the role of AlH was omitted in some earlier chemical studies (e.g. Gail & Sedlmayr 1998), although it is an important observable species. The most recent models of Gobrecht et al. (2016) include AlH in the reaction network and our observations confirm that it is an important tracer of Al.

### 5.2. Circumstellar chemistry: observations vs. models

We derive an average AlO abundance of  $10^{-9}$ – $10^{-7}$  with a high uncertainty owing to the unknown content and form of hydrogen. Kamiński et al. (2013) obtained a similar abundance of  $\sim 10^{-8}$  for AlO in the envelope of the red supergiant VY CMa that was derived from optical emission bands. The agreement between the two sources suggests that the processes governing aluminum chemistry in the envelopes of evolved late-type stars of different masses and different mass-loss rates may be similar.

The non-equilibrium model with condensation of IK Tau (Gobrecht et al. 2016) show that the abundances of Al-bearing species vary with the stellar pulsation phase. Our observations of *o* Ceti show that the lines are variable but we are unable to distinguish between the variable excitation conditions and the change in the column of gas. Also, the variability we observe is

not well correlated with phase, contrary to the key assumption in the model. The model gives an AlO abundance of  $10^{-6}$  in the shocked photosphere which decreases to  $10^{-10}$ – $10^{-8}$  between 2 and  $5 R_*$  for IK Tau (Cherchneff, priv. comm.). The latter abundance is close to  $10^{-9}$ – $10^{-7}$  we derived for the extended atmosphere of *o* Ceti (Sect. 3.5). A physico-chemical model of *o* Ceti is required to better reproduce the observed characteristics of Al-bearing species in this object.

The chemical models predict that most Al-bearing molecules are destroyed above the photosphere by the pulsation shock and then reformed higher up in the atmosphere (Gobrecht et al. 2016). Therefore, one would expect to see in our best-resolution data a gap (depletion zone) in the AlO distribution just above the pulsation shock if the discontinuity is thick enough. The region from  $1 R_*$  to  $\sim 3 R_*$ , where one would expect such a discontinuity, is very difficult to interpret in our data. The presence of absorption toward the stellar photosphere complicates the picture at angular scales comparable to the ALMA restoring beam, because emission and absorption are indistinctly convolved and mutually affect the image reconstruction of each other (Appendix B). Another complication is the patchy structure of the emission at angular scales comparable to the stellar size. Our data do not allow us to verify the presence of such a gap and it may well be that this region is within the radio photosphere, at  $r < 1.6 R_*$ , where we had no access with the current ALMA observations. Since the ALMA observations were obtained at a visual phase of about 0.5, near minimum light when the star is expected to be largest, corresponding observations closer to maximum light would peer deeper into the material surrounding the star.

Much more astronomical spectroscopic observations (preferably taken with a high angular resolution), more physically realistic models, and supporting laboratory spectroscopic measurements are needed to advance our understanding of the complex chemistry of AGB stars.

### 5.3. AlO and alumina dust formation in Mira

AlO is the a crucial gas-phase Al-bearing species for alumina dust formation, because the dimerisation of AlO followed by the oxygenation of the AlO dimers produce Al<sub>2</sub>O<sub>3</sub>, which in turn forms dimers and small alumina clusters (Sarangi & Cherchneff 2015). Therefore, the chemical production of AlO determines the efficiency of alumina-dust formation and, consequently, is also linked to the gas-to-dust mass ratio. The formation of alumina dust is expected mainly at very high *dust* temperatures of about 1700 K. Interferometric observations in the MIR show that the alumina dust indeed forms very close to the photospheres of AGB stars, i.e. at  $r \approx 2 R_*$  (e.g. Karovicova et al. 2013). In *o* Ceti, the hottest dust is observed as close as  $30 \text{ mas} = 2 R_*$  (Lopez et al. 1997; Degiacomi et al. 1992), but it has not been definitely established whether it is alumina or silicate dust. Here we assume that at such close proximity to the star the hot dust is Al<sub>2</sub>O<sub>3</sub>. Silicates are unlikely to condense there because Wong et al. (2016) have recently shown that considerable depletion of SiO takes place in Mira at radii above  $4 R_*$ . It is important to note here that  $2 R_*$  is only the inner radius at which the alumina condensation and AlO depletion starts and that the process may continue farther from the star.

Our high-resolution ALMA data provide a view of the AlO distribution in unprecedented detail with the beam corresponding to approximately  $2 R_*$ . Here we discuss how these observations can be understood within the context of alumina dust formation.

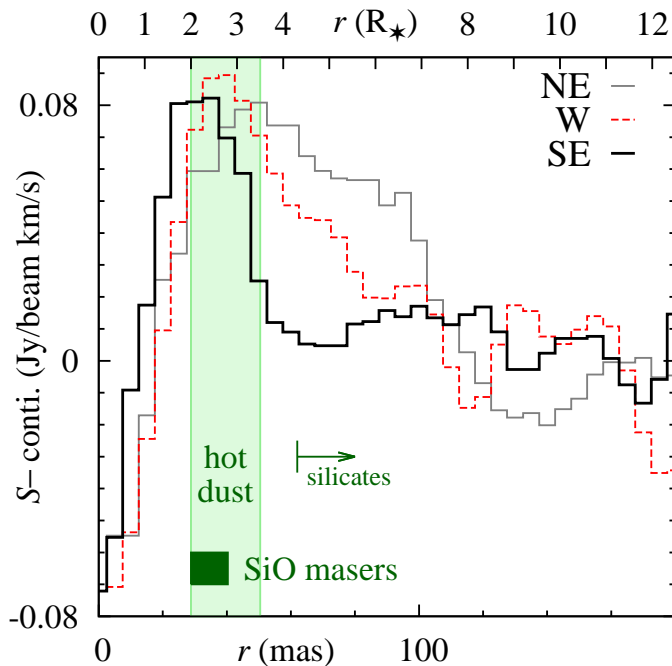


**Fig. 9.** Spatial cuts of the AIO 6→5 emission imaged by ALMA. The radial profiles extend from the center of the star and represent three position angles: 54° (nearly northeast), 133° (south-east), and −90° (west), shown in Fig. 3. Marked in green are characteristic locations within the envelope: the region closest to the star where hot dust has been observed in minimum/maximum light (inner/outer edge) (light green); the range of SiO maser rings (dark green); and the innermost radius where silicate dust is thought to condense in Mira stars (marked as “silicates”).

#### Average AIO abundance as a function of radius for $r \gtrsim 3R_*$

As mentioned in Sect. 3.2, the azimuthally-averaged brightness of AIO emission follows approximately a power law at radii  $\gtrsim 2R_{\text{ph,mm}}$  or  $\gtrsim 3R_*$  (Fig. 2). The observed brightness profile reflects the total density changes, excitation conditions, and possible abundance variations of AIO. The emission brightness changes only slowly with temperature because the brightness is proportional to  $\exp(-1/T_{\text{ex}})$  and the temperature changes approximately as  $r^{-0.3}$  (Wong et al. 2016). Although the envelope is inhomogeneous and the velocity field is complicated, to a first approximation one might expect that the total density decreases as  $r^{-2}$ . The models of Mira’s envelope suggest even steeper power laws of  $r^{-3}$  (Wong et al. 2016; Ireland et al. 2011) while NIR observations of dust in *o* Ceti require the dust density to decrease as  $r^{-1.5}$  (Lopez et al. 1997). The data can be reproduced by all these power laws equally well owing to the large scatter caused by local inhomogeneities (Fig. 4). As a result, the average profile suggests that no significant AIO depletion takes place at radii  $\gtrsim 3R_*$ .

#### AIO radial profiles in specific directions—a proof for depletion?

If we ignore the brightest emission clumps east and north/north-west from the star in Fig. 3, the AIO emission is limited to a horseshoe-shaped ring of radius  $2R_*$ . The emitting material is likely located in the plane of the sky. In Fig. 9, we show three spatial cuts through this structure along three position angles of 54° (nearly northeast), 133° (south-east), and −90° (west) and extending from the absorption center (Fig. 3). While two of those spatial cuts are in qualitative agreement with the average radial profile, the southeast cut shows distinctively a narrow feature with the line flux that practically disappears at a radius of  $3.5R_*$ ,

i.e. exactly in the region where hot dust has been observed in Mira. If we interpret the emission intensity as corresponding directly to the column density of AIO (i.e. the excitation conditions do not change much with radius), then this profile is exactly what one would expect if substantial depletion of AIO began at about  $2R_*$ . It is tempting to interpret this AIO deficit as depletion onto dust. It would be interesting to verify this depletion scenario by checking whether there is a dust-rich clump at the radial extension of this spatial cut beyond  $3R_*$ , but it is not possible to perform this test with the currently available data. Although there is no strong proof in our data for global AIO depletion, it may be that the gas-phase AIO is consumed by other species only in particular directions.

#### AIO variability and clumpiness vs. episodic dust production

The ALMA maps of the  $N=6 \rightarrow 5$  transition (Fig. 3) provide a detailed glimpse of the clumpy distribution of AIO gas very close to the photosphere. Together with data presented in Wong et al. (2016), they provide the first direct view of the inhomogeneities in the cool molecular layer at about  $2R_*$ . The existence of such inhomogeneities has been implied in *o* Ceti before (e.g. Wittkowski et al. 2016, and references therein) and in other oxygen-rich AGB stars (e.g. Haubois et al. 2015; Ohnaka et al. 2016). The clumps are close to the star and are likely to be transient, which is strongly supported by the variability of AIO observed in the rotational and electronic lines reported here.

The question which naturally arises is whether the complex spatial and temporal characteristics of AIO can influence the dust production. The dust produced around Mira has a very inhomogeneous distribution and its spectral features change with time (Lopez et al. 1997; Lobel et al. 2000). Mira’s flux variability in the range 8–11  $\mu\text{m}$  cannot be explained by the light changes of the star alone, rather some variations of the dust density must also occur (Lopez et al. 1997). It has been suggested in the literature that the dust production in AGB stars is in fact episodic and may occur during some phases or only in some cycles (cf. Lopez et al. 1997, and references therein). Because the production of alumina dust is chemically directly linked to the production of AIO, the clumpy distribution and time variability of AIO emission presented here may be the direct cause of the observed spatial and temporal characteristics of dust. Identifying the process that makes the molecular emission clumpy is beyond the scope of this paper but it is very likely linked to phenomena in the stellar photosphere. Localized shocks related to convection (Schwarzschild 1975) are good candidates to explain the observational features of some AGB stars (e.g. Ohnaka et al. 2016; Haubois et al. 2015) and red supergiants (e.g. Ohnaka et al. 2009). The episodic appearance of visual emission bands of AIO requiring shock excitation supports such an interpretation.

**Link of the AIO emission to faint-maxima cycles?** The occurrence of emission in electronic bands of AIO in Mira is very rare. It was reported for the first time in 1924. The first identification of AIO bands was made by Baxandall (1928), who used spectra of Joy (1926) (these authors assigned the features to  $\text{Al}_2\text{O}_3$ ). Emission was also reported for the 1964 maximum of Mira by Keenan et al. (1969). The search for AIO emission in Mira was continued by Kipper & Kipper (1979), but their observation of



the  $\Delta v=0$  sequence in 1978 did not reveal any emission<sup>12</sup>. Our observational data add two more episodes of AIO emission to the record.

The occurrences of AIO bands in emission were reported to proceed cycles with fainter-than-average visual maxima (cf. Fig. 7) which are rare. In the last century, maxima with  $\text{Vis.} \geq 4$  mag occurred only 5–8 times: in 1924, 1976, 1978, 1984, 1998/99, and possibly also in 1912, 1913, and 1931 (the photometric coverage is incomplete near these maxima). Emission was observed in 1924 over a few weeks (Keenan et al. 1969). Garrison (1997) observed Mira during most maxima in 1916–1997 and noticed that AIO emission appears in weak cycles. Our 1998/1999 observation of the AIO emission also coincided with a faint maximum. However, the 2007 observation of the AIO emission event proceeded a normal cycle. This raises the question as to whether there is a direct correspondence between AIO emission and faint maxima.

The existence of such a correlation would be very intriguing in the context of metal-oxide formation and variable dust production of Mira. One possibility is that faint maxima occur owing to enhanced dust production which would increase the extinction and reduce the optical fluxes of the star. Alternatively, some cycles may be dimmer due to increased production of TiO and other metal oxides which constitute the main opacity source in Miras and are directly responsible for their high-amplitude light variations in the visual (Reid & Goldston 2002). However the literature and our observations of AIO (and TiO) emission show that there is no established direct link between the occurrences of molecular emission and faint maxima.

Here, we prefer an interpretation in which the emission episodes in the electronic features of AIO and AlI are associated with shocks which are stronger than average and were also proposed to explain other inter-cycle phenomena in Mira variables (e.g. Richter et al. 2003; Lopez et al. 1997).

#### 5.4. Final words and prospects

The challenges in tracing gas-phase species important for dust formation are identified in the current study. We have demonstrated that the complex excitation of gas very near the stellar photosphere – influenced strongly by repetitive, irregular, and merging shocks – is the main obstacle in deriving abundances and more sophisticated analysis tools are necessary to interpret the data. A conclusive test of dust nucleation in stellar envelopes is possible but it will require a substantial observing effort. In particular, the most fruitful would be observations of a multitude of spectral lines with the highest angular resolution (as afforded primarily with the most extended ALMA configurations) conducted nearly simultaneously with IR/MIR interferometric observations of dust features.

## References

Alcolea, J., Bujarrabal, V., Planesas, P., et al. 2013, *A&A*, 559, A93  
 ALMA Partnership, Fomalont, E. B., Vlahakis, C., et al. 2015, *ApJ*, 808, L1  
 Alpaslan, M. 2009, arXiv:0912.4755  
 Alvarez, R., Jorissen, A., Plez, B., et al. 2001, *A&A*, 379, 305  
 Apponi, A. J., Barclay, W. L., Jr., & Ziurys, L. M. 1993, *ApJ*, 414, L129  
 Arkharov, A. A., Hagen-Torn, E. I., Puzakova, T. U., & Ruban, E. V. 2005, *Astrophysics*, 48, 143  
 Banerjee, D. P. K., Varricatt, W. P., Mathew, B., Launila, O., & Ashok, N. M. 2012, *ApJ*, 753, L20

Baxandall, F. E. 1928, *MNRAS*, 88, 679  
 Bester, M., Danchi, W. C., Degiacomi, C. G., Townes, C. H., & Geballe, T. R. 1991, *ApJ*, 367, L27  
 Cherchneff, I. 2006, *A&A*, 456, 1001  
 Cherchneff, I. 2013, *EAS Publications Series*, 60, 175  
 Cho, S.-H., Kaifu, N., & Ukita, N. 1996, *AJ*, 111, 1987  
 Cernicharo, J., Teyssier, D., Quintana-Lacaci, G., et al. 2014, *ApJ*, 796, L21  
 Cotton, W. D., Vlemmings, W., Mennesson, B., et al. 2006, *A&A*, 456, 339  
 Degiacomi, C. G., Bester, M., Danchi, W. C., Greenhill, L. J., & Townes, C. H. 1992, *ESO Conf. and Workshop Proceedings*, 39, 681  
 Dayou, F., & Balança, C. 2006, *A&A*, 459, 297  
 Fabas, N., Lèbre, A., & Gillet, D. 2011, *A&A*, 535, A12  
 Fox, M. W., Wood, P. R., & Dopita, M. A. 1984, *ApJ*, 286, 337  
 Gail, H.-P., & Sedlmayr, E. 1998, *Faraday Discussions*, 109, 303  
 Garrison, R. F. 1997, *Journal of the American Association of Variable Star Observers (JAAVSO)*, 25, 70  
 Garrison, R. F., Hui, F., Liska, J., et al. 1999, *Bulletin of the American Astr. Society*, 31, 929  
 Gerard, E., & Bourgois, G. 1993, *Astrophysical Masers*, 412, 365  
 Gillet, D., Debieve, J. F., Fokin, A. B., & Mazaauric, S. 1998, *A&A*, 332, 235  
 Gobrecht, D., Cherchneff, I., Sarangi, A., Plane, J. M. C., & Bromley, S. T. 2016, *A&A*, 585, A6  
 Goldsmith, P. F., & Langer, W. D. 1999, *ApJ*, 517, 209  
 Goto, M., & Saito, S. 1995, *ApJ*, 452, L147  
 Gray, M. D., Humphreys, E. M. L., & Yates, J. A. 1999, *MNRAS*, 304, 906  
 Gustafsson, B., Edvardsson, B., Eriksson, K., et al. 2008, *A&A*, 486, 951  
 Haubois, X., Wittkowski, M., Perrin, G., et al. 2015, *A&A*, 582, A71  
 Haniff, C. A., Ghez, A. M., Gorham, P. W., et al. 1992, *AJ*, 103, 1662  
 Herbig, G. H. 1956, *PASP*, 68, 204  
 Herbig, G. H., & Zappala, R. R. 1968, *ZAp*, 68, 423  
 Hinkle, K. H. 1978, *ApJ*, 220, 210  
 Hinkle, K. H., Scharlach, W. W. G., & Hall, D. N. B. 1984, *ApJS*, 56, 1  
 Hinkle, K., Wallace, L., Valenti, J., & Harmer, D. 2000, *Visible and Near Infrared Atlas of the Arcturus Spectrum 3727-9300 Å* ed. K. Hinkle, L. Wallace, J. Valenti, and D. Harmer. (San Francisco: ASP) ISBN: 1-58381-037-4, 2000  
 Höfner, S. 2008, *A&A*, 491, L1  
 Ireland, M. J., Monnier, J. D., Tuthill, P. G., et al. 2007, *ApJ*, 662, 651  
 Ireland, M. J., Scholz, M., & Wood, P. R. 2011, *MNRAS*, 418, 114  
 Ireland, M. J. 2011, *Why Galaxies Care about AGB Stars II: Shining Examples and Common Inhabitants*, 445, 83  
 Jeong, K. S., Winters, J. M., Le Bertre, T., & Sedlmayr, E. 2003, *A&A*, 407, 191  
 Joy, A. H. 1926, *ApJ*, 63, 281  
 Joy, A. H. 1954, *ApJS*, 1, 39  
 Karovska, M., Hack, W., Raymond, J., & Guinan, E. 1997, *ApJ*, 482, L175  
 Kamiński, T., Gottlieb, C. A., Menten, K. M., et al. 2013, *A&A*, 551, A113  
 Kamiński, T., Gottlieb, C. A., Young, K. H., Menten, K. M., & Patel, N. A. 2013, *ApJS*, 209, 38  
 Kamiński, T., Schmidt, M. R., & Menten, K. M. 2013, *A&A*, 549, A6  
 Kamiński, T., Mason, E., Tylenda, R., & Schmidt, M. R. 2015, *A&A*, 580, A34  
 Karakas, A. I., & Lattanzio, J. C. 2003, *PASA*, 20, 279  
 Karovicova, I., Wittkowski, M., Ohnaka, K., et al. 2013, *A&A*, 560, A75  
 Keenan, P. C., Deutsch, A. J., & Garrison, R. F. 1969, *ApJ*, 158, 261  
 Kimata, R., & Izumiura, H. 2003, *Planetary Nebulae: Their Evolution and Role in the Universe*, 209, 69  
 Kipper, T. A., & Kipper, M. A. 1979, *Publications of the Tartu Astrofizika Observatory*, 47, 222  
 Knapp, G. R., Pourbaix, D., Platais, I., & Jorissen, A. 2003, *A&A*, 403, 993  
 Labeyrie, A., Koechlin, L., Bonneau, D., Blazit, A., & Foy, R. 1977, *ApJ*, 218, L75  
 Li, S., Sattelmeyer, K. W., Yamaguchi, Y., & Schaefer, H. F. 2003, *J. Chem. Phys.*, 119, 12830  
 Little-Marenin, I. R., & Little, S. J. 1990, *AJ*, 99, 1173  
 Lobel, A., Bagnulo, S., Doyle, J. G., & Power, C. 2000, *MNRAS*, 317, 391  
 Lopez, B., Danchi, W. C., Bester, M., et al. 1997, *ApJ*, 488, 807  
 Lorenz-Martins, S., & Pompeia, L. 2000, *MNRAS*, 315, 856  
 Mangum, J. G., & Shirley, Y. L. 2015, *PASP*, 127, 266  
 Martinez, A., Bujarrabal, V., & Alcolea, J. 1988, *A&AS*, 74, 273  
 Matthews, L. D., Reid, M. J., & Menten, K. M. 2015, *ApJ*, 808, 36  
 Mauas, P. J. D., Borda, R. F., & Luoni, M. L. 2002, *ApJS*, 142, 285  
 Merrill, P. W., Deutsch, A. J., & Keenan, P. C. 1962, *ApJ*, 136, 21  
 Mohamed, S., & Podsiadlowski, P. 2012, *Baltic Astronomy*, 21, 88  
 Müller, H. S. P., Schlöder, F., Stutzki, J., & Winnewisser, G. 2005, *J. Mol. Struct.*, 742, 215  
 Nguyen, A. N., Keller, L. P., & Messenger, S. 2016, *ApJ*, 818, 51  
 Nhung, P. T., Hoai, D. T., Diep, P. N., et al. 2016, arXiv:1603.00148  
 Nittler, L. R., Alexander, C. M. O., Gallino, R., et al. 2008, *ApJ*, 682, 1450  
 Nowotny, W., Höfner, S., & Aringer, B. 2010, *A&A*, 514, A35  
 Ohnaka, K., Hofmann, K.-H., Benisty, M., et al. 2009, *A&A*, 503, 183  
 Ohnaka, K., Weigelt, G., & Hofmann, K.-H. 2016, arXiv:1603.01197  
 Pardo, J. R., Alcolea, J., Bujarrabal, V., et al. 2004, *A&A*, 424, 145

<sup>12</sup> Their spectral resolutions (dispersions of 24 and 12 Å/mm) might have been too low to detect weak emission, especially when mixed with an absorption profile.



- Patel, N. A., Young, K. H., Brünken, S., et al. 2009, *ApJ*, 691, L55
- Perrin, G., Ridgway, S. T., Mennesson, B., et al. 2004, *A&A*, 426, 279
- Pickett, H. M., Poynter, R. L., Cohen, E. A., et al. 1998, *J. Quant. Spectr. Rad. Transf.*, 60, 883
- Pilgrim, J. S., Robbins, D. L., & Duncan, M. A. 1993, *Chemical Physics Letters*, 202, 203
- Planesas, P., Alcolea, J., & Bachiller, R. 2016, *A&A*, 586, A69
- Polehampton, E., & Hafok, H., APEX Calibration and Data Reduction Manual, APEX-MPI-MAN-0012, 2013, <http://www.apex-telescope.org/documents/public/APEX-MPI-MAN-0012.pdf>
- Patrascu, A. T., Yurchenko, S. N., & Tennyson, J. 2015, *MNRAS*, 449, 3613
- Reimers, D., & Cassatella, A. 1985, *ApJ*, 297, 275
- Ramstedt, S., Mohamed, S., Vlemmings, W. H. T., et al. 2014, *A&A*, 570, L14
- Reid, M. J., & Goldston, J. E. 2002, *ApJ*, 568, 931
- Reid, M. J., & Menten, K. M. 2007, *ApJ*, 671, 2068
- Richter, H., Wood, P. R., Woitke, P., Bolick, U., & Sedlmayr, E. 2003, *A&A*, 400, 319
- Richter, H., & Wood, P. R. 2001, *A&A*, 369, 1027
- Ryde, N., & Schöier, F. L. 2001, *ApJ*, 547, 384
- Sarangi, A., & Cherchneff, I. 2015, *A&A*, 575, A95
- Schwarzschild, M. 1975, *ApJ*, 195, 137
- Sharp, C. M., & Huebner, W. F. 1990, *ApJS*, 72, 417
- Shenavrin, V. I., Taranova, O. G., & Nadzhip, A. E. 2011, *VizieR Online Data Catalog*, 808, 80034
- Short, C. I., & Lester, J. B. 1994, *ApJ*, 436, L165
- Short, C. I., & Lester, J. B. 1996, *ApJ*, 469, 898
- Sokoloski, J. L., & Bildsten, L. 2010, *ApJ*, 723, 1188
- Stewart, P. N., Tuthill, P. G., Hedman, M. M., Nicholson, P. D., & Lloyd, J. P. 2013, *MNRAS*, 433, 2286
- Szajna, W., & Zachwieja, M. 2010, *Journal of Molecular Spectroscopy*, 260, 130
- Szajna, W., & Zachwieja, M. 2009, *European Physical Journal D*, 55, 549
- Templeton, M. R., & Karovska, M. 2009, *ApJ*, 691, 1470
- Tenenbaum, E. D., & Ziurys, L. M. 2010, *ApJ*, 712, L93
- Tomasella, L., Munari, U., & Zwitter, T. 2010, *AJ*, 140, 1758
- Tsuji, T. 2000, *ApJ*, 540, L99
- van der Tak, F. F. S., Black, J. H., Schöier, F. L., Jansen, D. J., & van Dishoeck, E. F. 2007, *A&A*, 468, 627
- Vlemmings, W. H. T., Ramstedt, S., O’Gorman, E., et al. 2015, *A&A*, 577, L4
- Vollmer, C., Hoppe, P., Brenker, F., & Palme, H. 2006, 37th Annual Lunar and Planetary Sci. Conf., 37, 1284
- Western, C. M., 2014, University of Bristol Research Data Repository, doi:10.5523/bris.hufggvpcuc1zvliqed497r2
- Whitelock, P., Marang, F., & Feast, M. 2000, *MNRAS*, 319, 728
- Willacy, K., & Cherchneff, I. 1998, *A&A*, 330, 676
- Willmarth, D & Barnes, J. 1994, A User’s Guide to Reducing Echelle Spectra with IRAF, <http://iraf.net/irafdocs/ech/>
- Willson, L. A., Wallerstein, G., & Pilachowski, C. A. 1982, *MNRAS*, 198, 483
- Woitke, P., Helling, C., Winters, J. M., & Jeong, K. S. 1999, *A&A*, 348, L17
- Wittkowski, M., Chiavassa, A., Freytag, B., et al. 2016, *A&A*, 587, A12
- Wong, K. T., Kamiński, T., Menten, K. M., & Wyrowski, F. 2016, arXiv:1603.03371
- Woodruff, H. C., Eberhardt, M., Driebe, T., et al. 2004, *A&A*, 421, 703
- Yamada, C., Fujitake, M., Hirota, E., & Cohen, E. A. 1990, *J. Chem. Phys.*, 92, 2146
- Young, K. 1995, *ApJ*, 445, 872
- Zamanov, R. K., Bode, M. F., Melo, C. H. F., et al. 2006, *MNRAS*, 365, 1215
- Zhao-Geisler, R., Quirrenbach, A., Köhler, R., & Lopez, B. 2012, *A&A*, 545, A56
- Ziurys, L. M., Apponi, A. J., & Phillips, T. G. 1994, *ApJ*, 433, 729
- Ziurys, L. M., Savage, C., Highberger, J. L., et al. 2002, *ApJ*, 564, L45

Council of Canada. Herschel is an ESA space observatory with science instruments provided by European-led Principal Investigator consortia and with important participation from NASA. This research has made use of the Keck Observatory Archive (KOA), which is operated by the W. M. Keck Observatory and the NASA Exoplanet Science Institute (NExScI), under contract with the National Aeronautics and Space Administration. Based on analysis carried out with the CASSIS software and JPL spectroscopic database. CASSIS has been developed by IRAP-UPS/CNRS (<http://cassis.irap.omp.eu>). This paper makes use of the following ALMA data: ADS/JAO.ALMA#2011.0.00014.SV, 2011.0.00015.SV, 2011.0.00016.SV, 2011.0.00017.SV, 2011.0.00018.SV, 2011.0.00019.SV, 2011.0.00020.SV, 2011.0.00021.SV, 2011.0.00022.SV, 2011.0.00023.SV, 2011.0.00024.SV, 2011.0.00025.SV, 2011.0.00026.SV, 2011.0.00027.SV, 2011.0.00028.SV, 2011.0.00029.SV, 2011.0.00030.SV, 2011.0.00031.SV, 2011.0.00032.SV, 2011.0.00033.SV, 2011.0.00034.SV, 2011.0.00035.SV, 2011.0.00036.SV, 2011.0.00037.SV, 2011.0.00038.SV, 2011.0.00039.SV, 2011.0.00040.SV, 2011.0.00041.SV, 2011.0.00042.SV, 2011.0.00043.SV, 2011.0.00044.SV, 2011.0.00045.SV, 2011.0.00046.SV, 2011.0.00047.SV, 2011.0.00048.SV, 2011.0.00049.SV, 2011.0.00050.SV, 2011.0.00051.SV, 2011.0.00052.SV, 2011.0.00053.SV, 2011.0.00054.SV, 2011.0.00055.SV, 2011.0.00056.SV, 2011.0.00057.SV, 2011.0.00058.SV, 2011.0.00059.SV, 2011.0.00060.SV, 2011.0.00061.SV, 2011.0.00062.SV, 2011.0.00063.SV, 2011.0.00064.SV, 2011.0.00065.SV, 2011.0.00066.SV, 2011.0.00067.SV, 2011.0.00068.SV, 2011.0.00069.SV, 2011.0.00070.SV, 2011.0.00071.SV, 2011.0.00072.SV, 2011.0.00073.SV, 2011.0.00074.SV, 2011.0.00075.SV, 2011.0.00076.SV, 2011.0.00077.SV, 2011.0.00078.SV, 2011.0.00079.SV, 2011.0.00080.SV, 2011.0.00081.SV, 2011.0.00082.SV, 2011.0.00083.SV, 2011.0.00084.SV, 2011.0.00085.SV, 2011.0.00086.SV, 2011.0.00087.SV, 2011.0.00088.SV, 2011.0.00089.SV, 2011.0.00090.SV, 2011.0.00091.SV, 2011.0.00092.SV, 2011.0.00093.SV, 2011.0.00094.SV, 2011.0.00095.SV, 2011.0.00096.SV, 2011.0.00097.SV, 2011.0.00098.SV, 2011.0.00099.SV, 2011.0.00100.SV, 2011.0.00101.SV, 2011.0.00102.SV, 2011.0.00103.SV, 2011.0.00104.SV, 2011.0.00105.SV, 2011.0.00106.SV, 2011.0.00107.SV, 2011.0.00108.SV, 2011.0.00109.SV, 2011.0.00110.SV, 2011.0.00111.SV, 2011.0.00112.SV, 2011.0.00113.SV, 2011.0.00114.SV, 2011.0.00115.SV, 2011.0.00116.SV, 2011.0.00117.SV, 2011.0.00118.SV, 2011.0.00119.SV, 2011.0.00120.SV, 2011.0.00121.SV, 2011.0.00122.SV, 2011.0.00123.SV, 2011.0.00124.SV, 2011.0.00125.SV, 2011.0.00126.SV, 2011.0.00127.SV, 2011.0.00128.SV, 2011.0.00129.SV, 2011.0.00130.SV, 2011.0.00131.SV, 2011.0.00132.SV, 2011.0.00133.SV, 2011.0.00134.SV, 2011.0.00135.SV, 2011.0.00136.SV, 2011.0.00137.SV, 2011.0.00138.SV, 2011.0.00139.SV, 2011.0.00140.SV, 2011.0.00141.SV, 2011.0.00142.SV, 2011.0.00143.SV, 2011.0.00144.SV, 2011.0.00145.SV, 2011.0.00146.SV, 2011.0.00147.SV, 2011.0.00148.SV, 2011.0.00149.SV, 2011.0.00150.SV, 2011.0.00151.SV, 2011.0.00152.SV, 2011.0.00153.SV, 2011.0.00154.SV, 2011.0.00155.SV, 2011.0.00156.SV, 2011.0.00157.SV, 2011.0.00158.SV, 2011.0.00159.SV, 2011.0.00160.SV, 2011.0.00161.SV, 2011.0.00162.SV, 2011.0.00163.SV, 2011.0.00164.SV, 2011.0.00165.SV, 2011.0.00166.SV, 2011.0.00167.SV, 2011.0.00168.SV, 2011.0.00169.SV, 2011.0.00170.SV, 2011.0.00171.SV, 2011.0.00172.SV, 2011.0.00173.SV, 2011.0.00174.SV, 2011.0.00175.SV, 2011.0.00176.SV, 2011.0.00177.SV, 2011.0.00178.SV, 2011.0.00179.SV, 2011.0.00180.SV, 2011.0.00181.SV, 2011.0.00182.SV, 2011.0.00183.SV, 2011.0.00184.SV, 2011.0.00185.SV, 2011.0.00186.SV, 2011.0.00187.SV, 2011.0.00188.SV, 2011.0.00189.SV, 2011.0.00190.SV, 2011.0.00191.SV, 2011.0.00192.SV, 2011.0.00193.SV, 2011.0.00194.SV, 2011.0.00195.SV, 2011.0.00196.SV, 2011.0.00197.SV, 2011.0.00198.SV, 2011.0.00199.SV, 2011.0.00200.SV, 2011.0.00201.SV, 2011.0.00202.SV, 2011.0.00203.SV, 2011.0.00204.SV, 2011.0.00205.SV, 2011.0.00206.SV, 2011.0.00207.SV, 2011.0.00208.SV, 2011.0.00209.SV, 2011.0.00210.SV, 2011.0.00211.SV, 2011.0.00212.SV, 2011.0.00213.SV, 2011.0.00214.SV, 2011.0.00215.SV, 2011.0.00216.SV, 2011.0.00217.SV, 2011.0.00218.SV, 2011.0.00219.SV, 2011.0.00220.SV, 2011.0.00221.SV, 2011.0.00222.SV, 2011.0.00223.SV, 2011.0.00224.SV, 2011.0.00225.SV, 2011.0.00226.SV, 2011.0.00227.SV, 2011.0.00228.SV, 2011.0.00229.SV, 2011.0.00230.SV, 2011.0.00231.SV, 2011.0.00232.SV, 2011.0.00233.SV, 2011.0.00234.SV, 2011.0.00235.SV, 2011.0.00236.SV, 2011.0.00237.SV, 2011.0.00238.SV, 2011.0.00239.SV, 2011.0.00240.SV, 2011.0.00241.SV, 2011.0.00242.SV, 2011.0.00243.SV, 2011.0.00244.SV, 2011.0.00245.SV, 2011.0.00246.SV, 2011.0.00247.SV, 2011.0.00248.SV, 2011.0.00249.SV, 2011.0.00250.SV, 2011.0.00251.SV, 2011.0.00252.SV, 2011.0.00253.SV, 2011.0.00254.SV, 2011.0.00255.SV, 2011.0.00256.SV, 2011.0.00257.SV, 2011.0.00258.SV, 2011.0.00259.SV, 2011.0.00260.SV, 2011.0.00261.SV, 2011.0.00262.SV, 2011.0.00263.SV, 2011.0.00264.SV, 2011.0.00265.SV, 2011.0.00266.SV, 2011.0.00267.SV, 2011.0.00268.SV, 2011.0.00269.SV, 2011.0.00270.SV, 2011.0.00271.SV, 2011.0.00272.SV, 2011.0.00273.SV, 2011.0.00274.SV, 2011.0.00275.SV, 2011.0.00276.SV, 2011.0.00277.SV, 2011.0.00278.SV, 2011.0.00279.SV, 2011.0.00280.SV, 2011.0.00281.SV, 2011.0.00282.SV, 2011.0.00283.SV, 2011.0.00284.SV, 2011.0.00285.SV, 2011.0.00286.SV, 2011.0.00287.SV, 2011.0.00288.SV, 2011.0.00289.SV, 2011.0.00290.SV, 2011.0.00291.SV, 2011.0.00292.SV, 2011.0.00293.SV, 2011.0.00294.SV, 2011.0.00295.SV, 2011.0.00296.SV, 2011.0.00297.SV, 2011.0.00298.SV, 2011.0.00299.SV, 2011.0.00300.SV, 2011.0.00301.SV, 2011.0.00302.SV, 2011.0.00303.SV, 2011.0.00304.SV, 2011.0.00305.SV, 2011.0.00306.SV, 2011.0.00307.SV, 2011.0.00308.SV, 2011.0.00309.SV, 2011.0.00310.SV, 2011.0.00311.SV, 2011.0.00312.SV, 2011.0.00313.SV, 2011.0.00314.SV, 2011.0.00315.SV, 2011.0.00316.SV, 2011.0.00317.SV, 2011.0.00318.SV, 2011.0.00319.SV, 2011.0.00320.SV, 2011.0.00321.SV, 2011.0.00322.SV, 2011.0.00323.SV, 2011.0.00324.SV, 2011.0.00325.SV, 2011.0.00326.SV, 2011.0.00327.SV, 2011.0.00328.SV, 2011.0.00329.SV, 2011.0.00330.SV, 2011.0.00331.SV, 2011.0.00332.SV, 2011.0.00333.SV, 2011.0.00334.SV, 2011.0.00335.SV, 2011.0.00336.SV, 2011.0.00337.SV, 2011.0.00338.SV, 2011.0.00339.SV, 2011.0.00340.SV, 2011.0.00341.SV, 2011.0.00342.SV, 2011.0.00343.SV, 2011.0.00344.SV, 2011.0.00345.SV, 2011.0.00346.SV, 2011.0.00347.SV, 2011.0.00348.SV, 2011.0.00349.SV, 2011.0.00350.SV, 2011.0.00351.SV, 2011.0.00352.SV, 2011.0.00353.SV, 2011.0.00354.SV, 2011.0.00355.SV, 2011.0.00356.SV, 2011.0.00357.SV, 2011.0.00358.SV, 2011.0.00359.SV, 2011.0.00360.SV, 2011.0.00361.SV, 2011.0.00362.SV, 2011.0.00363.SV, 2011.0.00364.SV, 2011.0.00365.SV, 2011.0.00366.SV, 2011.0.00367.SV, 2011.0.00368.SV, 2011.0.00369.SV, 2011.0.00370.SV, 2011.0.00371.SV, 2011.0.00372.SV, 2011.0.00373.SV, 2011.0.00374.SV, 2011.0.00375.SV, 2011.0.00376.SV, 2011.0.00377.SV, 2011.0.00378.SV, 2011.0.00379.SV, 2011.0.00380.SV, 2011.0.00381.SV, 2011.0.00382.SV, 2011.0.00383.SV, 2011.0.00384.SV, 2011.0.00385.SV, 2011.0.00386.SV, 2011.0.00387.SV, 2011.0.00388.SV, 2011.0.00389.SV, 2011.0.00390.SV, 2011.0.00391.SV, 2011.0.00392.SV, 2011.0.00393.SV, 2011.0.00394.SV, 2011.0.00395.SV, 2011.0.00396.SV, 2011.0.00397.SV, 2011.0.00398.SV, 2011.0.00399.SV, 2011.0.00400.SV, 2011.0.00401.SV, 2011.0.00402.SV, 2011.0.00403.SV, 2011.0.00404.SV, 2011.0.00405.SV, 2011.0.00406.SV, 2011.0.00407.SV, 2011.0.00408.SV, 2011.0.00409.SV, 2011.0.00410.SV, 2011.0.00411.SV, 2011.0.00412.SV, 2011.0.00413.SV, 2011.0.00414.SV, 2011.0.00415.SV, 2011.0.00416.SV, 2011.0.00417.SV, 2011.0.00418.SV, 2011.0.00419.SV, 2011.0.00420.SV, 2011.0.00421.SV, 2011.0.00422.SV, 2011.0.00423.SV, 2011.0.00424.SV, 2011.0.00425.SV, 2011.0.00426.SV, 2011.0.00427.SV, 2011.0.00428.SV, 2011.0.00429.SV, 2011.0.00430.SV, 2011.0.00431.SV, 2011.0.00432.SV, 2011.0.00433.SV, 2011.0.00434.SV, 2011.0.00435.SV, 2011.0.00436.SV, 2011.0.00437.SV, 2011.0.00438.SV, 2011.0.00439.SV, 2011.0.00440.SV, 2011.0.00441.SV, 2011.0.00442.SV, 2011.0.00443.SV, 2011.0.00444.SV, 2011.0.00445.SV, 2011.0.00446.SV, 2011.0.00447.SV, 2011.0.00448.SV, 2011.0.00449.SV, 2011.0.00450.SV, 2011.0.00451.SV, 2011.0.00452.SV, 2011.0.00453.SV, 2011.0.00454.SV, 2011.0.00455.SV, 2011.0.00456.SV, 2011.0.00457.SV, 2011.0.00458.SV, 2011.0.00459.SV, 2011.0.00460.SV, 2011.0.00461.SV, 2011.0.00462.SV, 2011.0.00463.SV, 2011.0.00464.SV, 2011.0.00465.SV, 2011.0.00466.SV, 2011.0.00467.SV, 2011.0.00468.SV, 2011.0.00469.SV, 2011.0.00470.SV, 2011.0.00471.SV, 2011.0.00472.SV, 2011.0.00473.SV, 2011.0.00474.SV, 2011.0.00475.SV, 2011.0.00476.SV, 2011.0.00477.SV, 2011.0.00478.SV, 2011.0.00479.SV, 2011.0.00480.SV, 2011.0.00481.SV, 2011.0.00482.SV, 2011.0.00483.SV, 2011.0.00484.SV, 2011.0.00485.SV, 2011.0.00486.SV, 2011.0.00487.SV, 2011.0.00488.SV, 2011.0.00489.SV, 2011.0.00490.SV, 2011.0.00491.SV, 2011.0.00492.SV, 2011.0.00493.SV, 2011.0.00494.SV, 2011.0.00495.SV, 2011.0.00496.SV, 2011.0.00497.SV, 2011.0.00498.SV, 2011.0.00499.SV, 2011.0.00500.SV, 2011.0.00501.SV, 2011.0.00502.SV, 2011.0.00503.SV, 2011.0.00504.SV, 2011.0.00505.SV, 2011.0.00506.SV, 2011.0.00507.SV, 2011.0.00508.SV, 2011.0.00509.SV, 2011.0.00510.SV, 2011.0.00511.SV, 2011.0.00512.SV, 2011.0.00513.SV, 2011.0.00514.SV, 2011.0.00515.SV, 2011.0.00516.SV, 2011.0.00517.SV, 2011.0.00518.SV, 2011.0.00519.SV, 2011.0.00520.SV, 2011.0.00521.SV, 2011.0.00522.SV, 2011.0.00523.SV, 2011.0.00524.SV, 2011.0.00525.SV, 2011.0.00526.SV, 2011.0.00527.SV, 2011.0.00528.SV, 2011.0.00529.SV, 2011.0.00530.SV, 2011.0.00531.SV, 2011.0.00532.SV, 2011.0.00533.SV, 2011.0.00534.SV, 2011.0.00535.SV, 2011.0.00536.SV, 2011.0.00537.SV, 2011.0.00538.SV, 2011.0.00539.SV, 2011.0.00540.SV, 2011.0.00541.SV, 2011.0.00542.SV, 2011.0.00543.SV, 2011.0.00544.SV, 2011.0.00545.SV, 2011.0.00546.SV, 2011.0.00547.SV, 2011.0.00548.SV, 2011.0.00549.SV, 2011.0.00550.SV, 2011.0.00551.SV, 2011.0.00552.SV, 2011.0.00553.SV, 2011.0.00554.SV, 2011.0.00555.SV, 2011.0.00556.SV, 2011.0.00557.SV, 2011.0.00558.SV, 2011.0.00559.SV, 2011.0.00560.SV, 2011.0.00561.SV, 2011.0.00562.SV, 2011.0.00563.SV, 2011.0.00564.SV, 2011.0.00565.SV, 2011.0.00566.SV, 2011.0.00567.SV, 2011.0.00568.SV, 2011.0.00569.SV, 2011.0.00570.SV, 2011.0.00571.SV, 2011.0.00572.SV, 2011.0.00573.SV, 2011.0.00574.SV, 2011.0.00575.SV, 2011.0.00576.SV, 2011.0.00577.SV, 2011.0.00578.SV, 2011.0.00579.SV, 2011.0.00580.SV, 2011.0.00581.SV, 2011.0.00582.SV, 2011.0.00583.SV, 2011.0.00584.SV, 2011.0.00585.SV, 2011.0.00586.SV, 2011.0.00587.SV, 2011.0.00588.SV, 2011.0.00589.SV, 2011.0.00590.SV, 2011.0.00591.SV, 2011.0.00592.SV, 2011.0.00593.SV, 2011.0.00594.SV, 2011.0.00595.SV, 2011.0.00596.SV, 2011.0.00597.SV, 2011.0.00598.SV, 2011.0.00599.SV, 2011.0.00600.SV, 2011.0.00601.SV, 2011.0.00602.SV, 2011.0.00603.SV, 2011.0.00604.SV, 2011.0.00605.SV, 2011.0.00606.SV, 2011.0.00607.SV, 2011.0.00608.SV, 2011.0.00609.SV, 2011.0.00610.SV, 2011.0.00611.SV, 2011.0.00612.SV, 2011.0.00613.SV, 2011.0.00614.SV, 2011.0.00615.SV, 2011.0.00616.SV, 2011.0.00617.SV, 2011.0.00618.SV, 2011.0.00619.SV, 2011.0.00620.SV, 2011.0.00621.SV, 2011.0.00622.SV, 20

## Appendix A: Details of the APEX observations

### Appendix A.1: The spectral setups

The spectral setups used in the APEX observations are listed in Table A.1.

### Appendix A.2: Spectral variability in the APEX data

*Spectral* variability of stellar sources at submillimeter wavelengths has been rarely reported in the literature. It has been convincingly shown for O-rich Mira variables, including *o* Ceti, but only for maser species such as SiO (e.g. Gray et al. 1999) and OH (Gerard & Bourgois 1993) and no convincing evidence has been presented so far for other molecules. This is partially so, because investigation of variability, especially at submm wavelengths, is challenging for technical reasons. In particular, apparent intensity changes can often be explained by imperfect focus, pointing, and flux calibrations, uncertainties of which are usually difficult to assess quantitatively. Our APEX observations do not have those usual shortcomings. All the observations presented here were obtained after applying focus calibration which was performed on *o* Ceti using its bright CO emission. Similarly, pointing was calibrated on the Mira's CO lines and it did not show deviations from the source position greater than 2'' (usually much less), which is insignificant compared to the telescope beam of 18'' or 27'' at our frequencies. Overall, the pointing model and tracking performance at APEX was excellent in the years covered by our observations. We are confident these basic calibrations do not affect the derived intensity of the spectral features.

The flux calibration can be tested directly in our observations. It can be safely assumed that the rotational transitions of CO at  $v=0$ ,  $J=2-1$  and  $3-2$ , covered in two different epochs do not vary on the time scales of years (Cernicharo et al. 2014). Taking the large size of the envelope producing these lines of  $r \sim 10^{16}$  cm and the corresponding wind crossing time of the order of  $10^5$  yr, any short-scale change in Mira's wind, e.g. due to a potentially variable mass-loss rate, cannot effectively influence the total flux of those lines. Additionally, the lines arise in gas that is collisionally excited and none of the main gas heating terms can be significantly affected by stellar light variability for these low- $J$  lines. We can therefore use them as a benchmark for relative-intensity calibration of the instrument at different dates.

The band centered at 229.8 GHz was observed in 2013 and 2015 using exactly the same configuration. The same sensitivity levels were reached. This band covers the CO(2-1) line which was observed at a signal-to-noise ratio (S/N) of 4700 (line peak to rms noise level). The line profiles are identical in both spectra and the line flux is consistent to within 1.12% on both dates. Other lines covered in the spectrum were the CO(2-1) line at  $v=1$  and AIO  $N=6 \rightarrow 5$ . The two lines were not detected in 2013 but are definitely present in 2015. On the basis the excellent consistency in the observations of the CO(2-1) line, the change in the appearance of the CO  $v=1$  and AIO features in 2015 must be due to the intrinsic source variability in those lines, where both are expected to arise in the innermost envelope.

The band centered at 344.454 GHz was observed in the USB in August 2013 and in the LSB in July 2014. The strongest line covered by these spectra, CO(3-2), has a measured flux 1.07 times higher on the earlier date. Two other strong lines covered,  $^{29}\text{SiO}(8-7)$  and  $\text{SO}(8_8-7_7)$ , show very similar intensity ratios, i.e. consistent to within 1% with what was measured for the CO(3-2) line. The effect is therefore systematic and we cor-

rected the later spectrum by the calculated factor. (The most likely source of this slight inconsistency is an error in the sideband rejection factors of FLASH+, as the sideband was the only different aspect in the instrumental configuration. A few % uncertainty in the sideband ratio is well within the performance specifications of FLASH+.) In the corrected spectra, the flux of the maser emission of the SiO(8-7)  $v=1$  line decreases by a factor of 2.1 from 2013 to 2014. This decrease is physical (cf. Gray et al. 1999). For other weaker lines covered, including the species of our interest, CO(3-2) at  $v=1$  and AIO  $N=9 \rightarrow 8$ , the fluxes are consistent with the rms noise levels on the two dates. We therefore combined the data to increase the S/N for these weak lines.

## Appendix B: Processing of the interferometric data for the AIO 6 $\rightarrow$ 5 line

While processing the ALMA data for the AIO 6 $\rightarrow$ 5 transition, we encountered a similar problem with the CLEAN procedure as that described in detail in Wong et al. (2016) (their Appendix B). That is, we found significant differences in the depth and shape of absorption features when processed in CLEAN with continuum and after continuum subtraction. This data-processing problem is closely related to the relative distribution of the emission and absorption regions and their relative strengths. In our work, we present only the data processed in CLEAN after continuum subtraction which have a better S/N and all absorption features are *deeper* than in the data processed with the alternative method. The emission regions one beam size away and farther from the strongest absorption feature appear exactly the same after applying each of the processing schemes. Unlike in Wong et al. (2016), where data of much higher S/N are analyzed and the processing procedure does not influence the data interpretation, we do not analyze in detail the region within  $2R_*$  because the two processing schemes may lead to different interpretations.

## Appendix C: Optical spectra of Mira

**Table A.1.** Log of APEX observations of Mira.

Frequency setup	Central frequency (MHz)	Noise rms per 3.8 MHz ( $T_A^*$ mK)	Integr. time ON (min)	Observation dates
HET230				
TiO-222L	222700.000	1.3	203.4	03,17,18,19,20-12-2013
vCO21-AlO	229800.000	1.3	186.9	06,15,16,18,23-10-2013
vCO21-AlO	229800.000	1.2	213.9	09,10,11,12-06-2015
FLASH+				
AlO306_OSB	294698.830	1.4	99.2	07,08-07-2014
AlO306	306700.000	1.4	99.2	07,08-07-2014
AlO344_OSB	332452.819	1.9	78.9	13,14-08-2013
AlO344	344454.000	1.8	80.4	13,14-08-2013
AlO344TiO	344454.000	1.7	84.8	30-06-2014; 01,02,06-07-2014
AlO344TiO_OSB	356455.219	2.0	84.8	30-06-2014; 01,02,06-07-2014
AlO420_OSB	408898.804	4.2	51.7	13,14-08-2013
AlO420	420900.000	10.5	51.7	13,14-08-2013
AlOvCO458	458020.000	5.1	27.3	14-08-2013
AlOvCO458_OSB	470021.181	6.2	27.3	14-08-2013
AlO497_OSB	485398.793	24.0	168.7	01,02,06,07,08-07-2014
AlO497	497400.000	4.3	168.7	01,02,06,07,08-07-2014

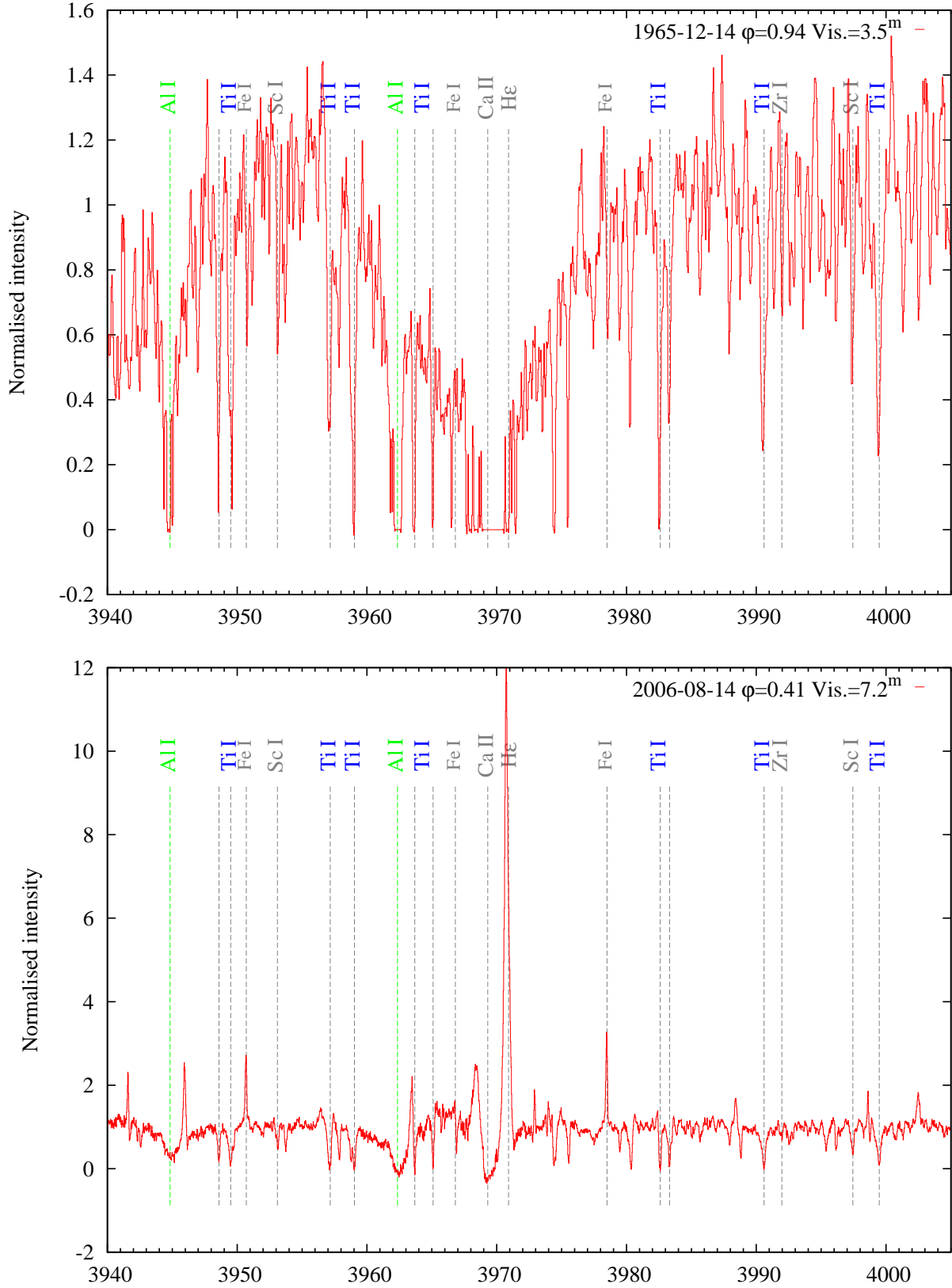


**Fig. C.1.** High-resolution optical spectra of Mira covering the resonance lines of Al I and Ti I. The date of observations and the corresponding phase and visual magnitude are specified in the upper right corner of each panel. All spectra were normalized with high-order polynomials. The pseudo-continuum in this spectral region is dominated by broad wings of the Ca II doublet and the normalization partially removed its absorption. The normalization was optimised to better illustrate the shape of the Al I lines and to limit the scale of the figure. The imperfect normalization affects the apparent intensity ratio of the two lines of Al I. Some spectra were smoothed. Identification labels are shown for selected features at their approximate locations.

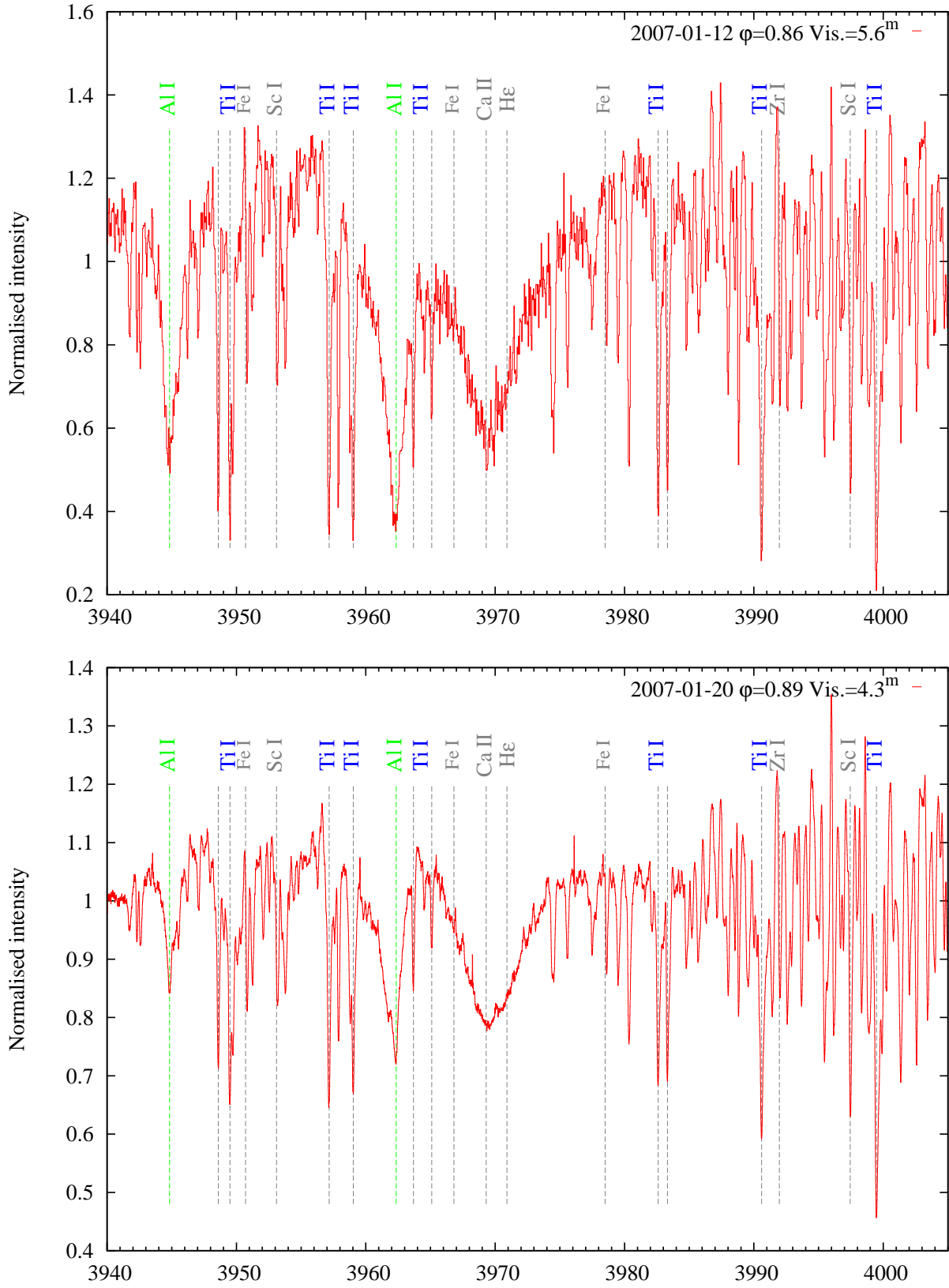


Fig. C.1. Continued.

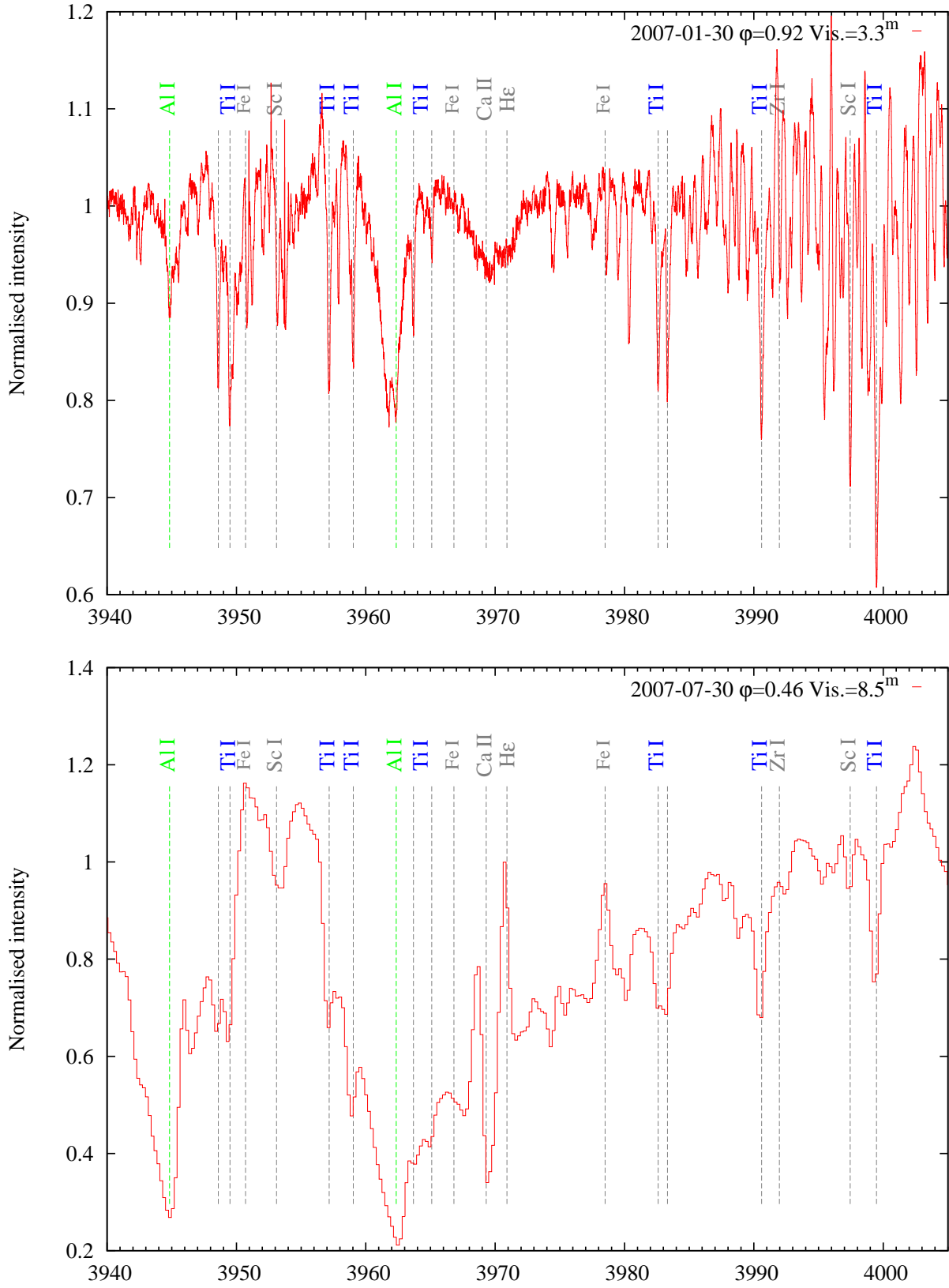


Fig. C.1. Continued.



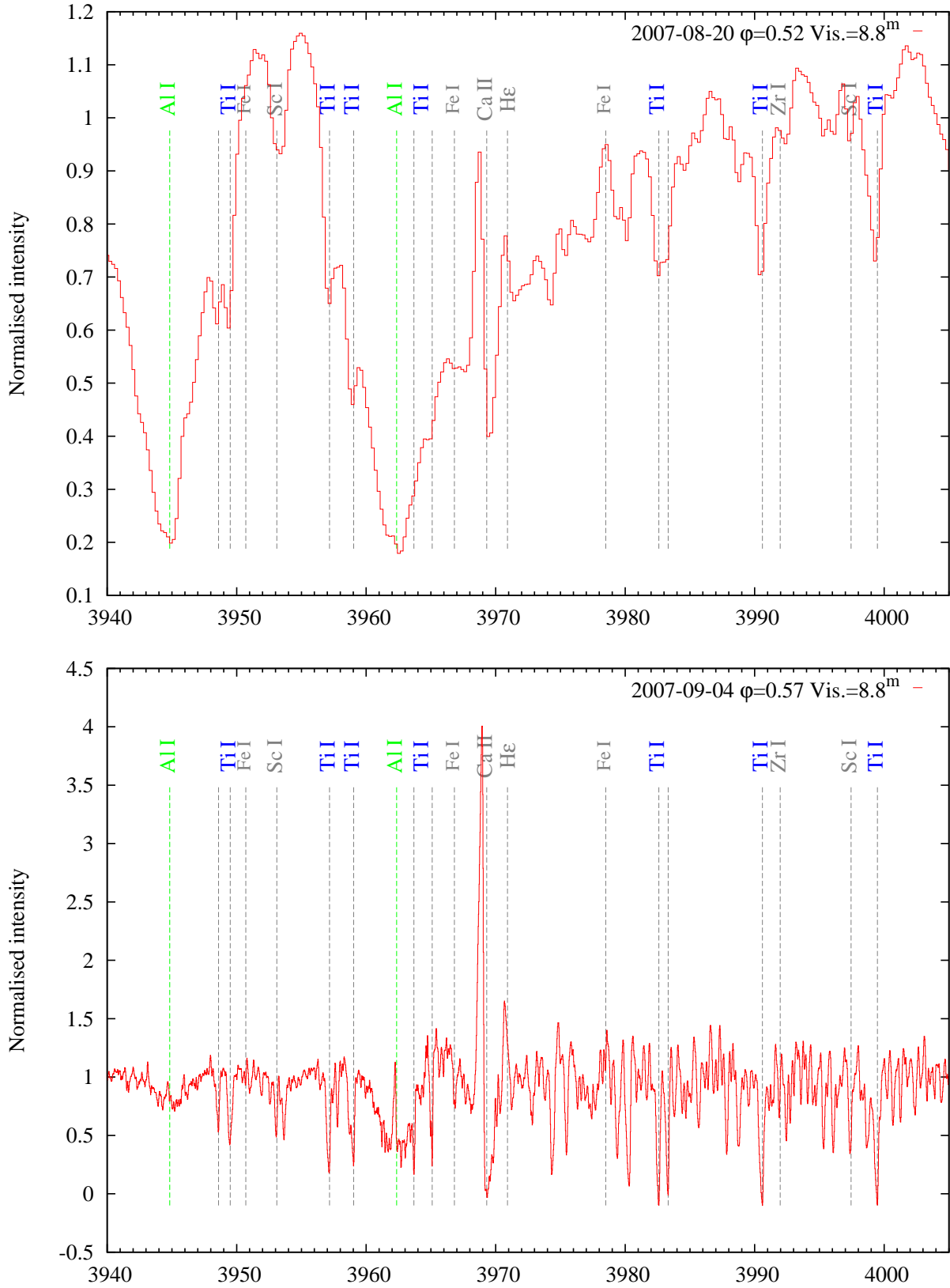


Fig. C.1. Continued.

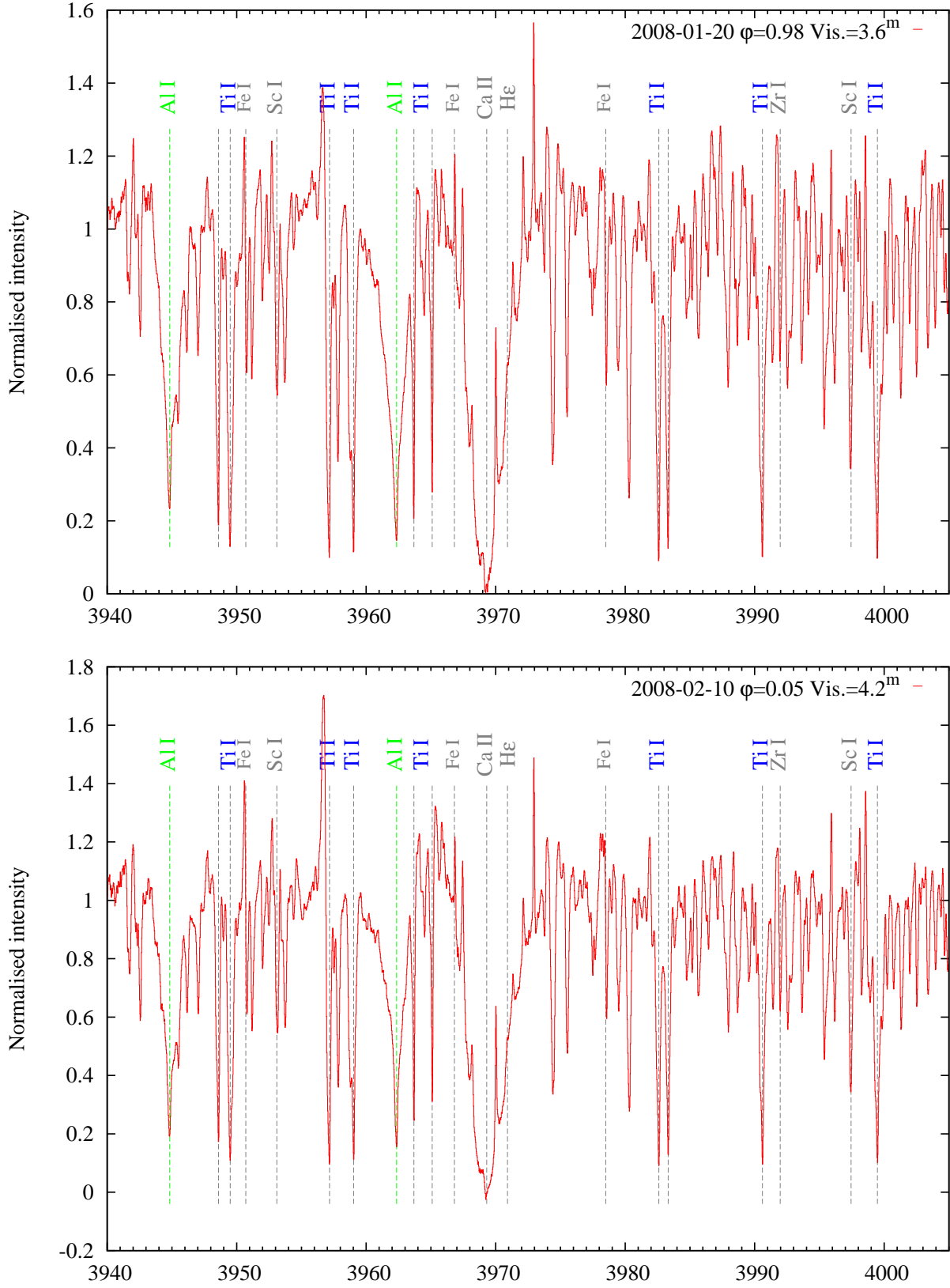


Fig. C.1. Continued.

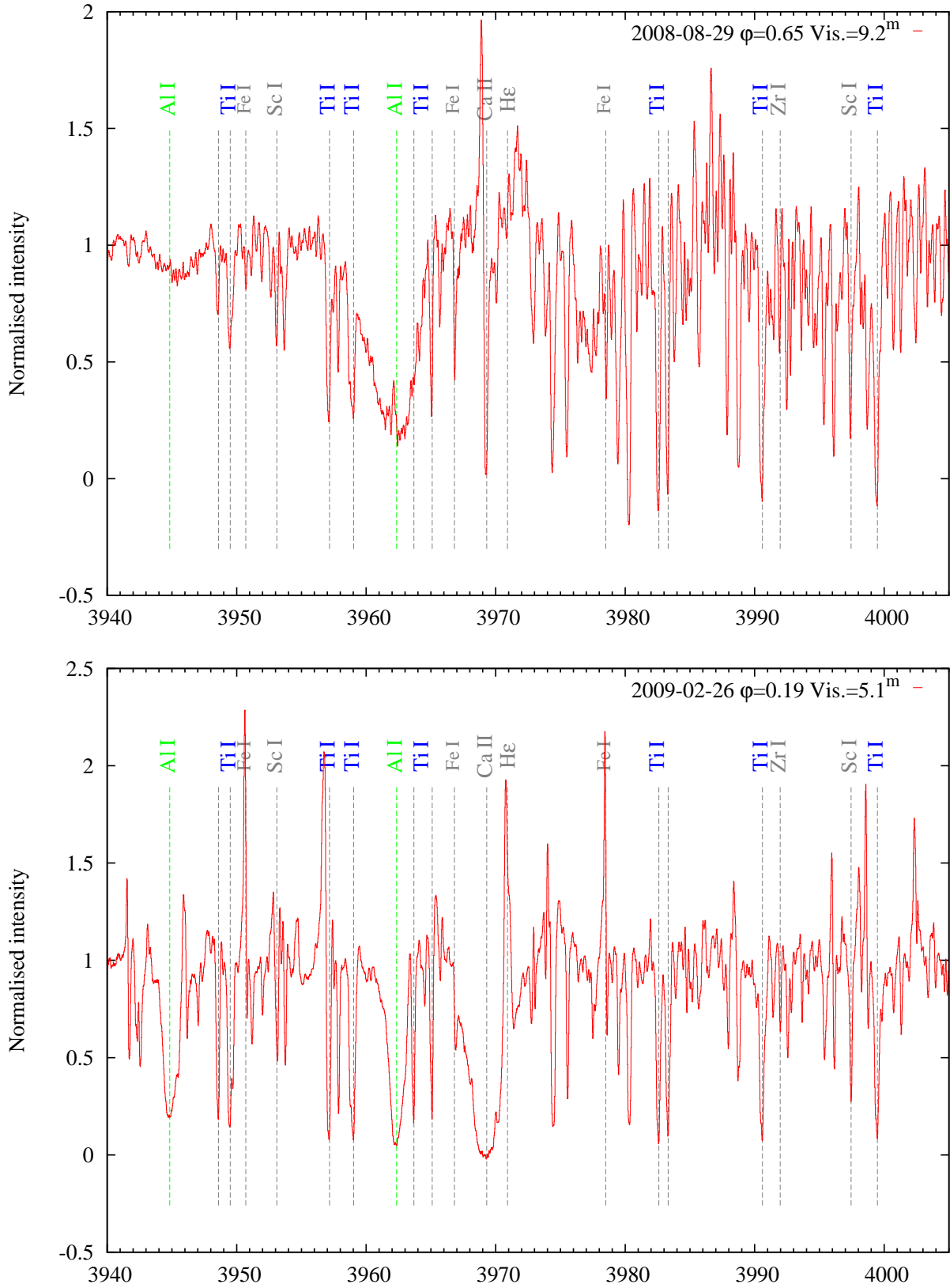
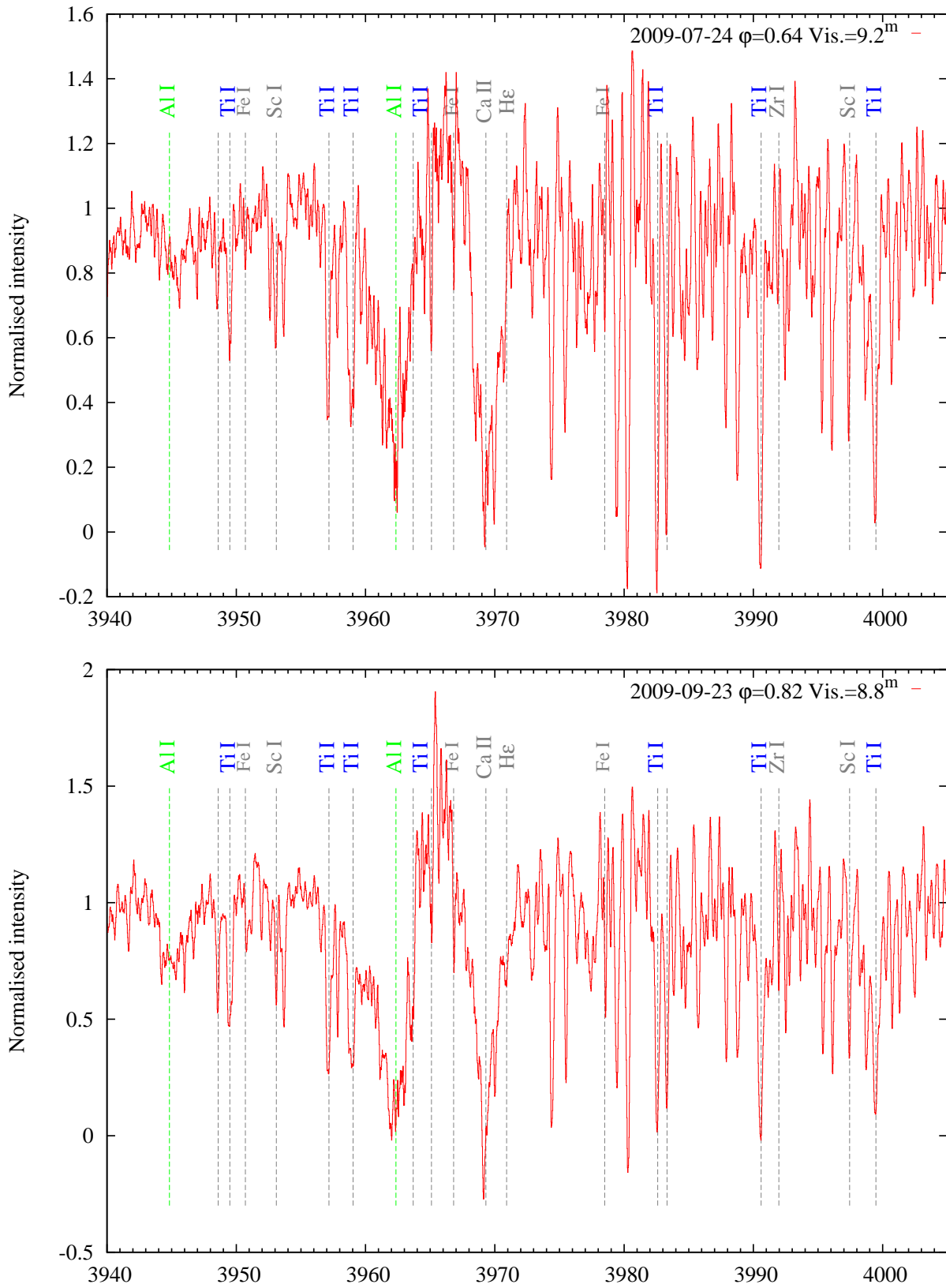


Fig. C.1. Continued.



**Fig. C.1. Continued.**

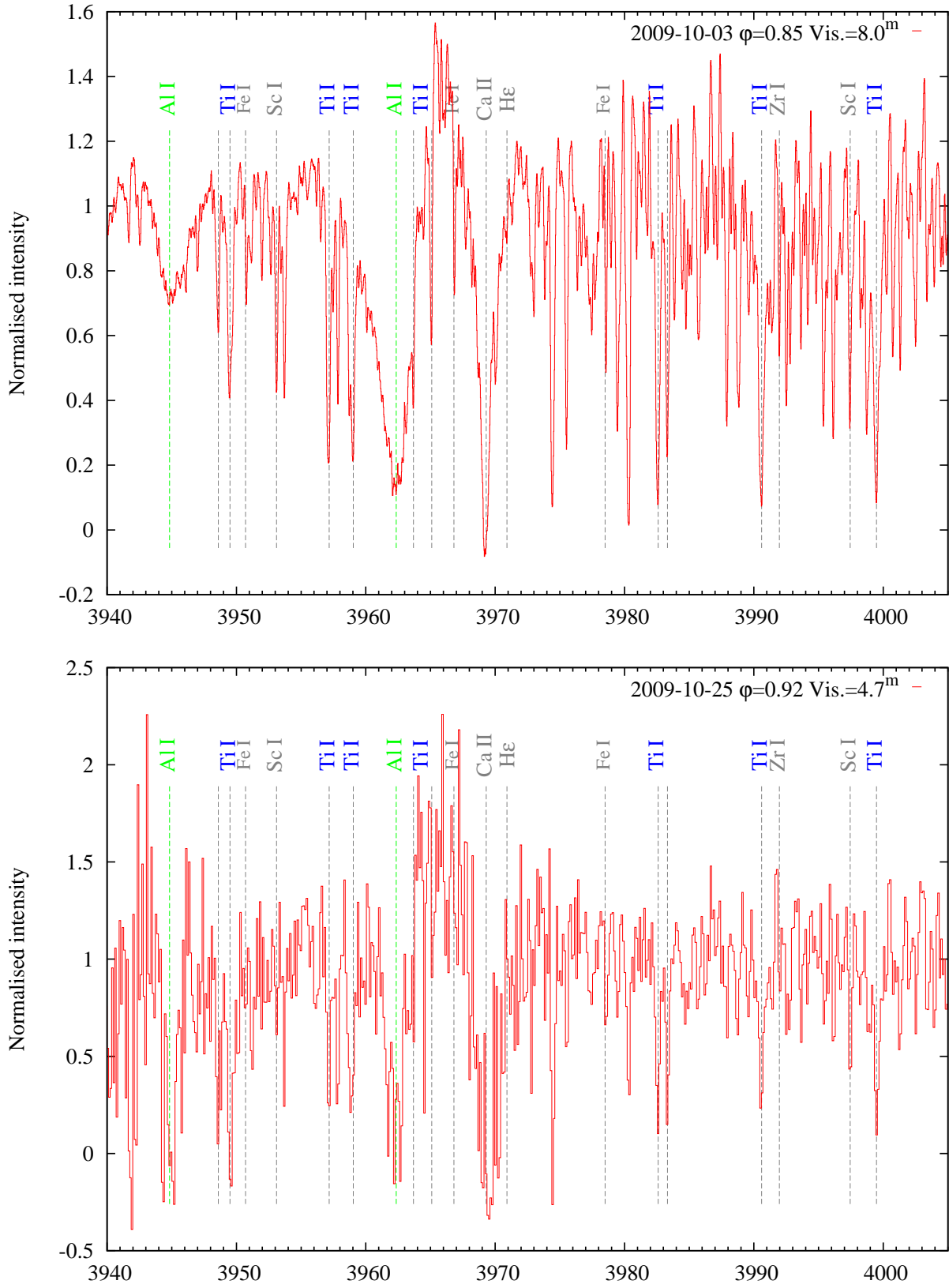


Fig. C.1. Continued.

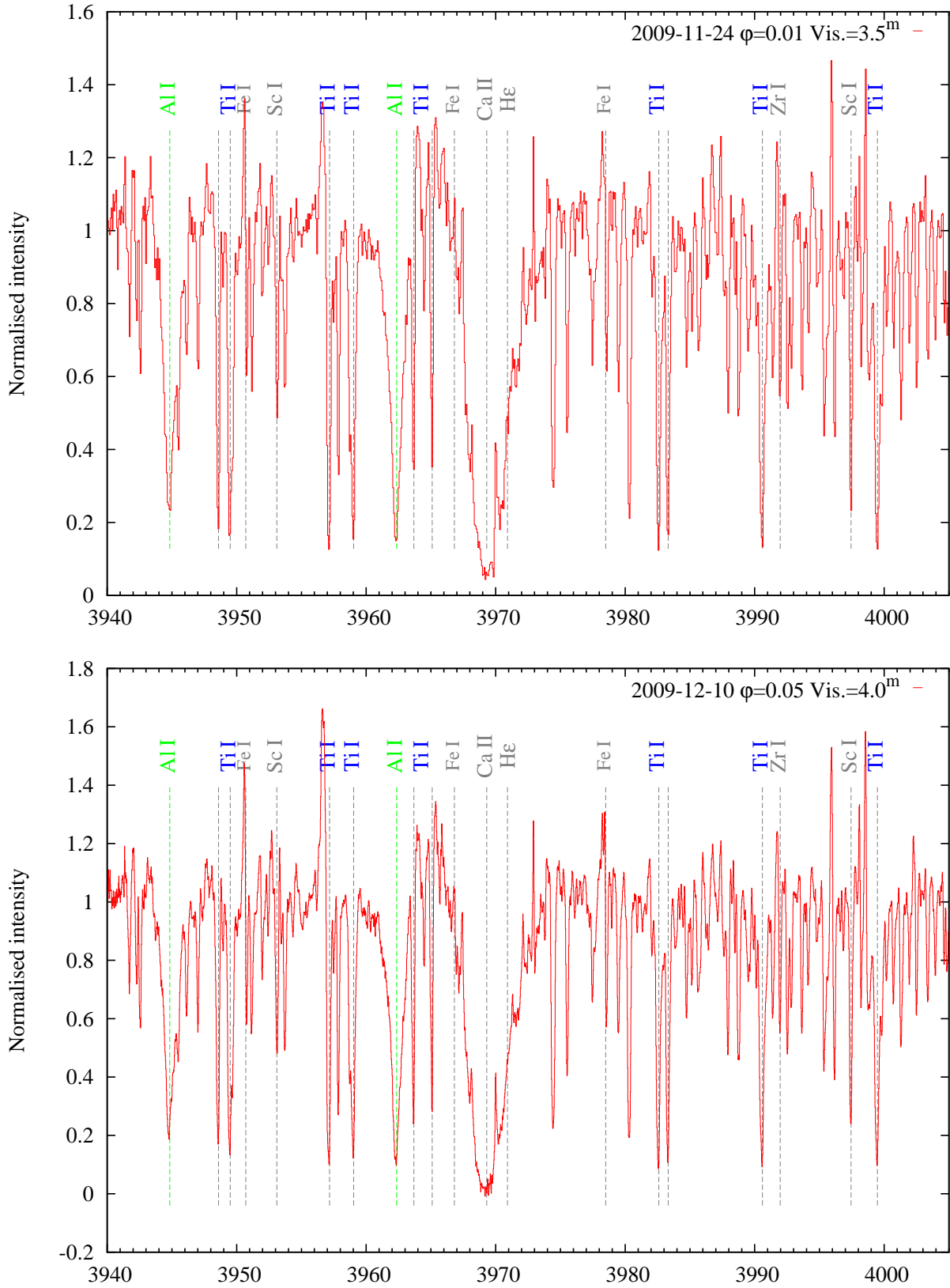


Fig. C.1. Continued.



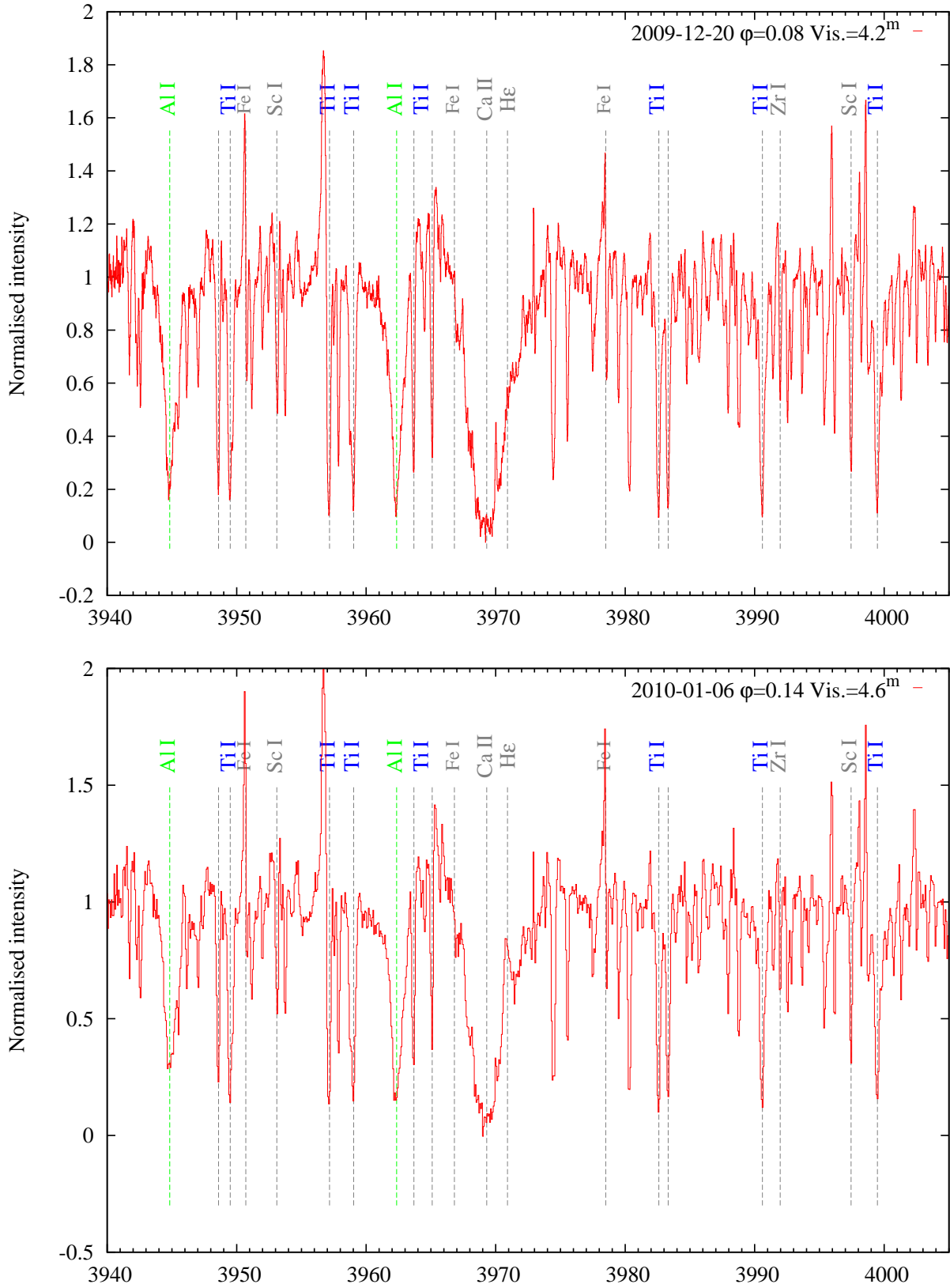


Fig. C.1. Continued.

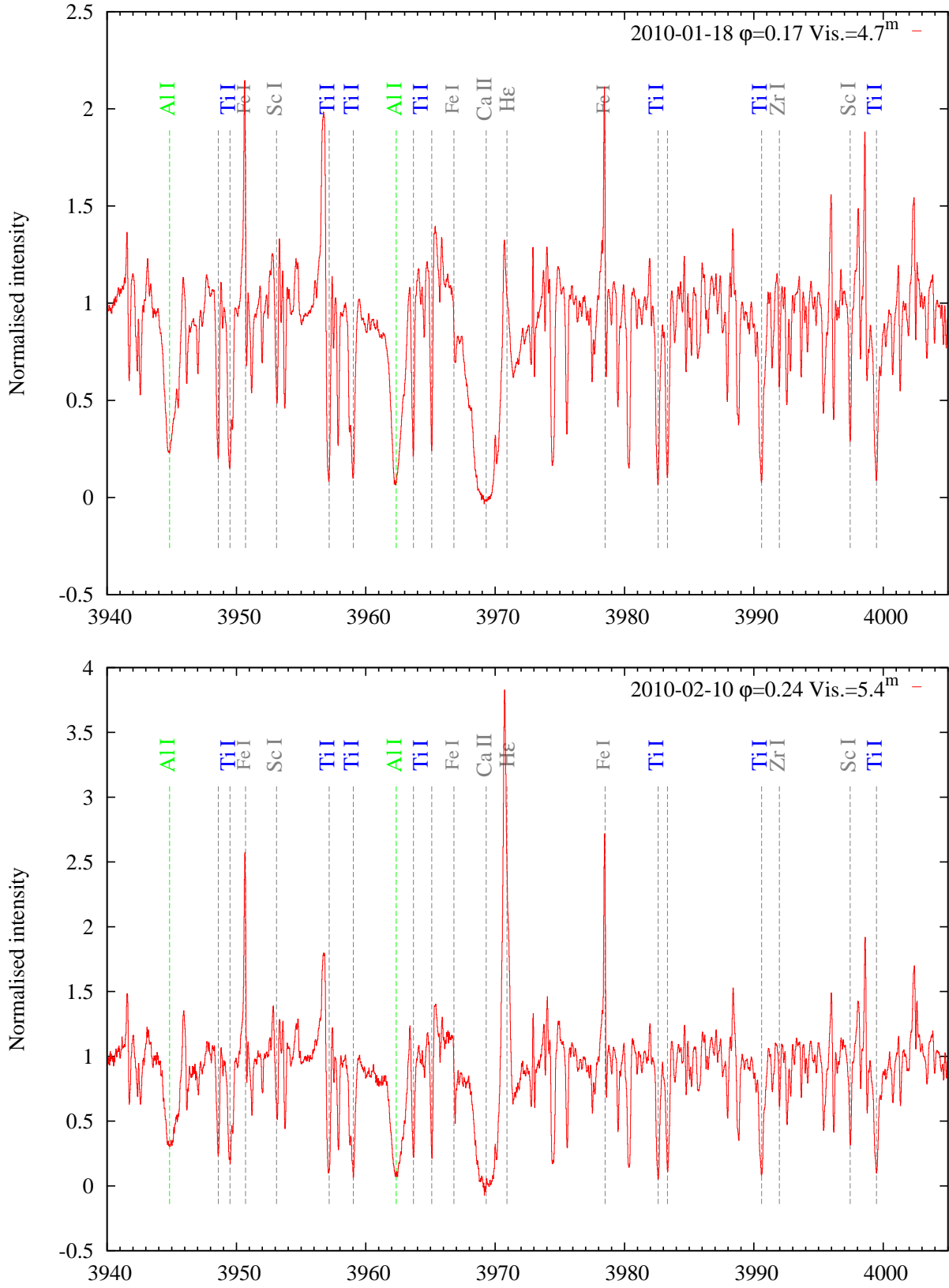


Fig. C.1. Continued.

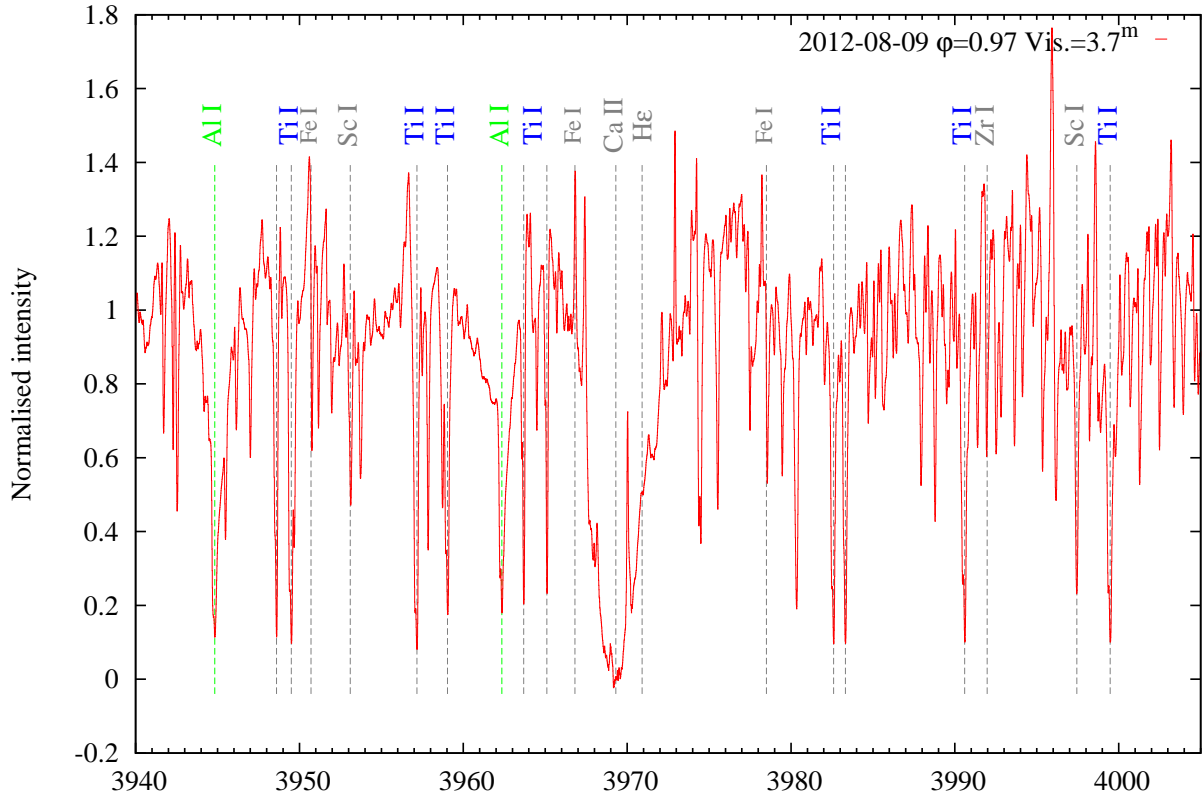
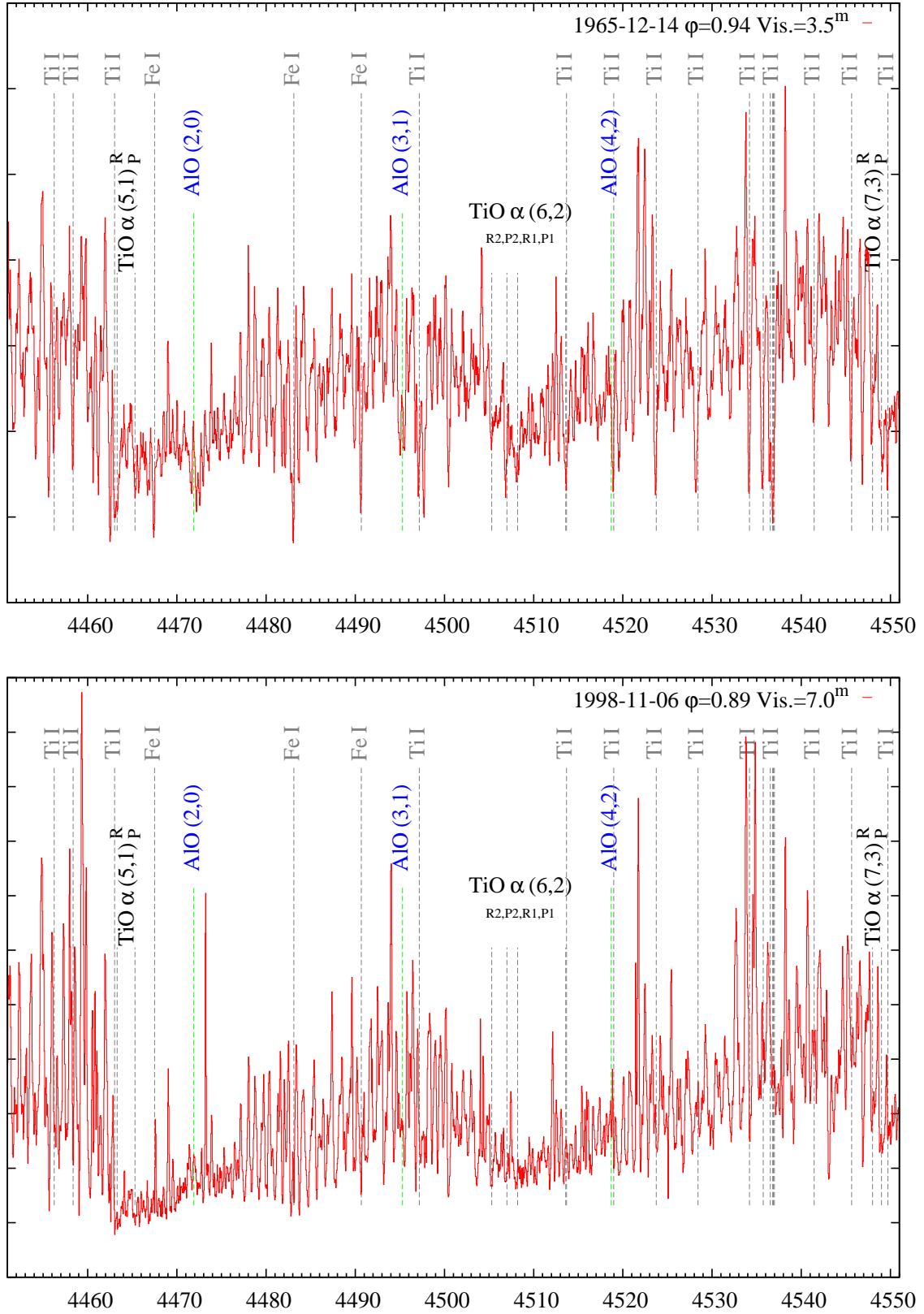


Fig. C.1. Continued.



**Fig. C.2.** High-resolution optical spectra of Mira covering the  $\Delta v=+2$  sequence of the AIO  $B-X$  system. The AIO bands are marked with blue labels. Locations of the identification markings are only approximate. The date of observation and the corresponding phase and visual magnitude are specified in the upper right corner of each panel. Some spectra were smoothed. Spectra from Narval are affected by an imperfect combination of different echelle orders in the 4485–4495 Å range.

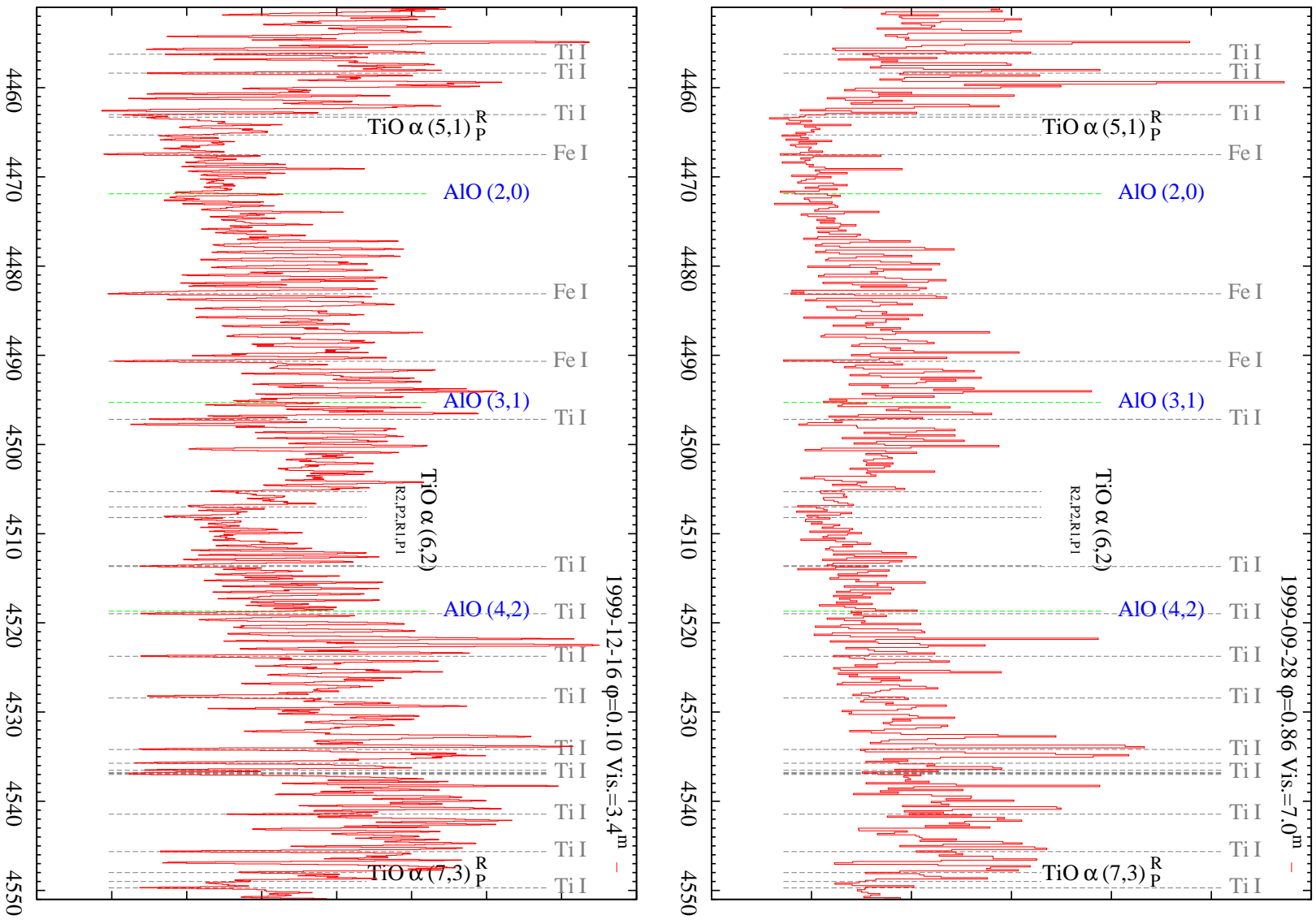


Fig. C.2. Continued.

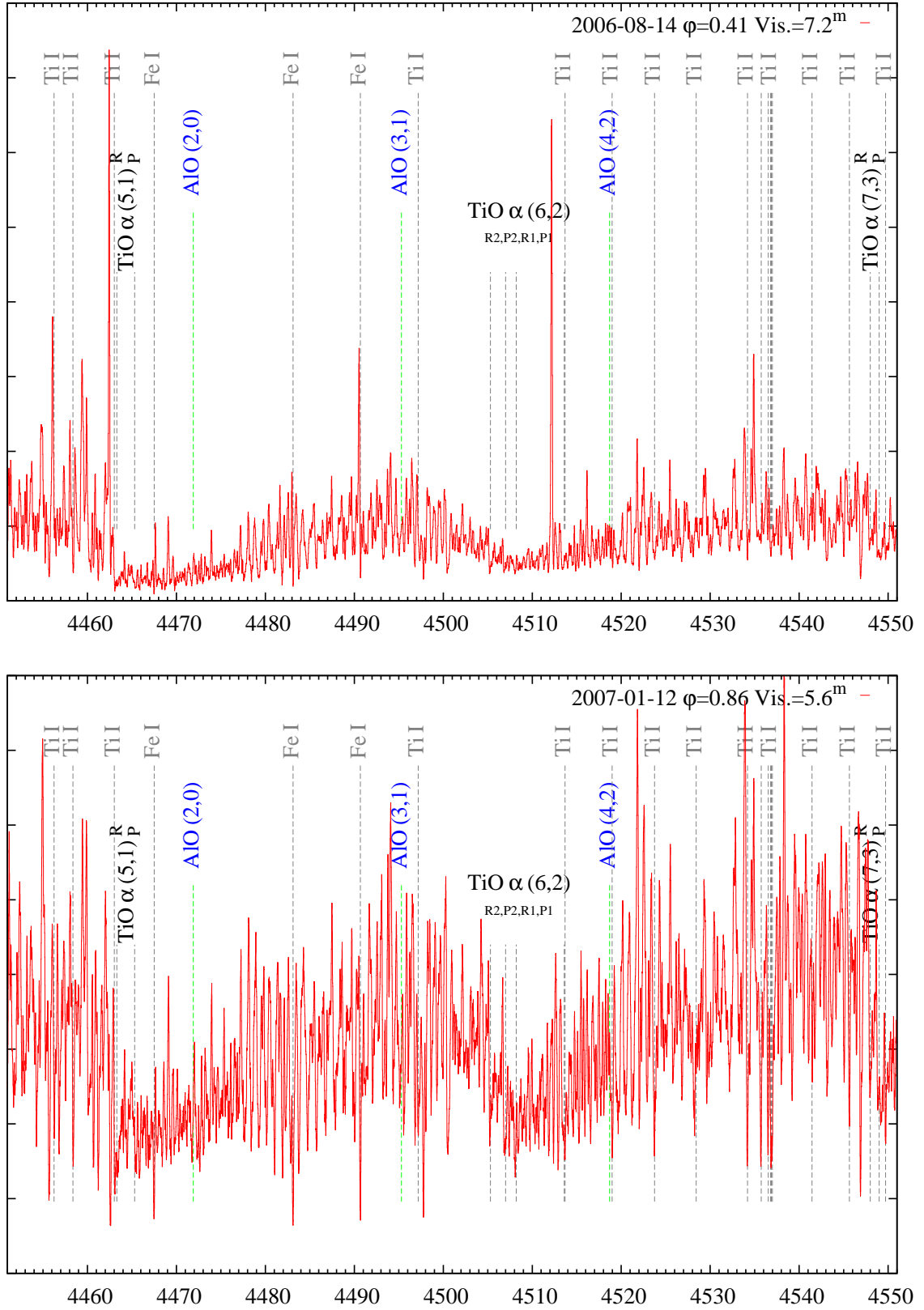


Fig. C.2. Continued.

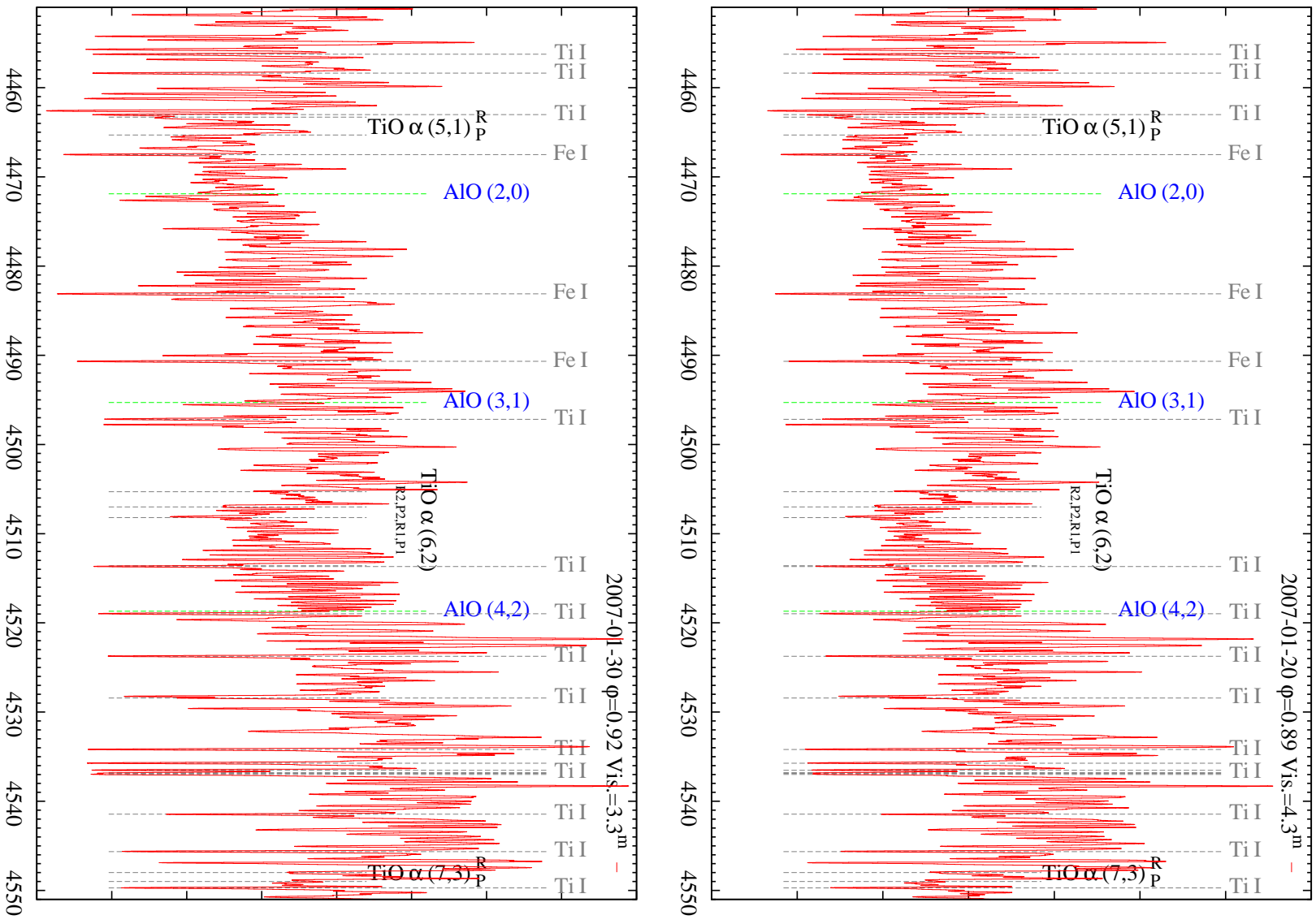


Fig. C.2. Continued.



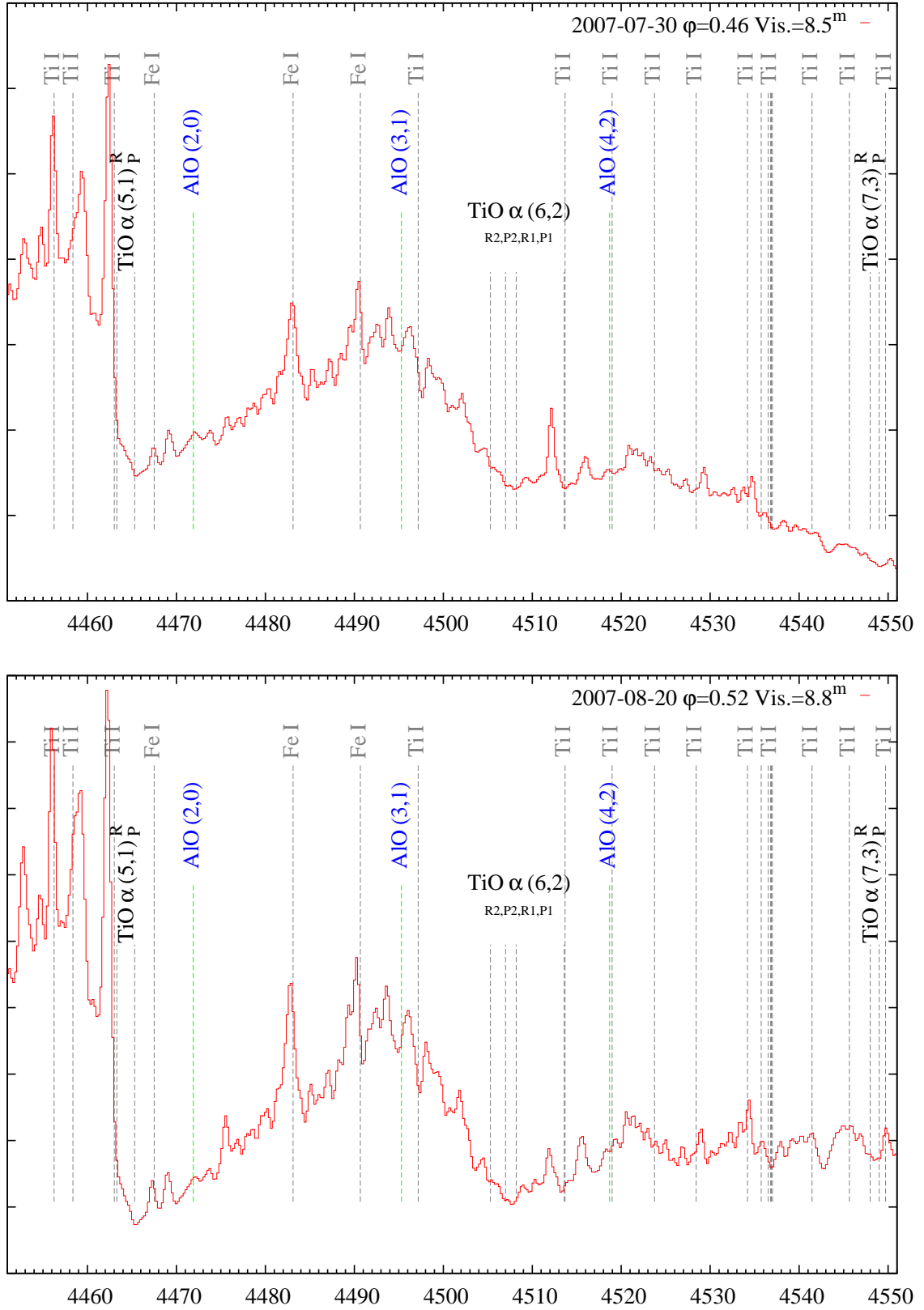


Fig. C.2. Continued.

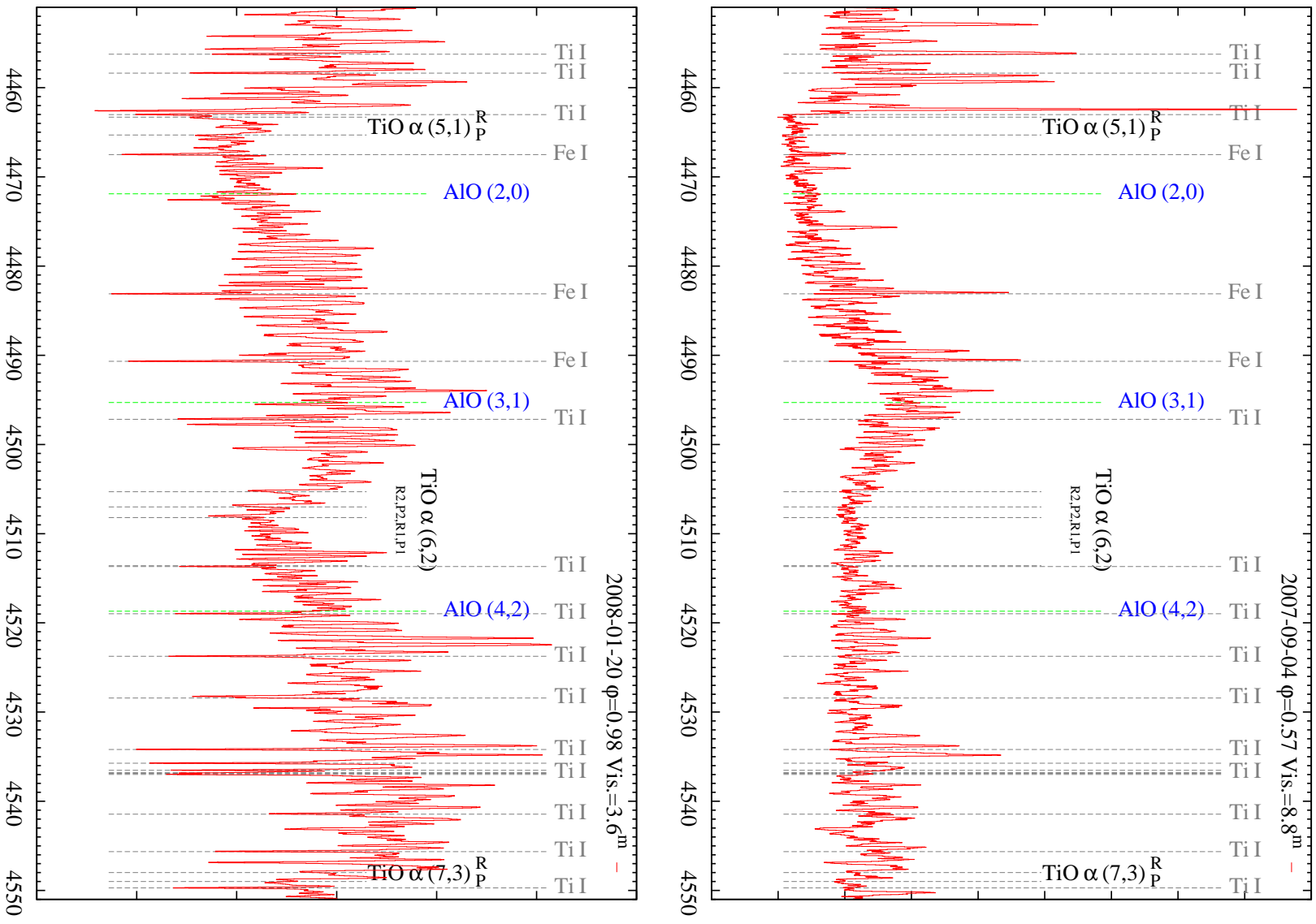


Fig. C.2. Continued.

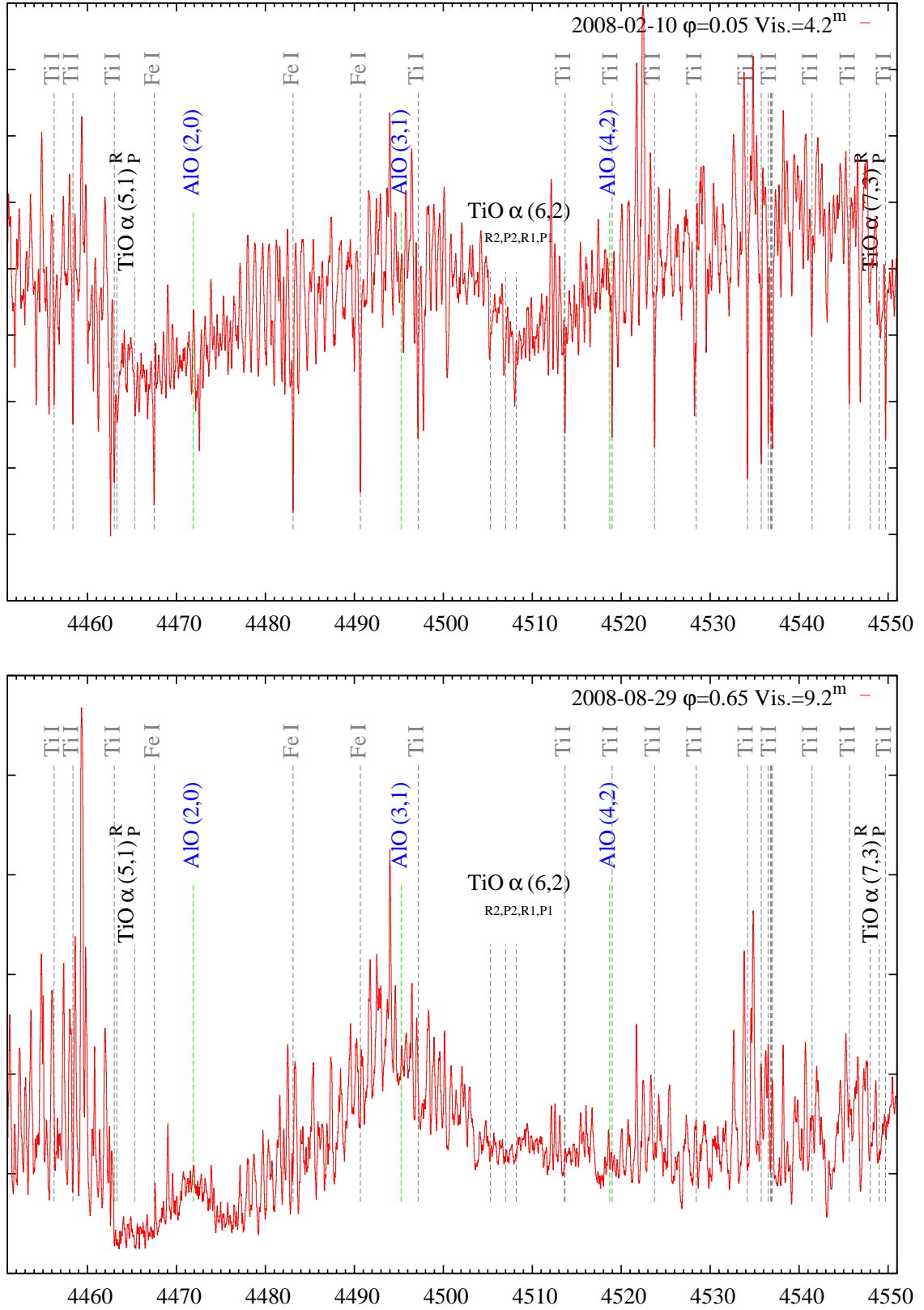


Fig. C.2. Continued.

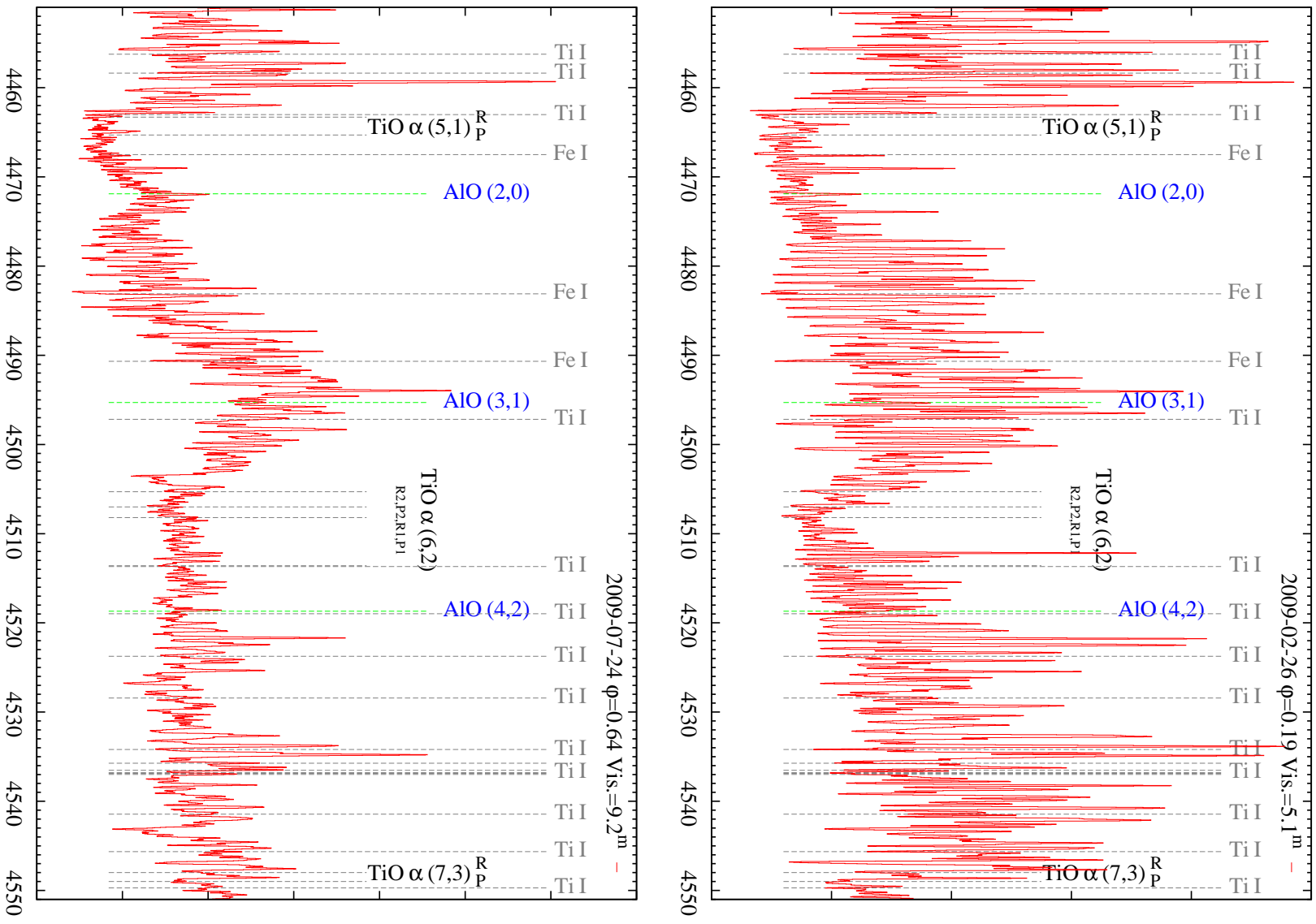


Fig. C.2. Continued.

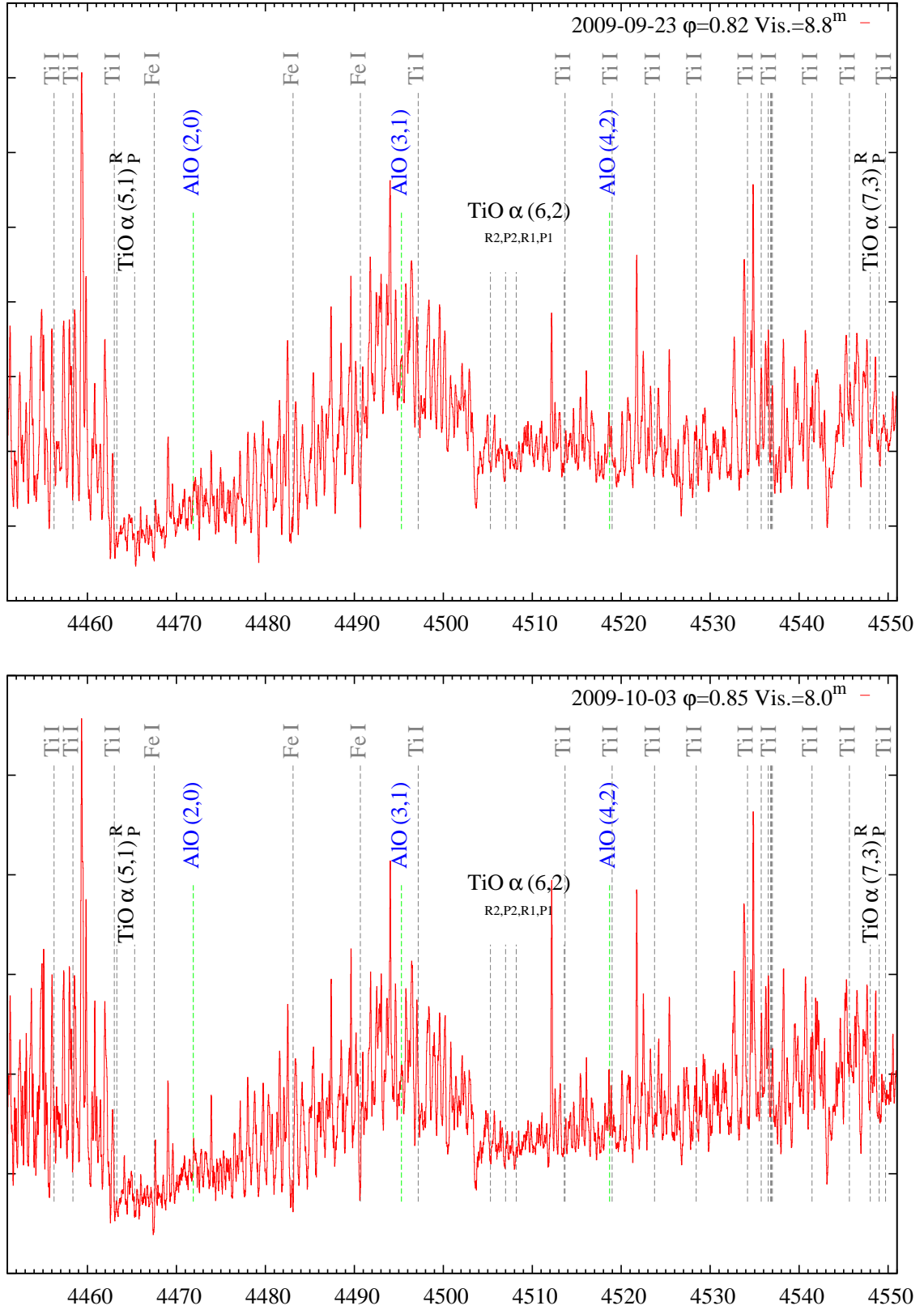


Fig. C.2. Continued.

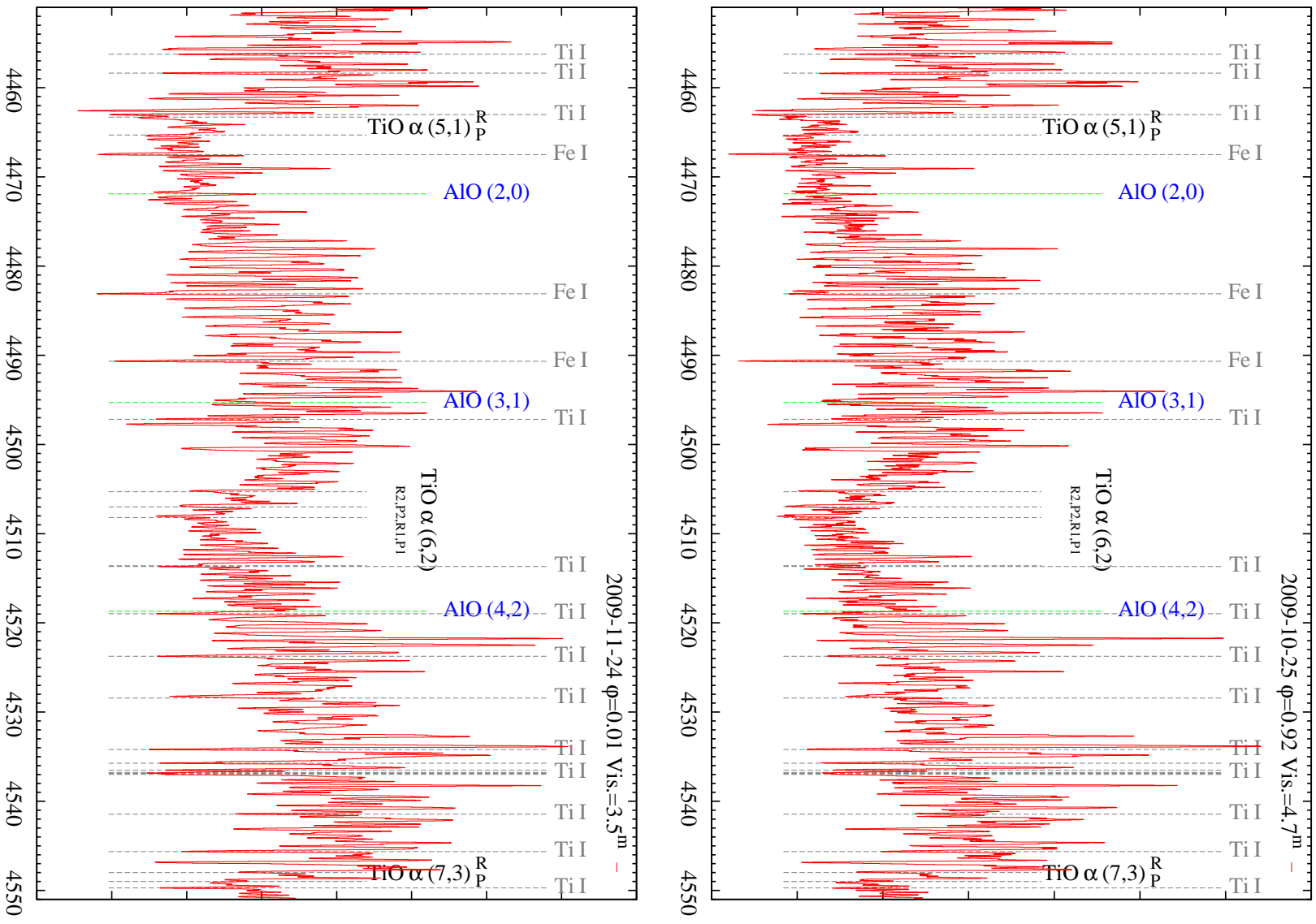


Fig. C.2. Continued.



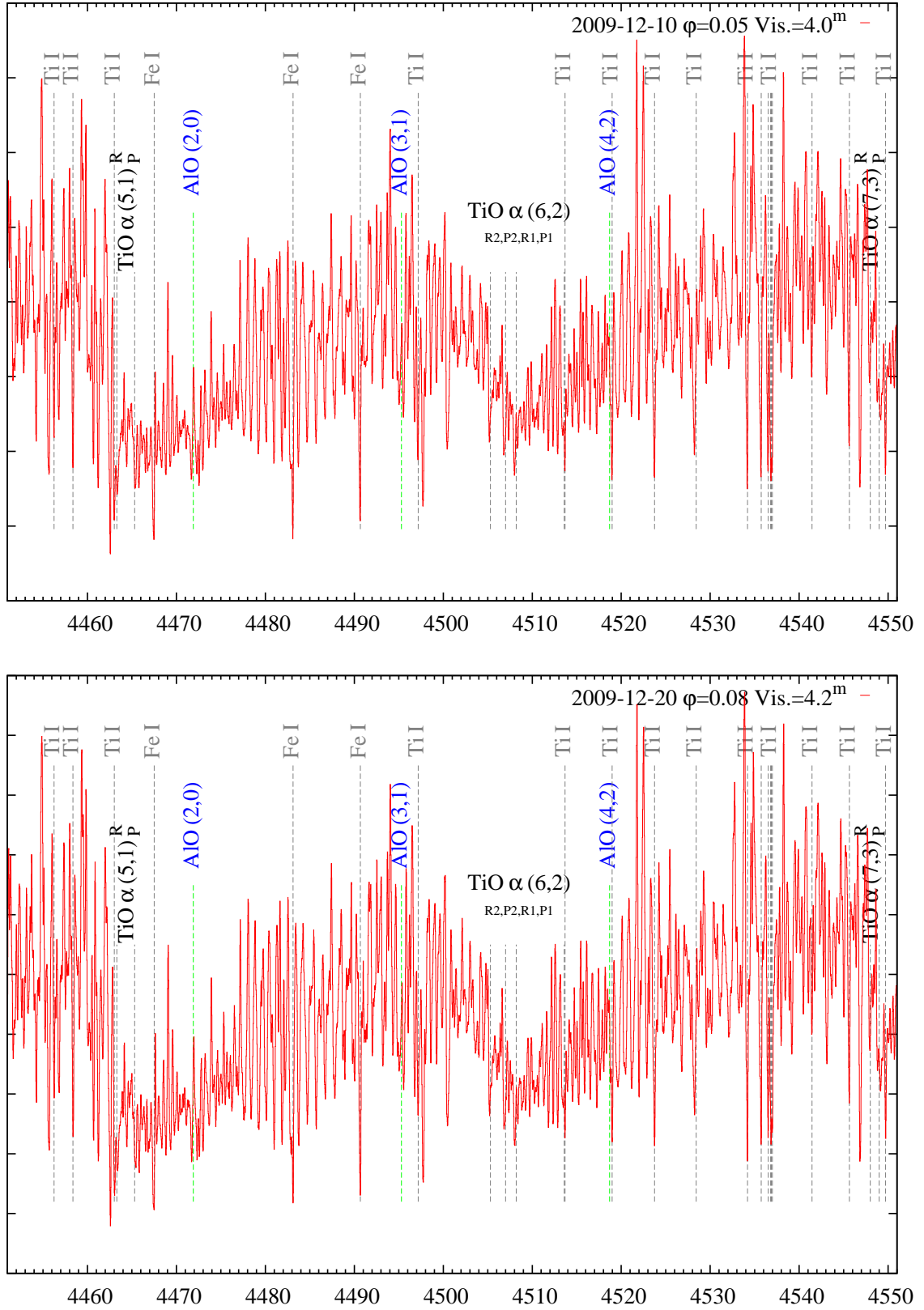


Fig. C.2. Continued.



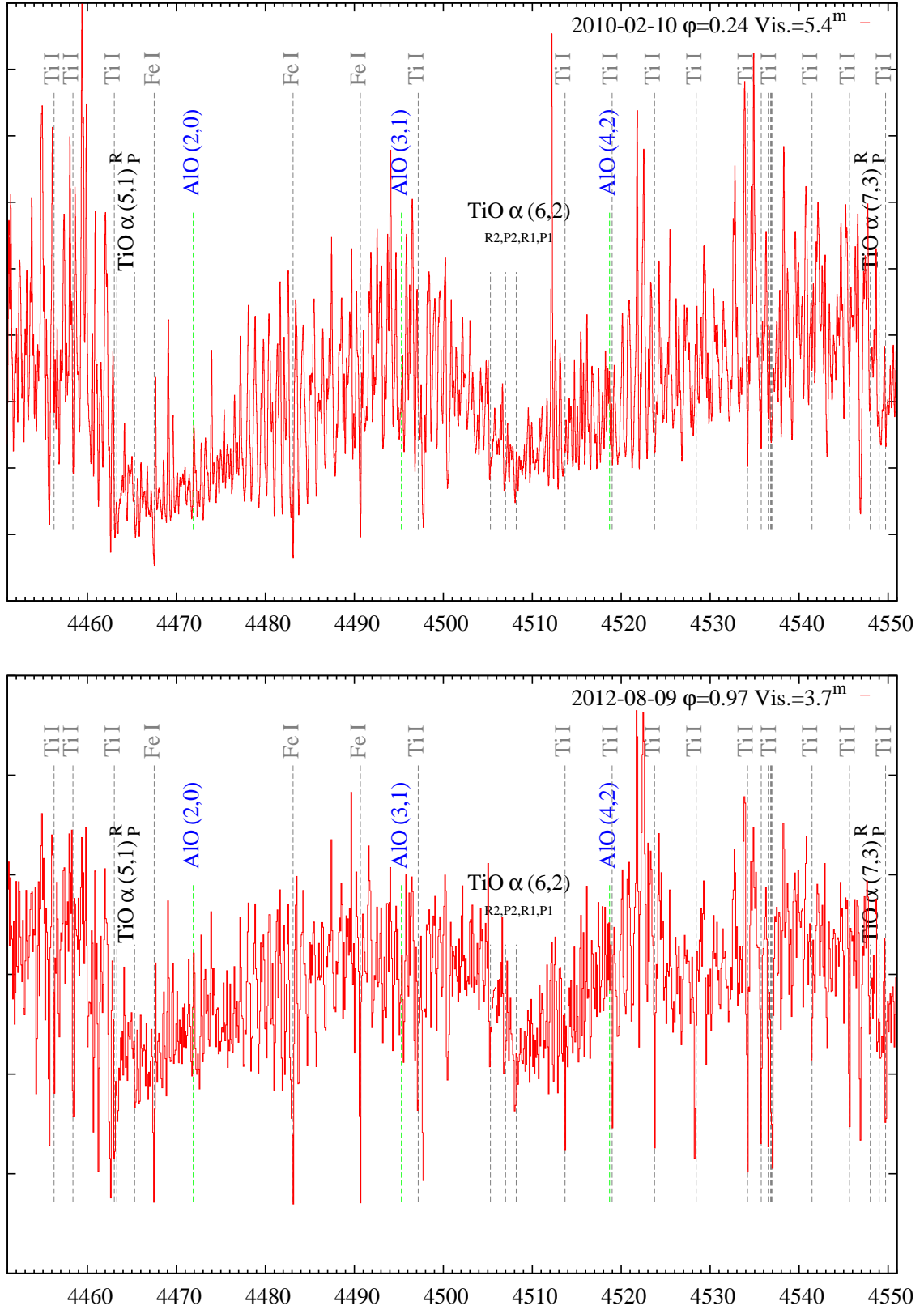
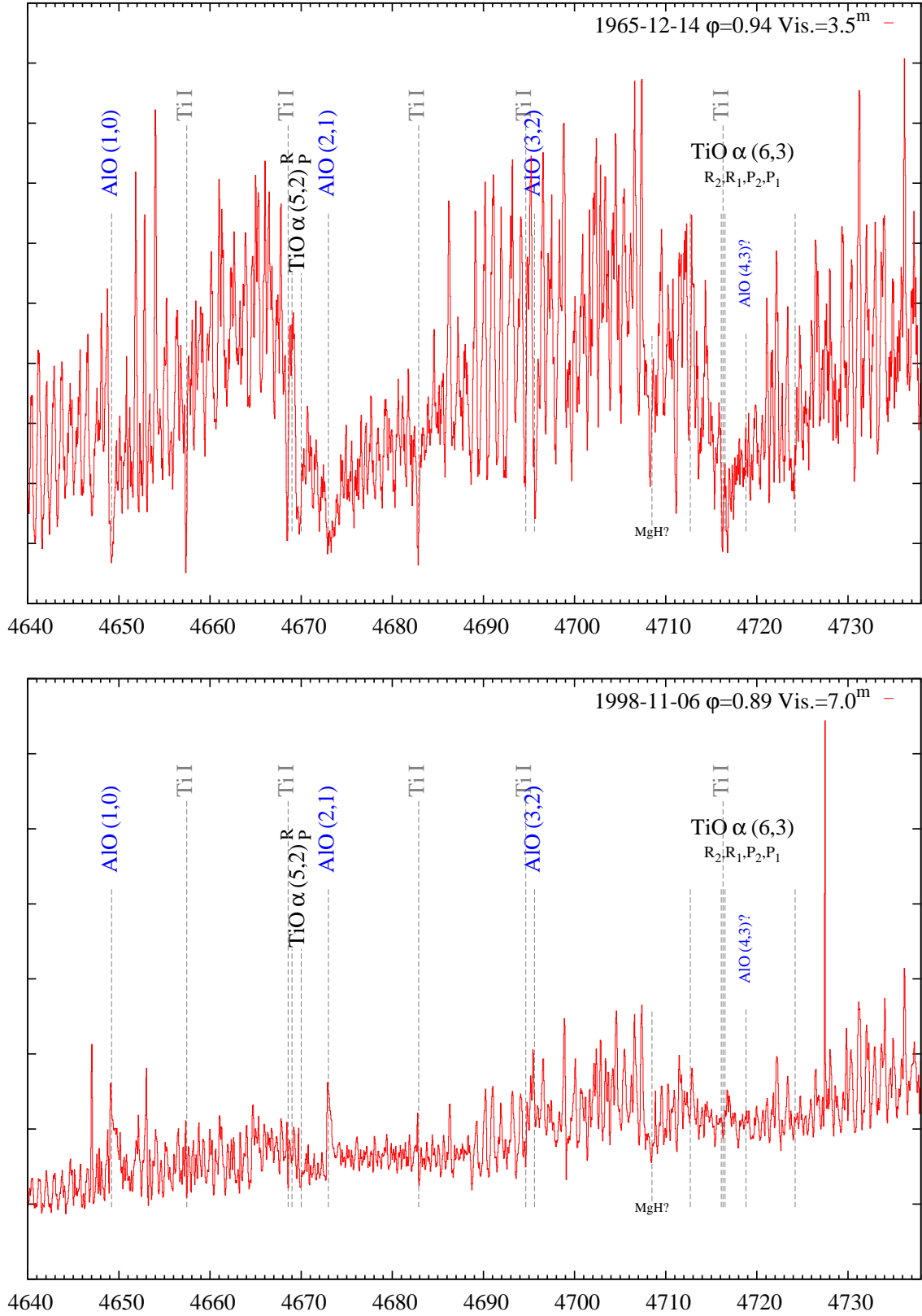


Fig. C.2. Continued.



**Fig. C.3.** The same as Fig. C.2 but for the  $\Delta\nu=+1$  sequence of AlO  $B-X$ . Spectra from Narval are affected by an imperfect combination of different echelle orders in the 4665–46755 Å range.

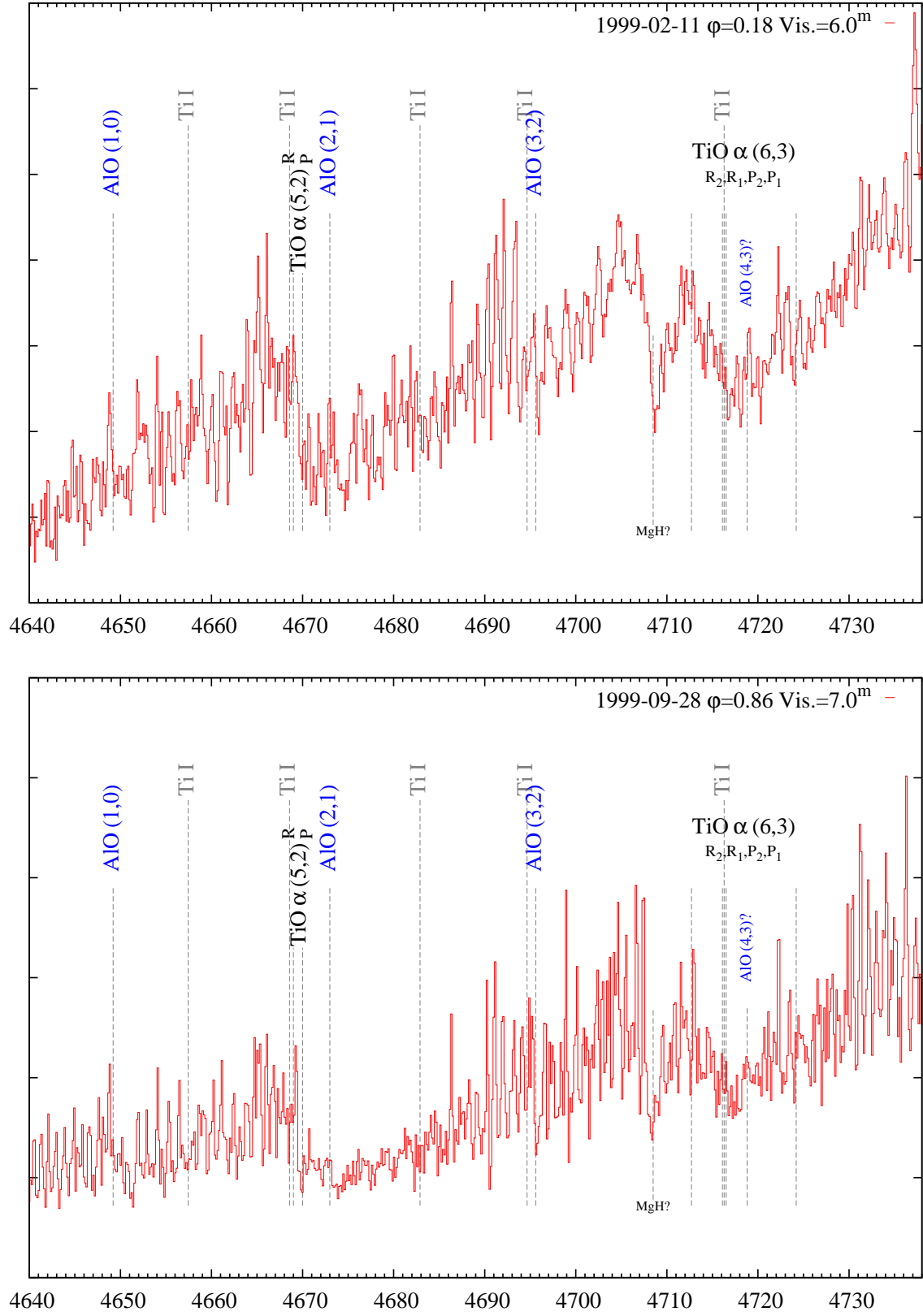


Fig. C.3. Continued.

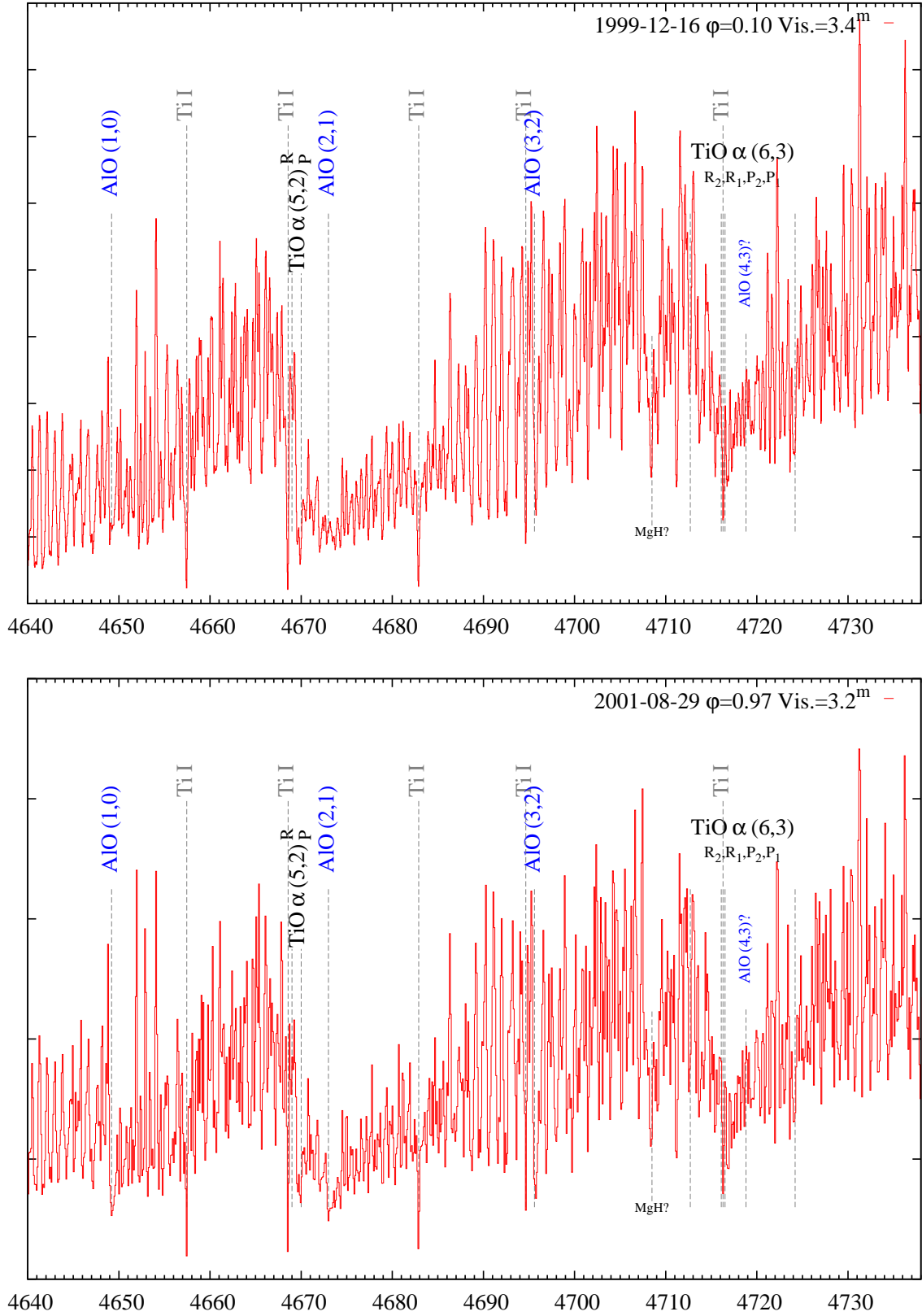


Fig. C.3. Continued.

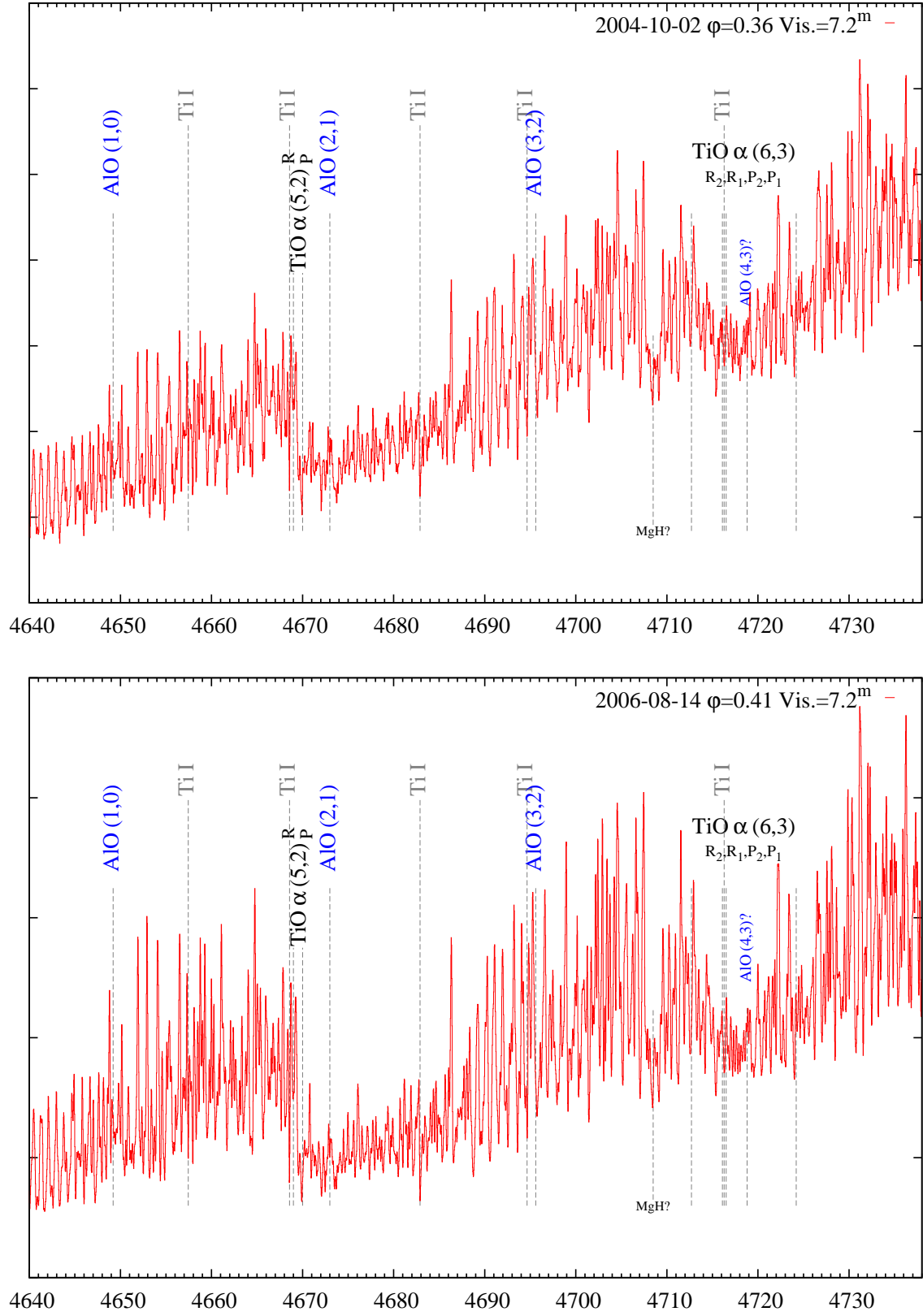


Fig. C.3. Continued.



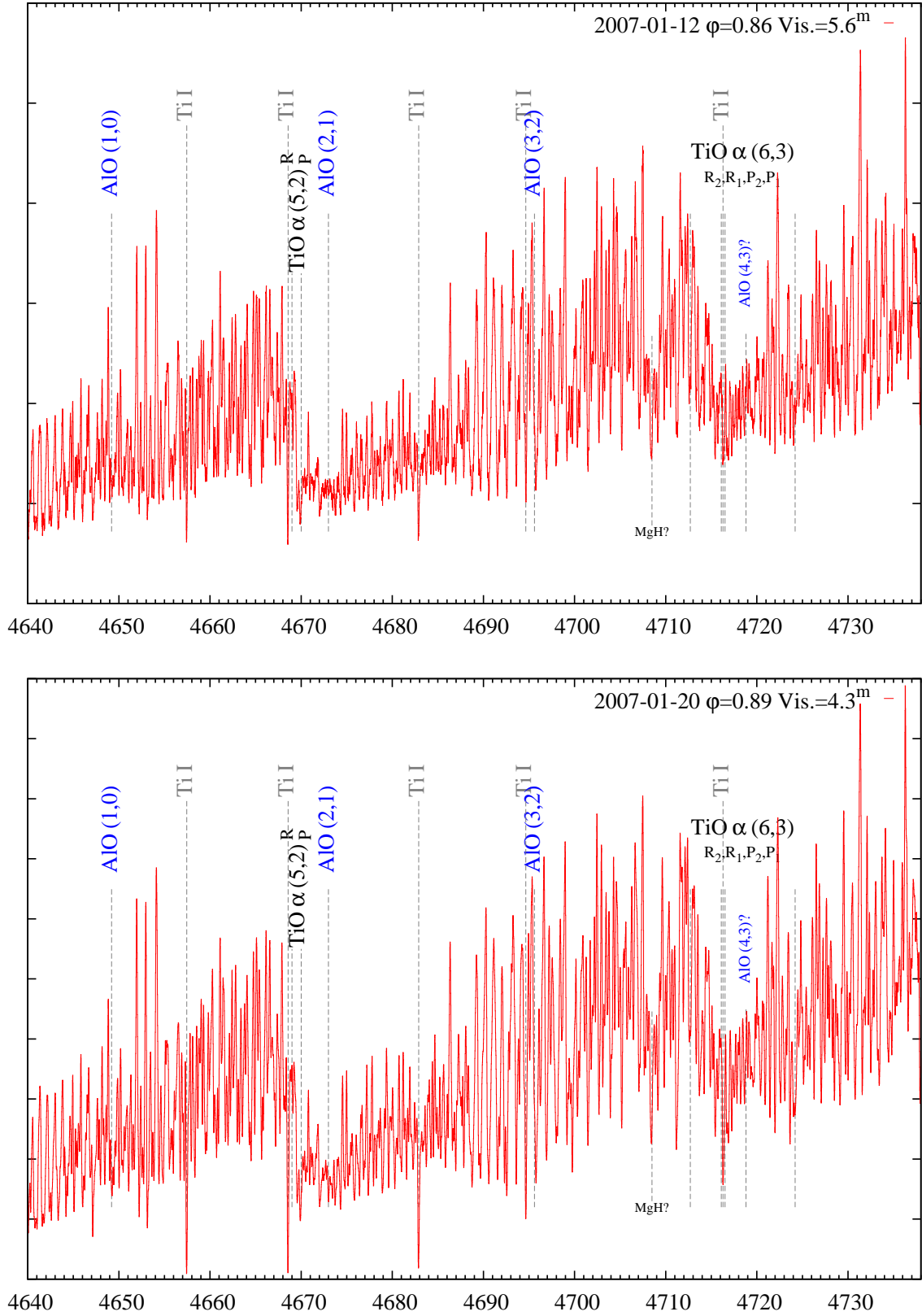


Fig. C.3. Continued.

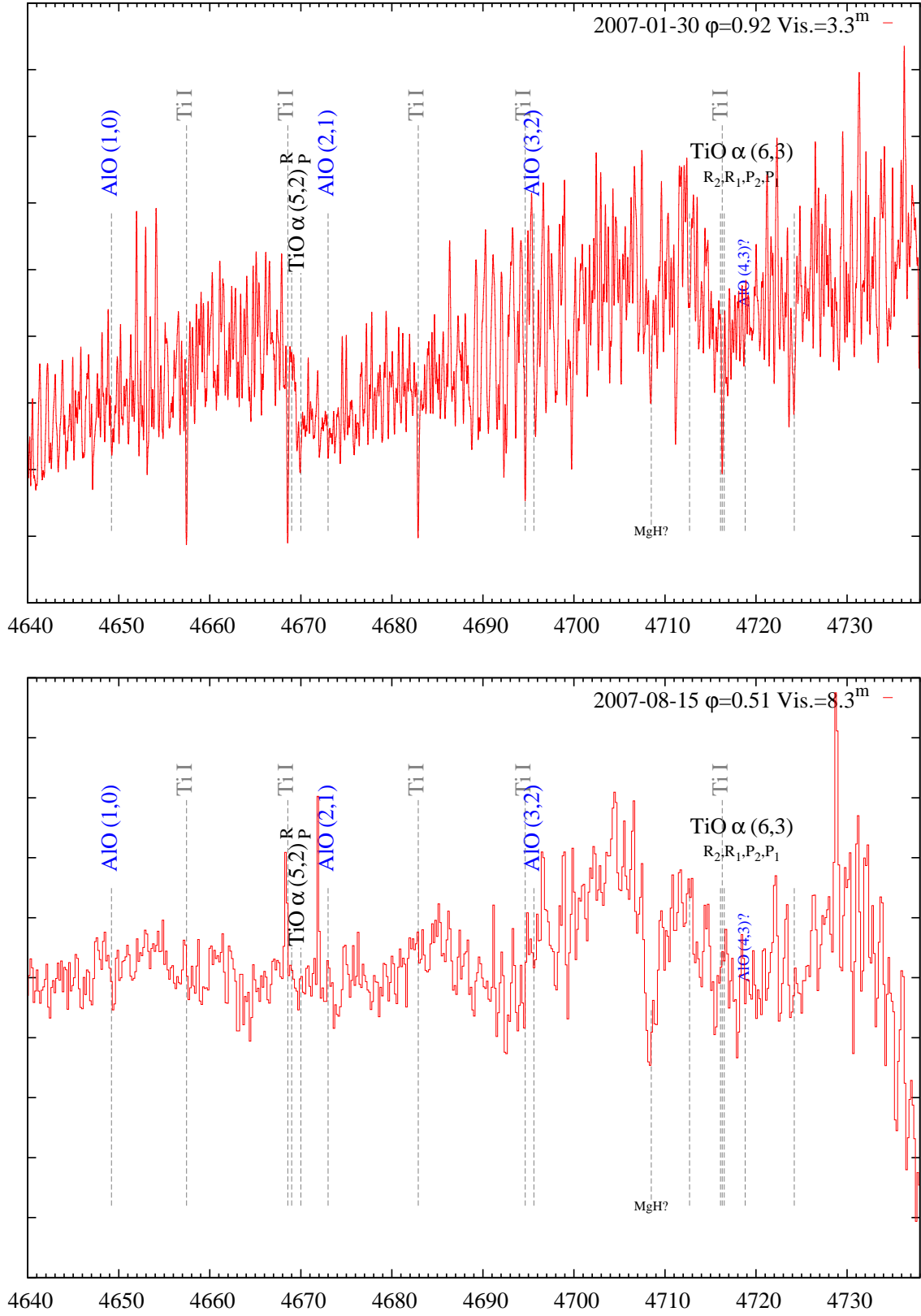


Fig. C.3. Continued.

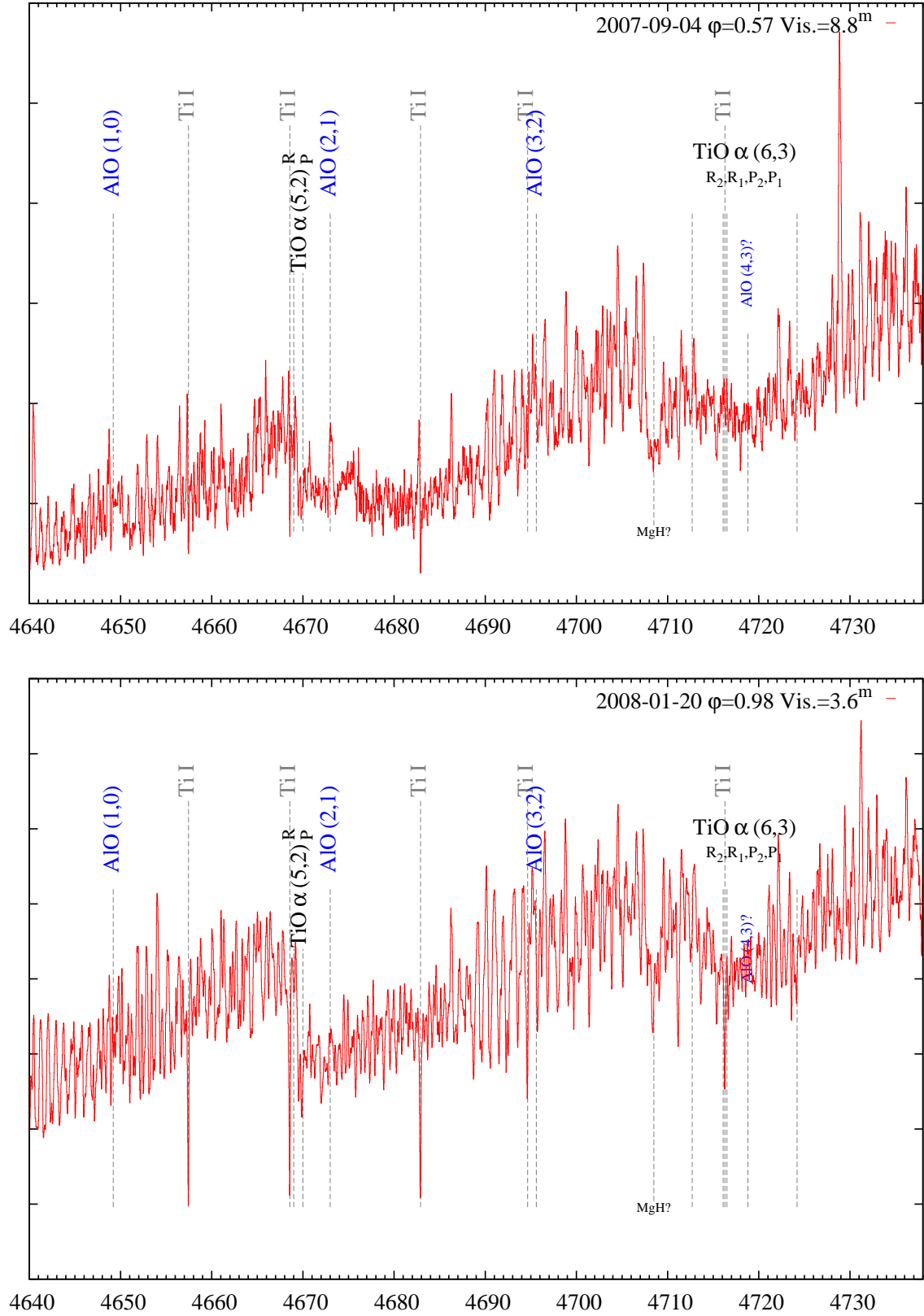


Fig. C.3. Continued.

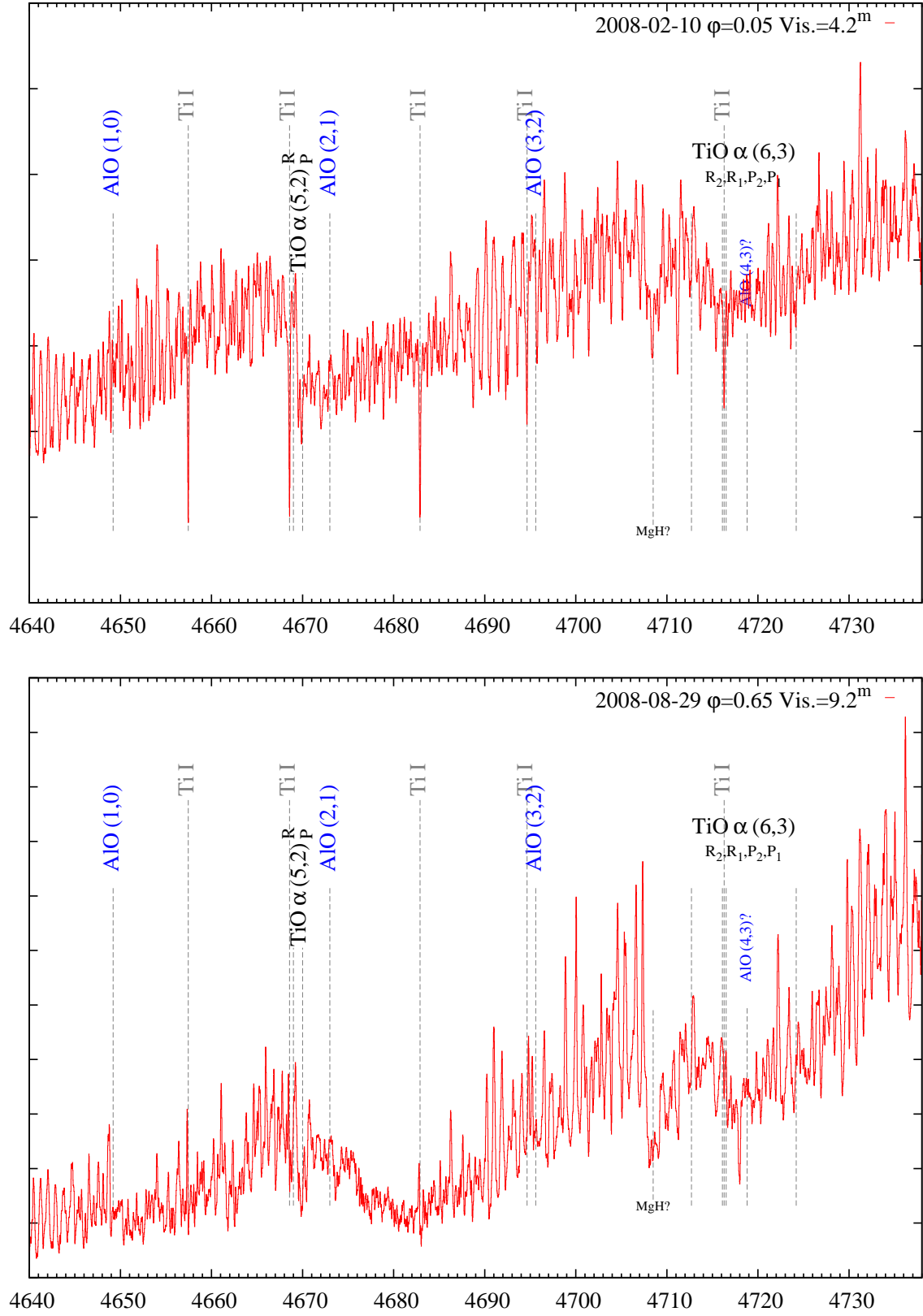


Fig. C.3. Continued.

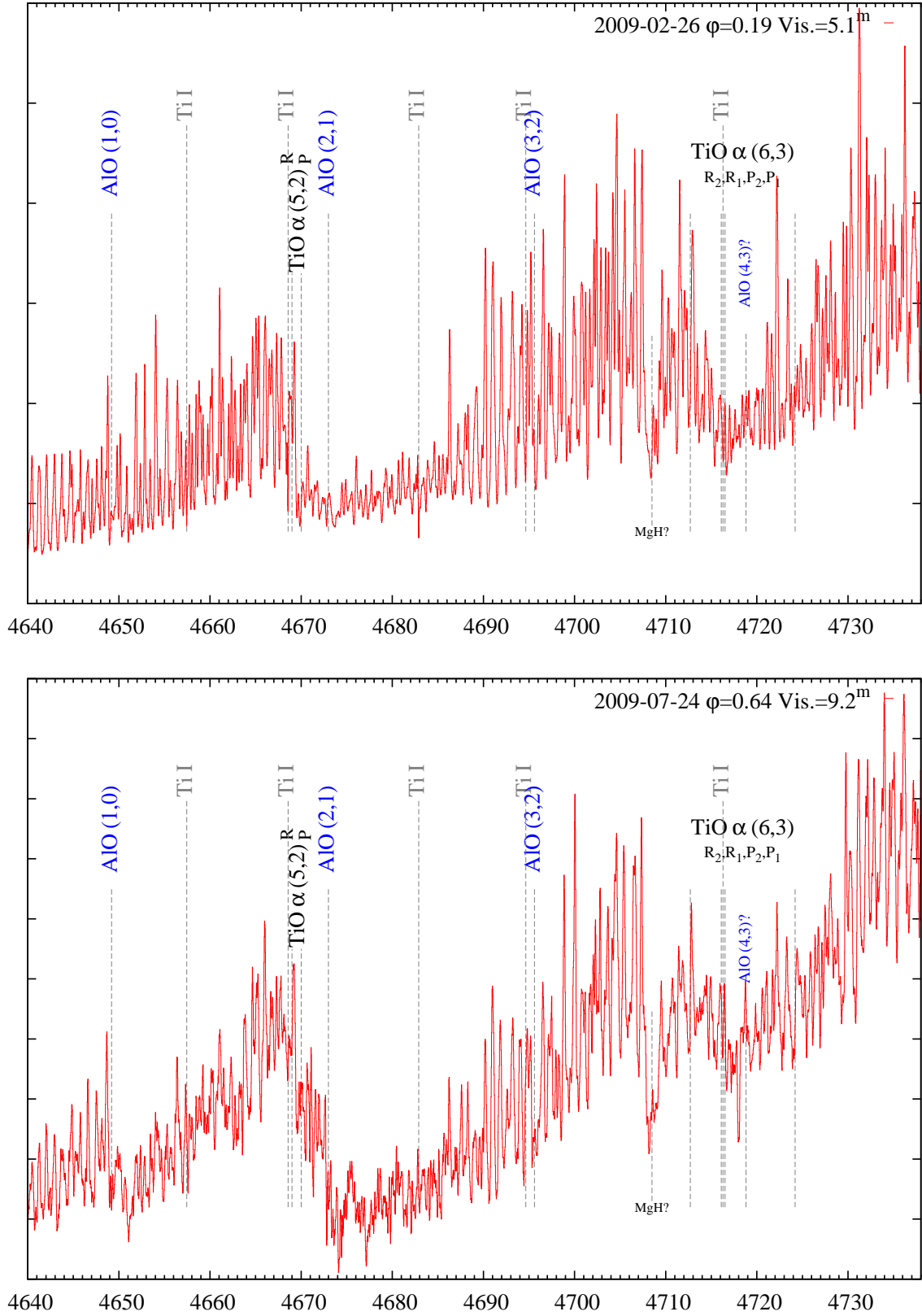


Fig. C.3. Continued.

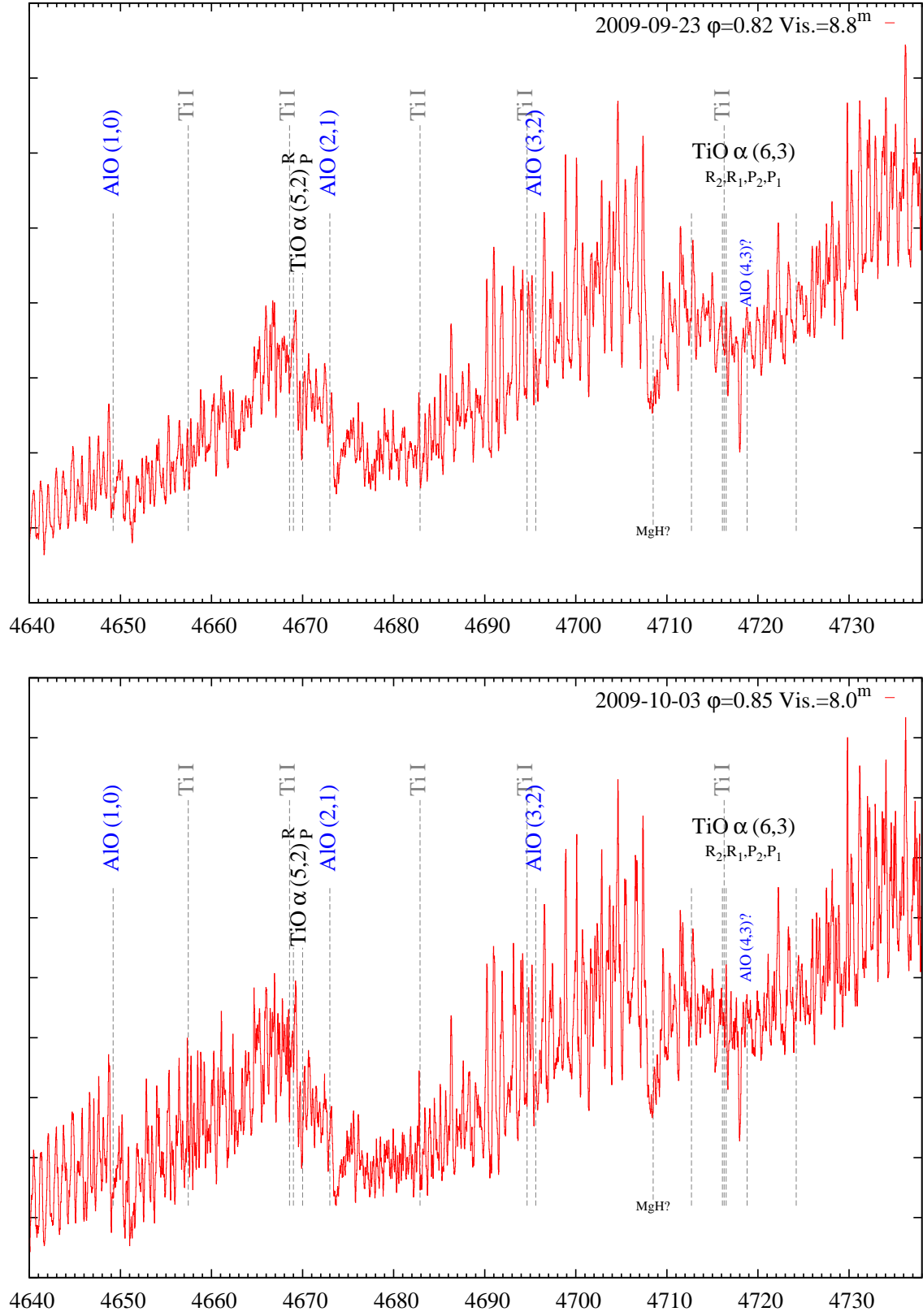


Fig. C.3. Continued.

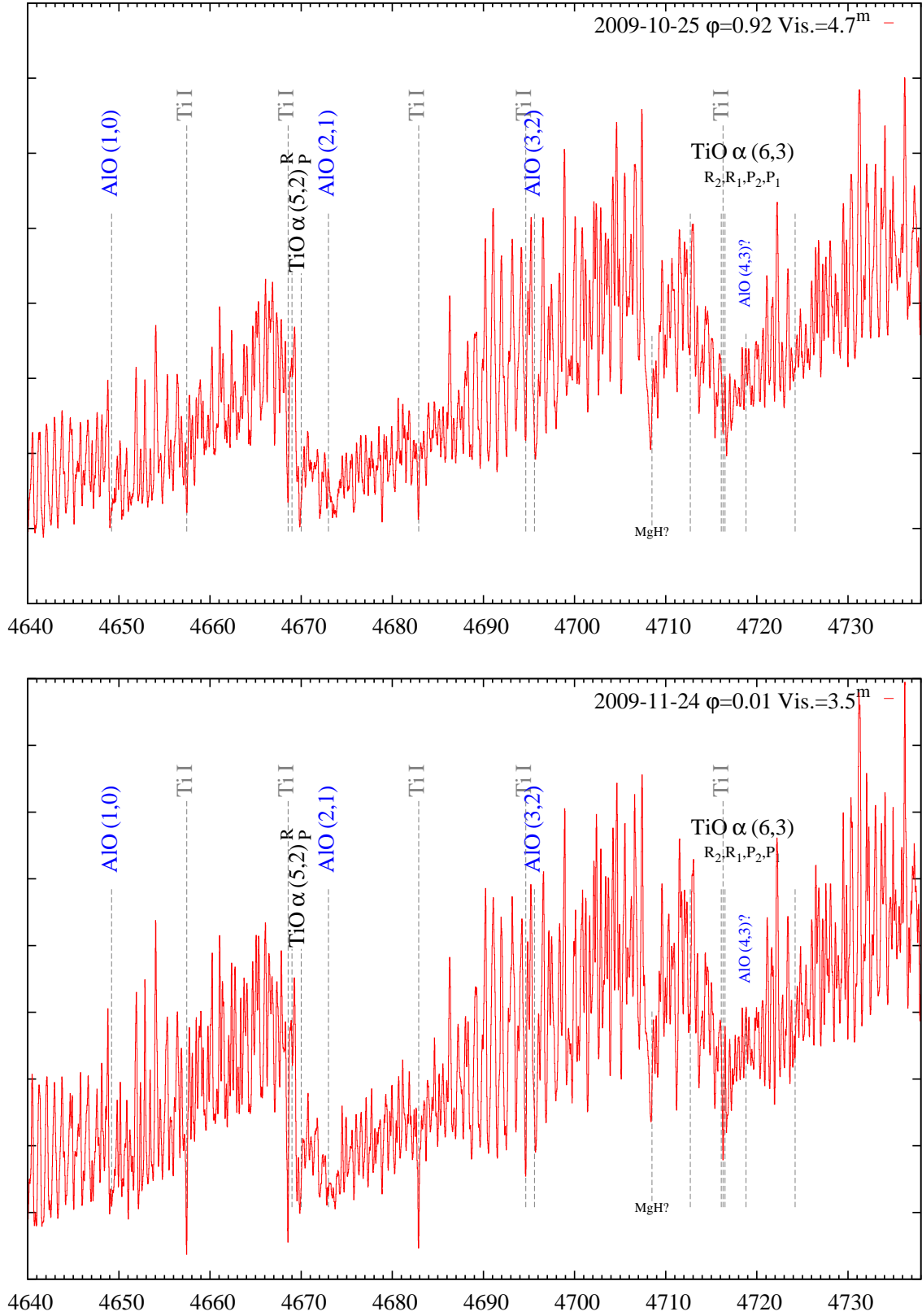


Fig. C.3. Continued.



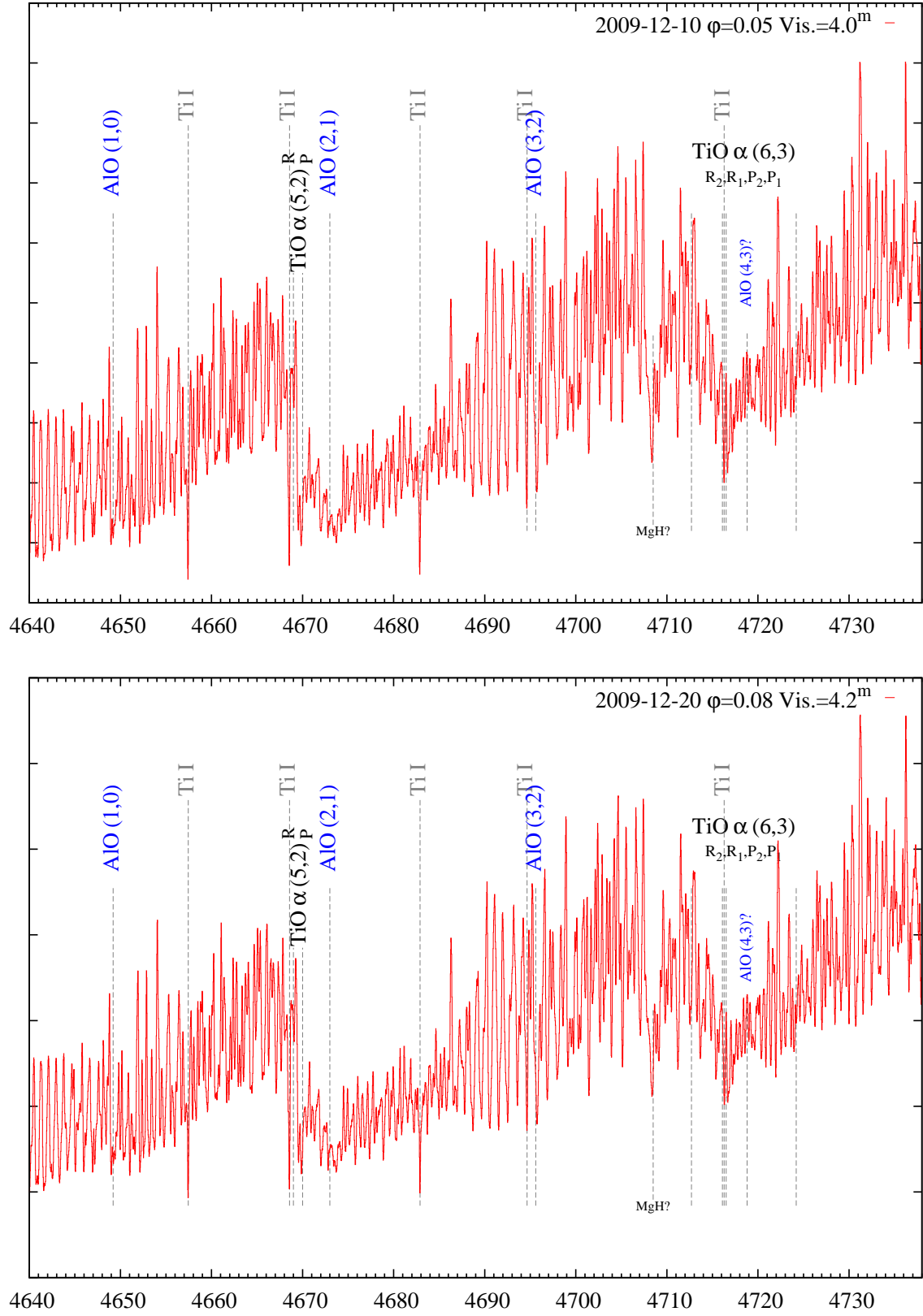


Fig. C.3. Continued.

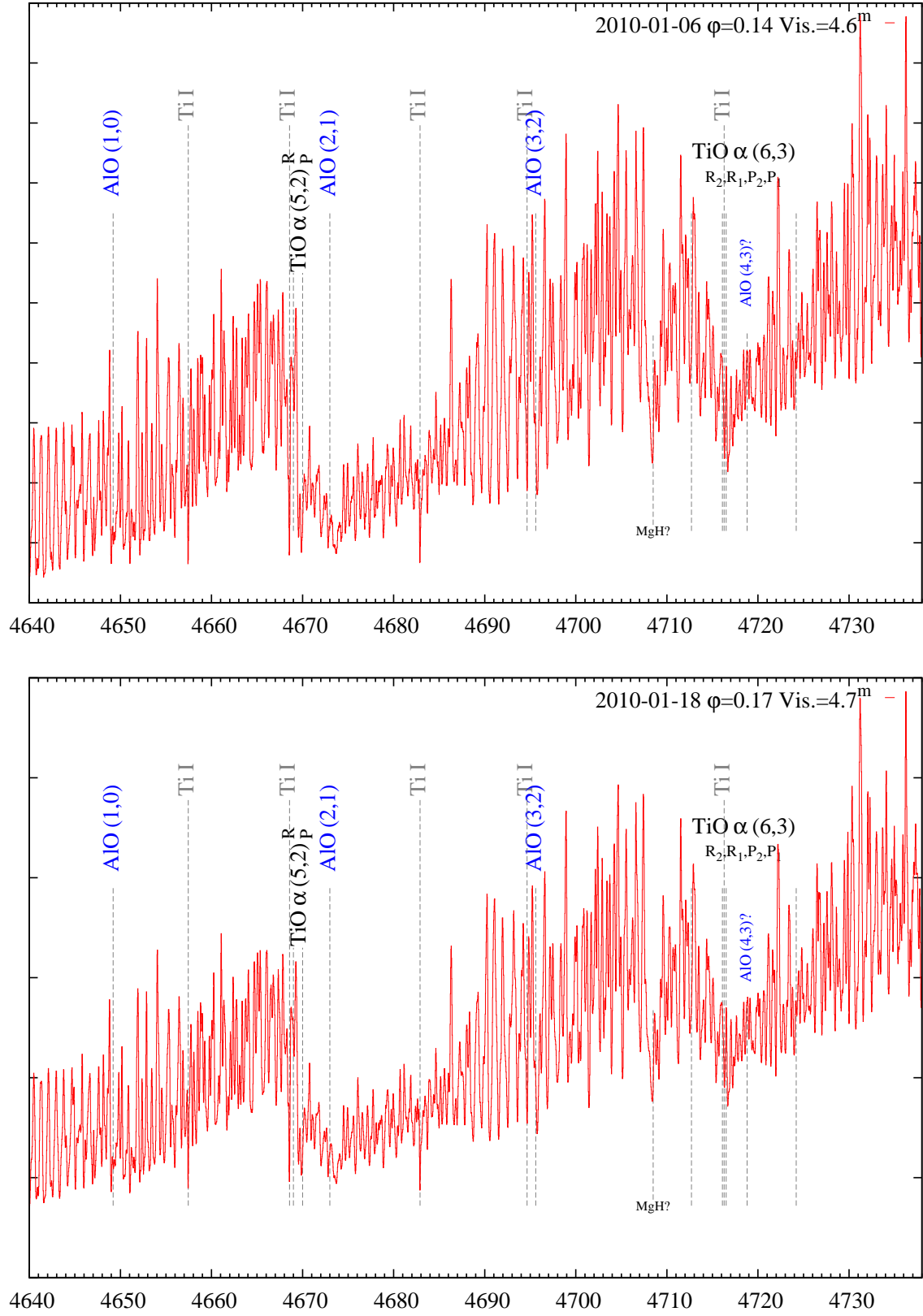


Fig. C.3. Continued.

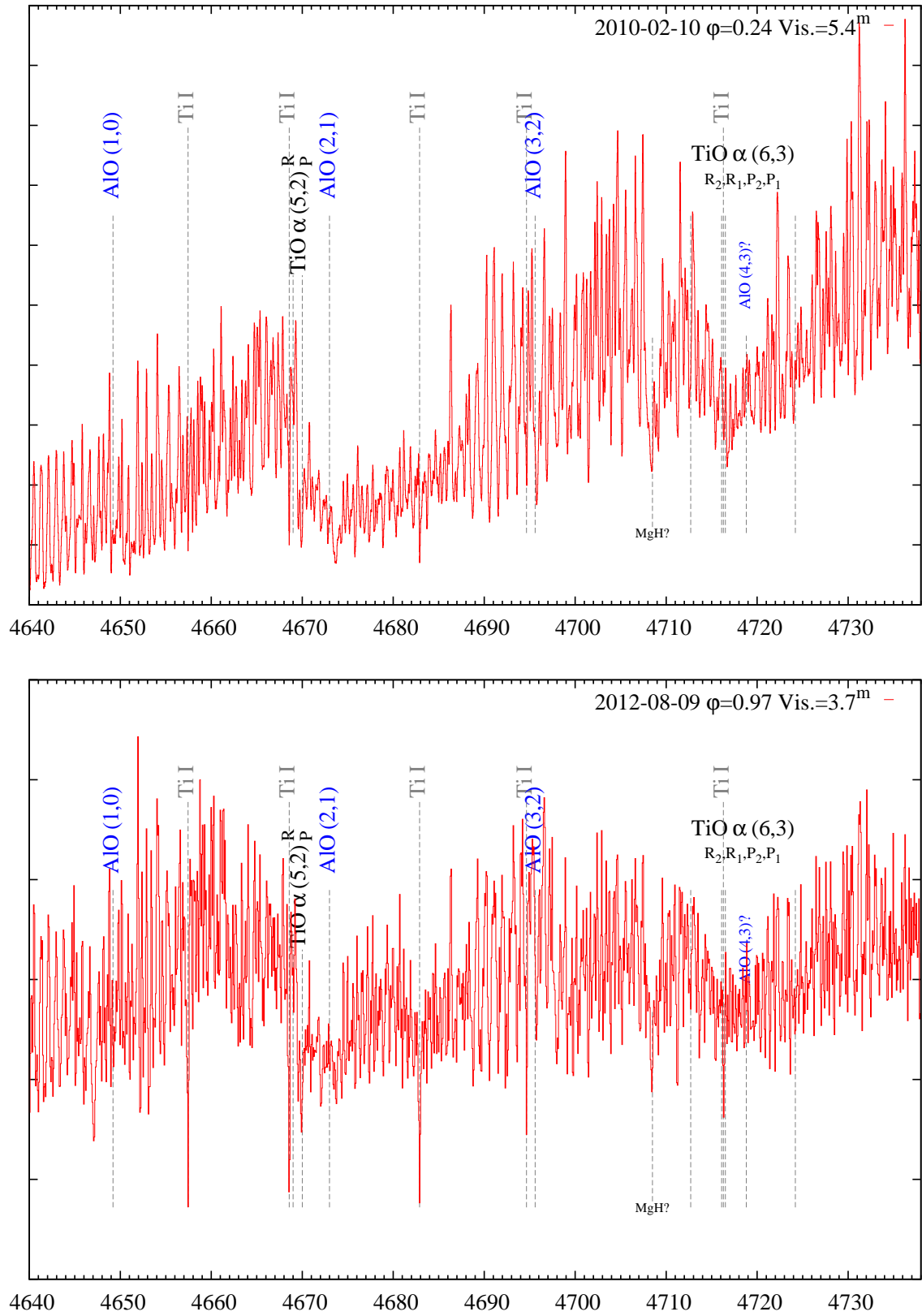
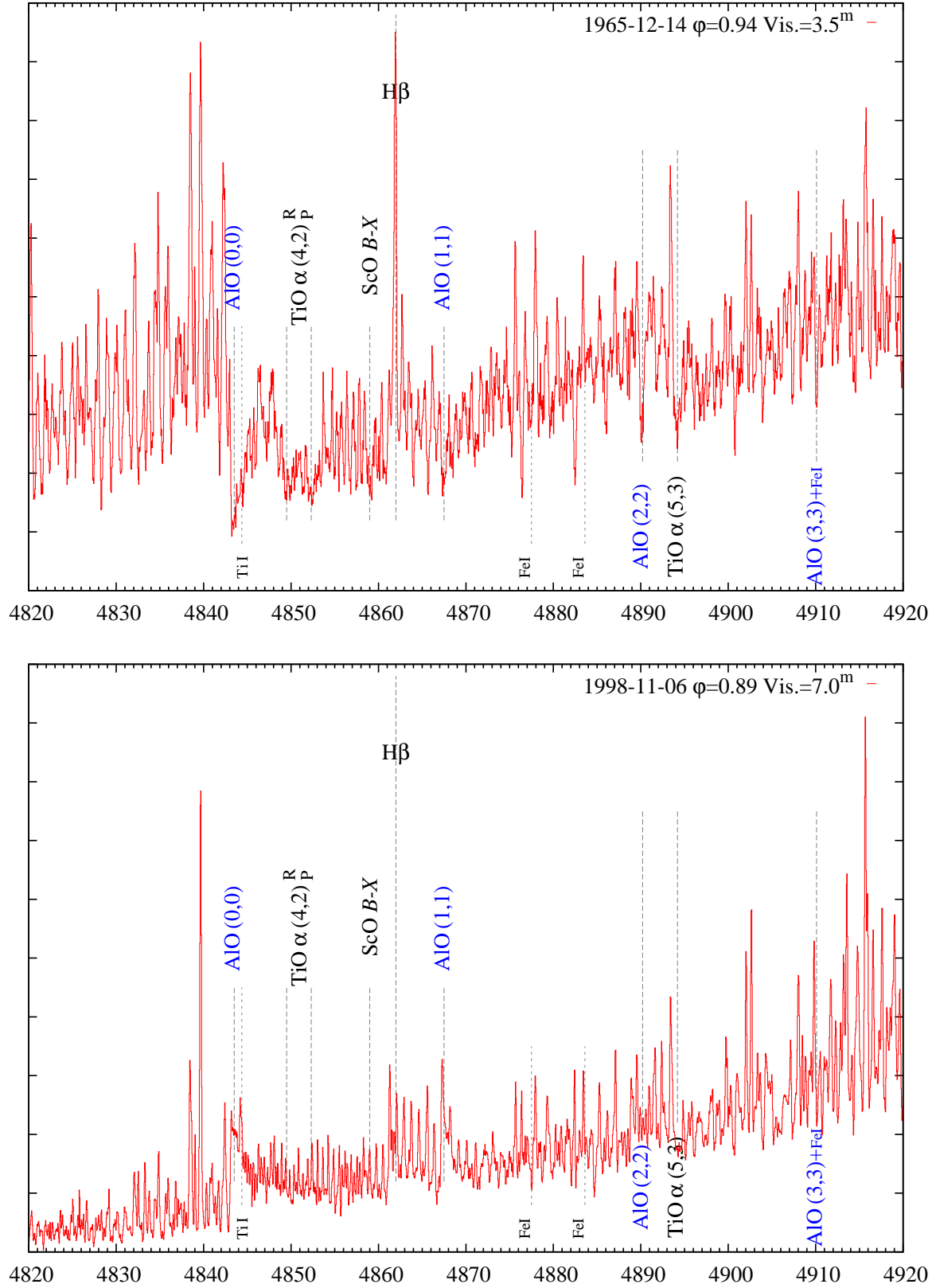


Fig. C.3. Continued.



**Fig. C.4.** The same as Fig. C.2 but for the  $\Delta\nu=0$  sequence of AlO  $B-X$ . Spectra from Narval are affected by an imperfect combination of different echelle orders in the 4877–4881  $\text{\AA}$  range. The spectrum from 2007-08-15 was divided by a high-order polynomial.

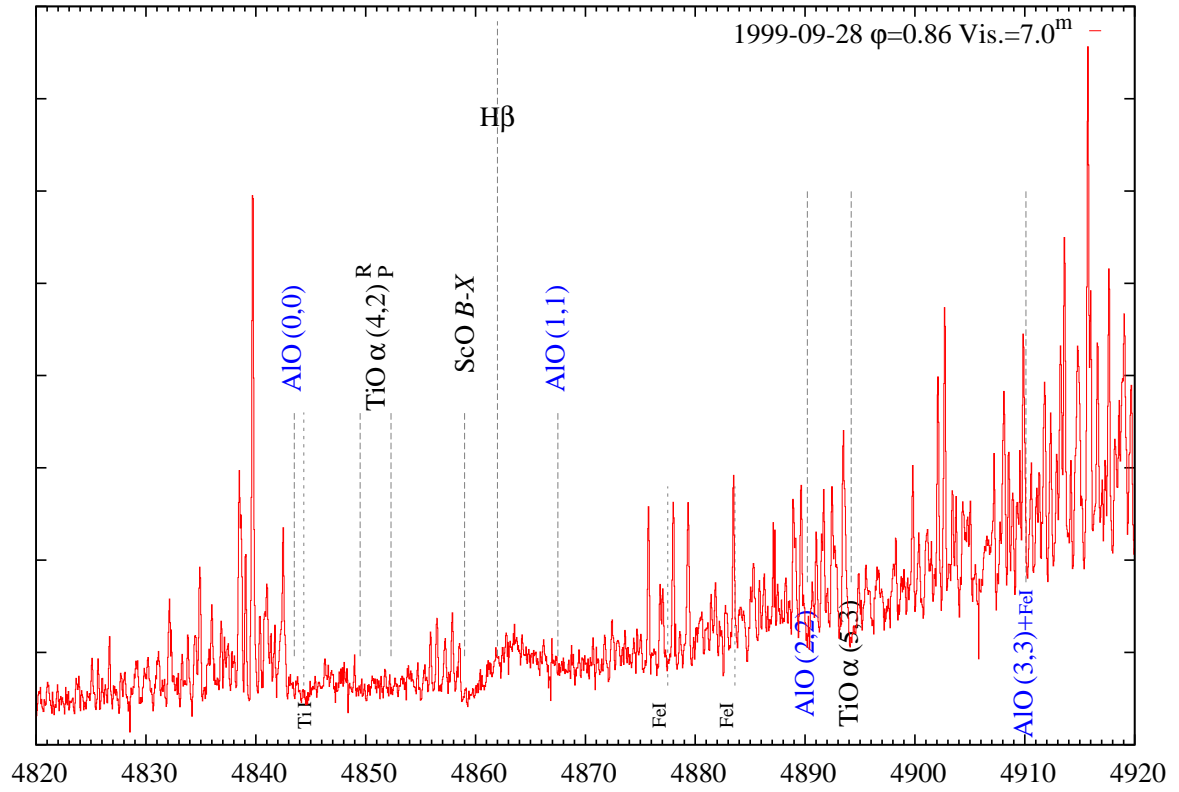
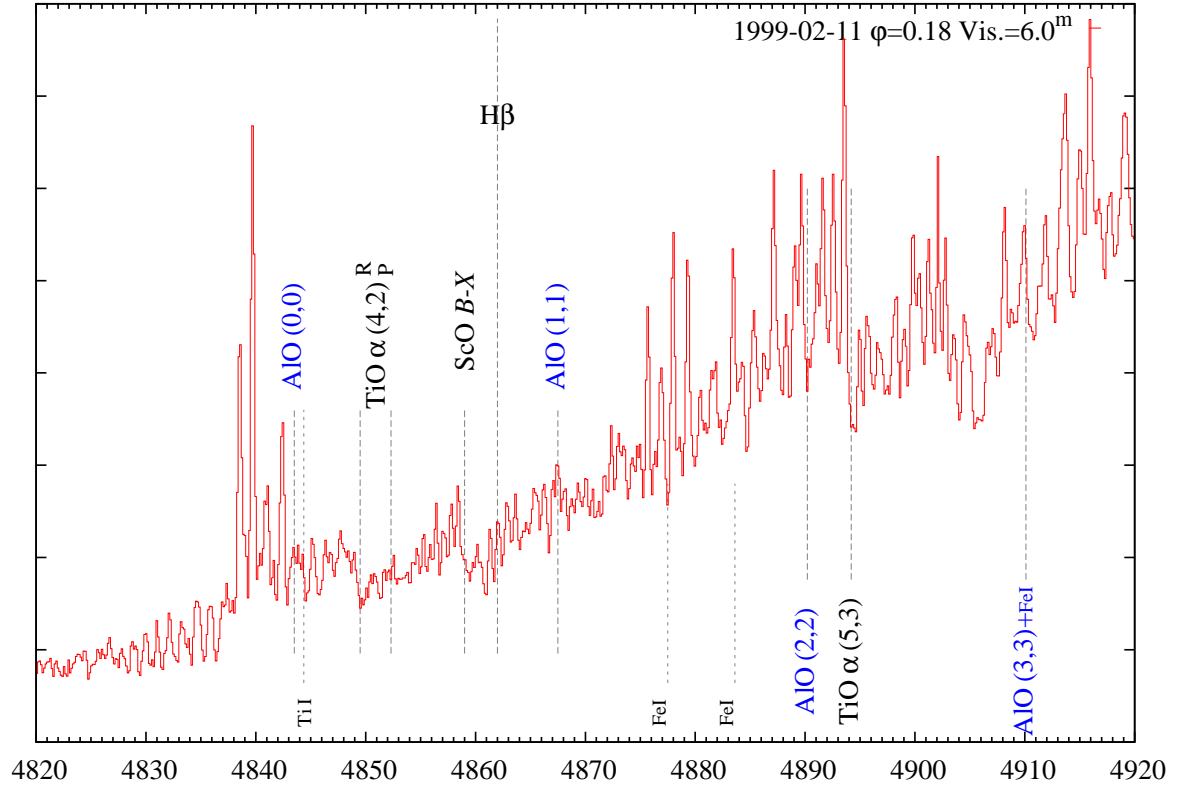


Fig. C.4. Continued.

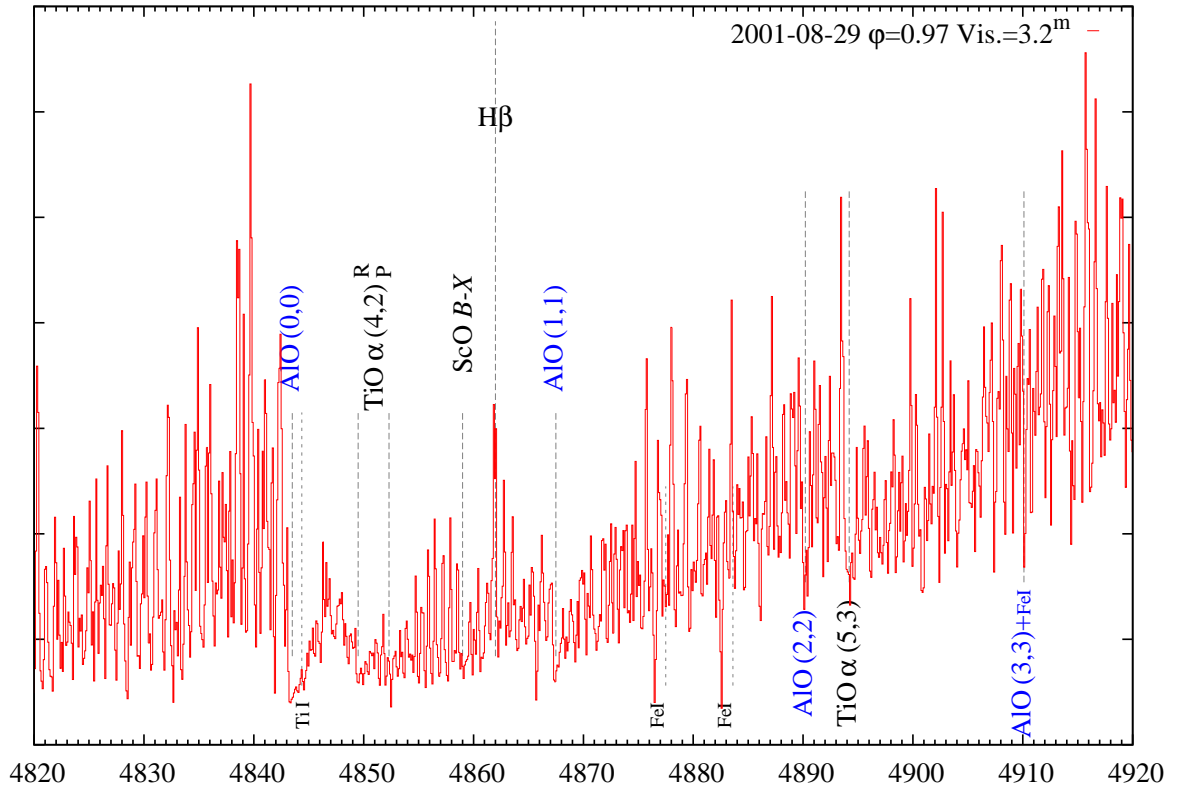
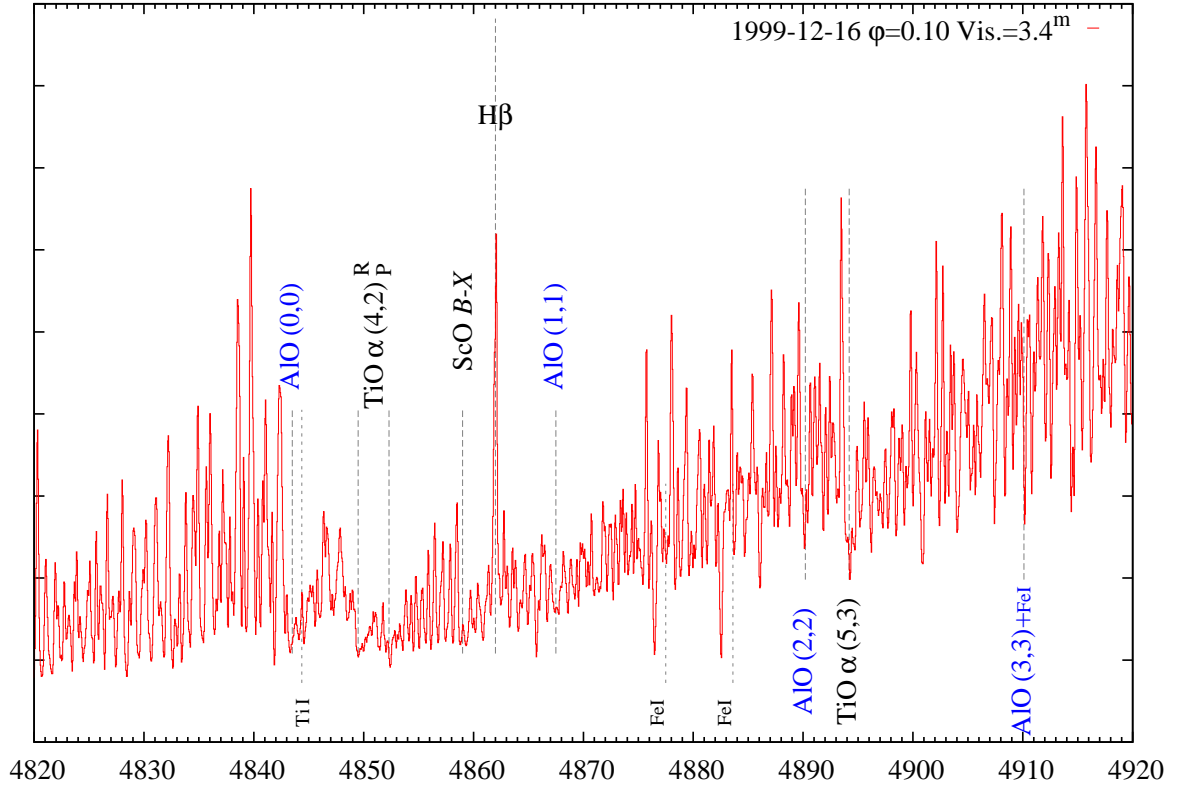


Fig. C.4. Continued.

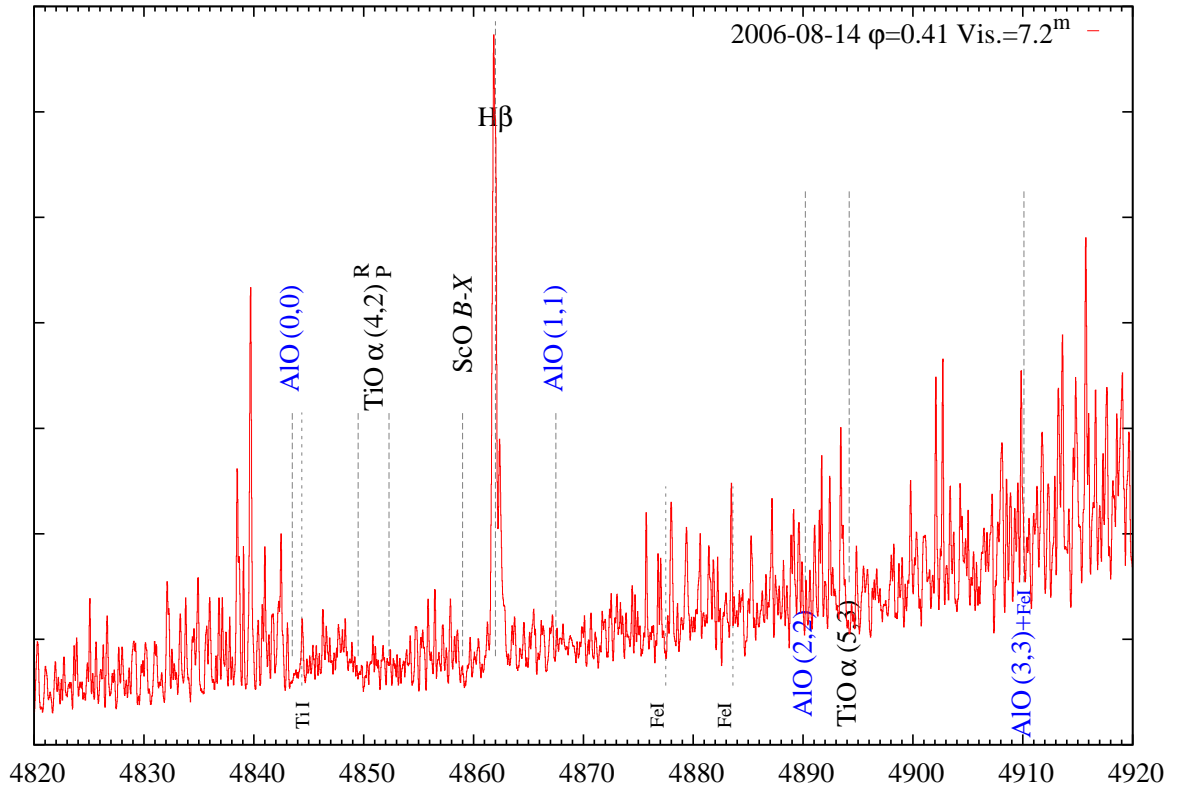
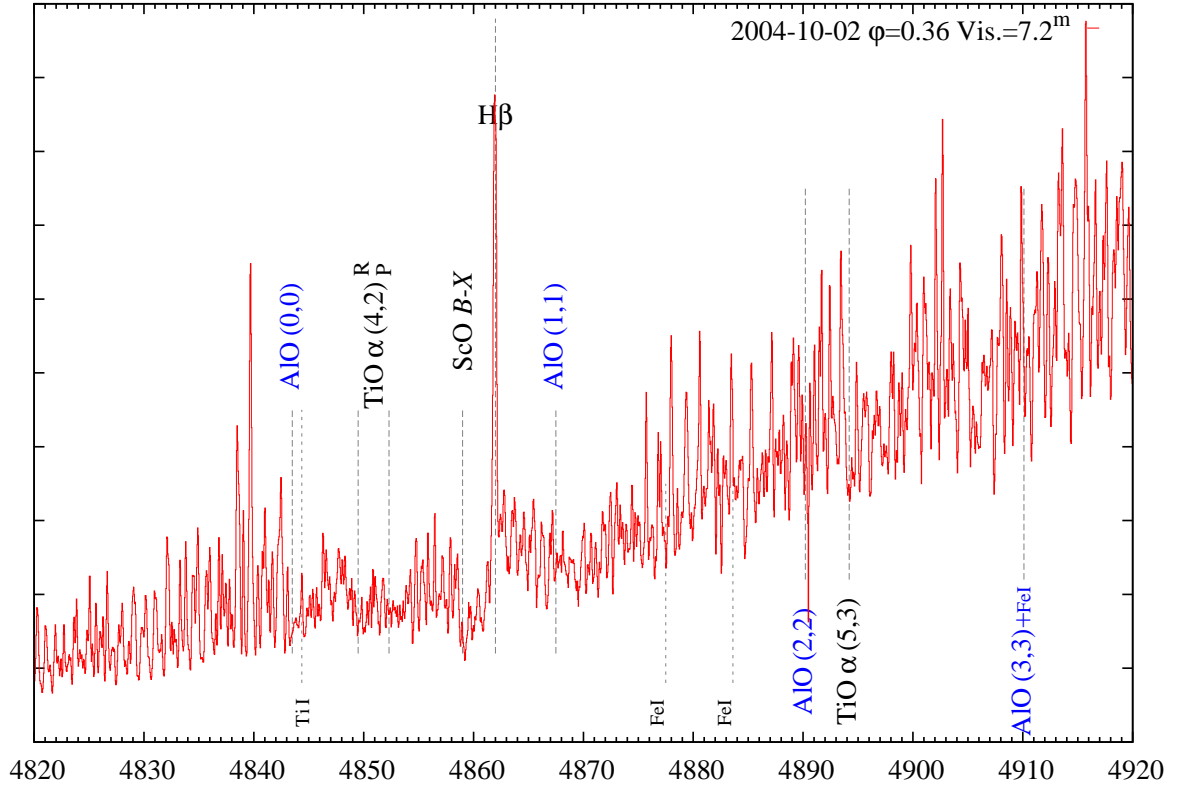


Fig. C.4. Continued.

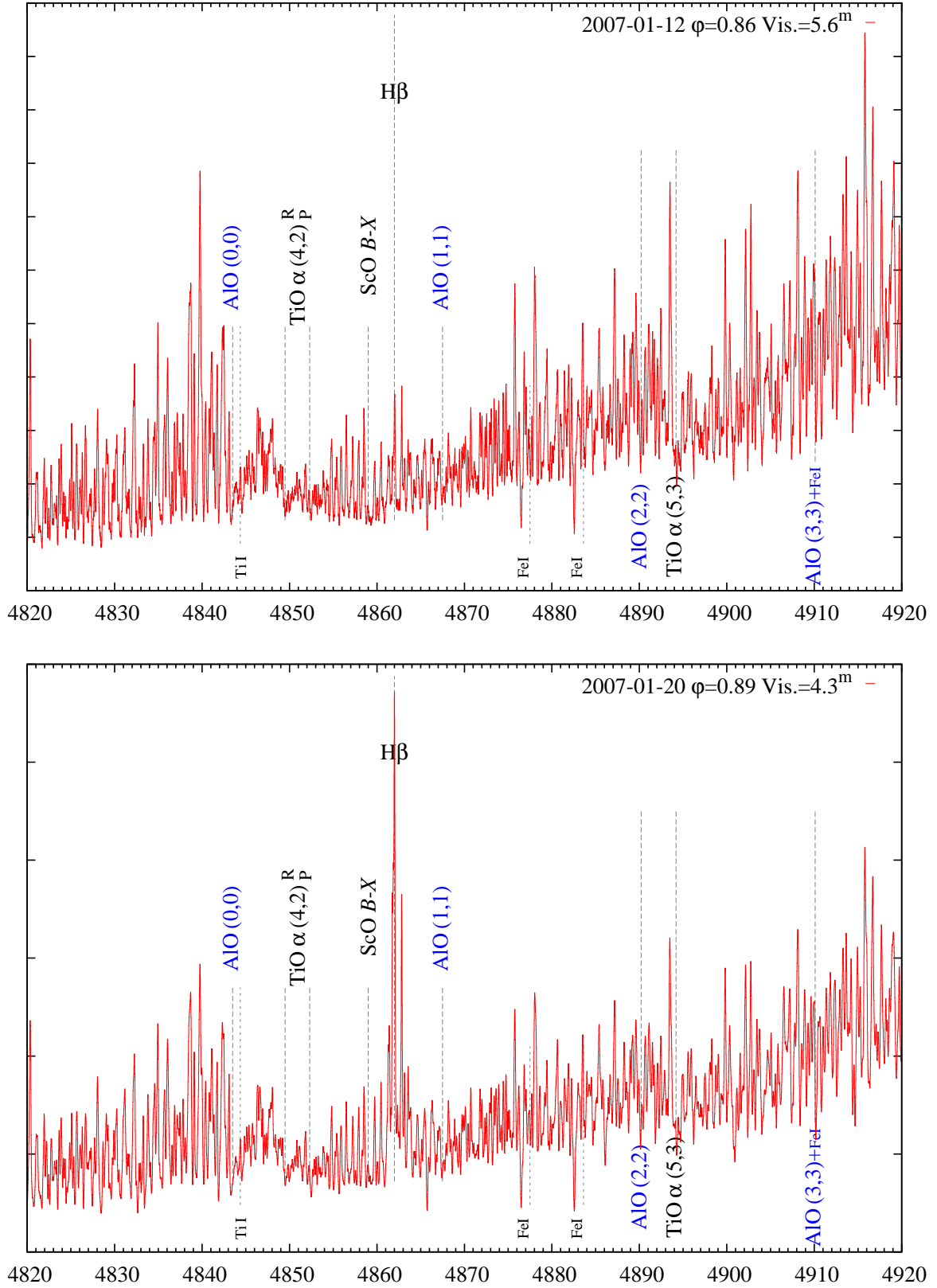


Fig. C.4. Continued.



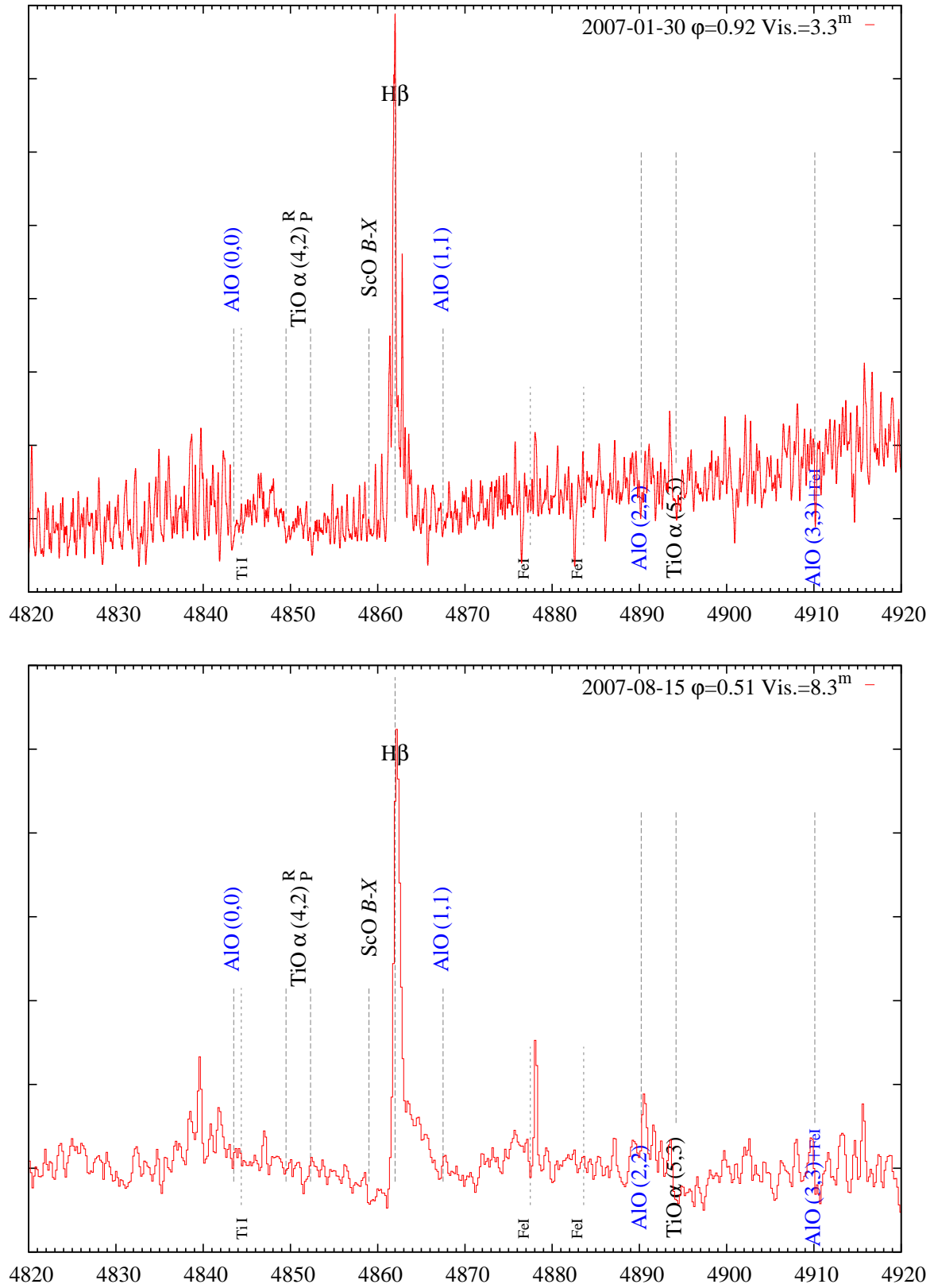


Fig. C.4. Continued.

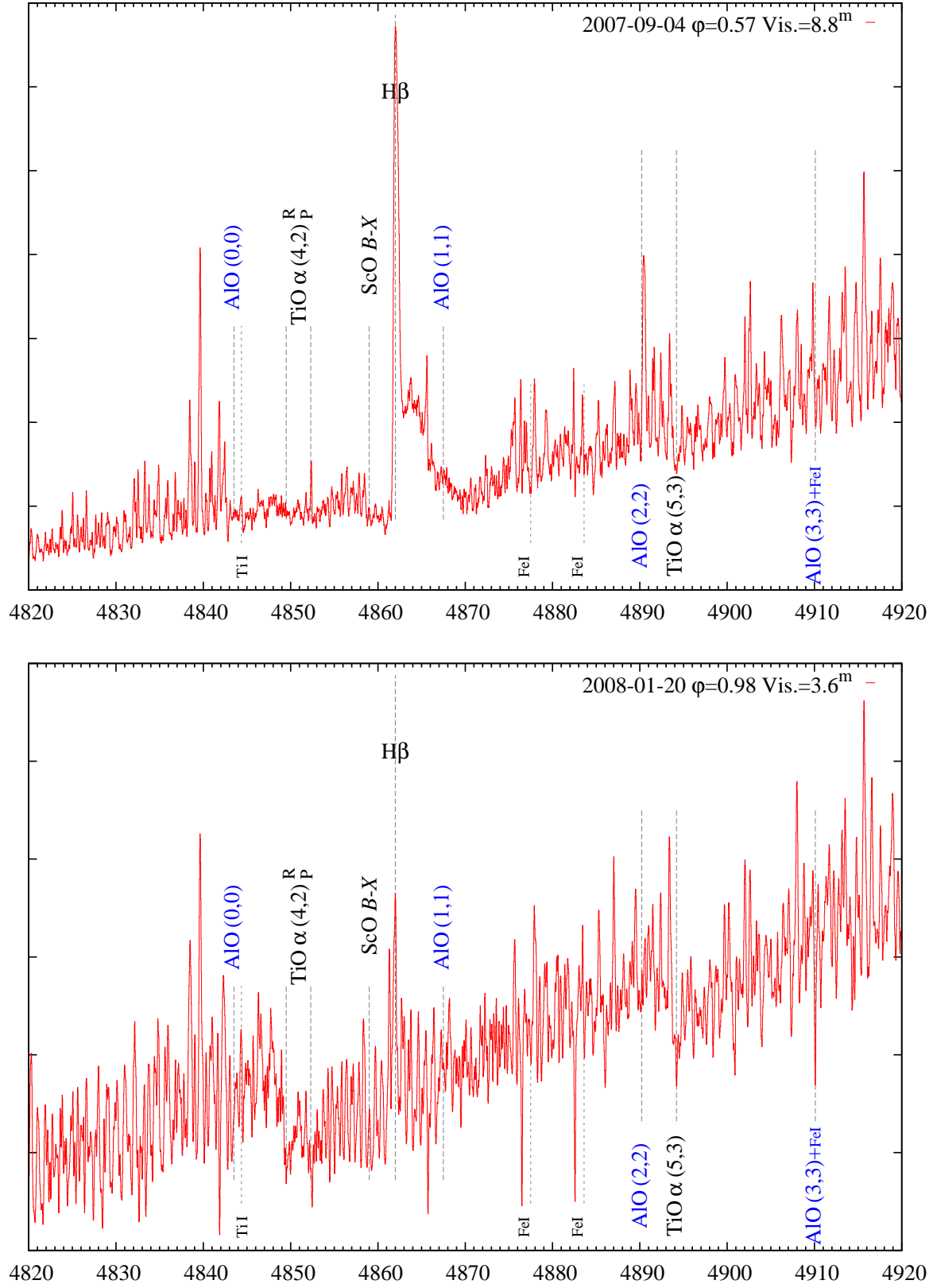


Fig. C.4. Continued.

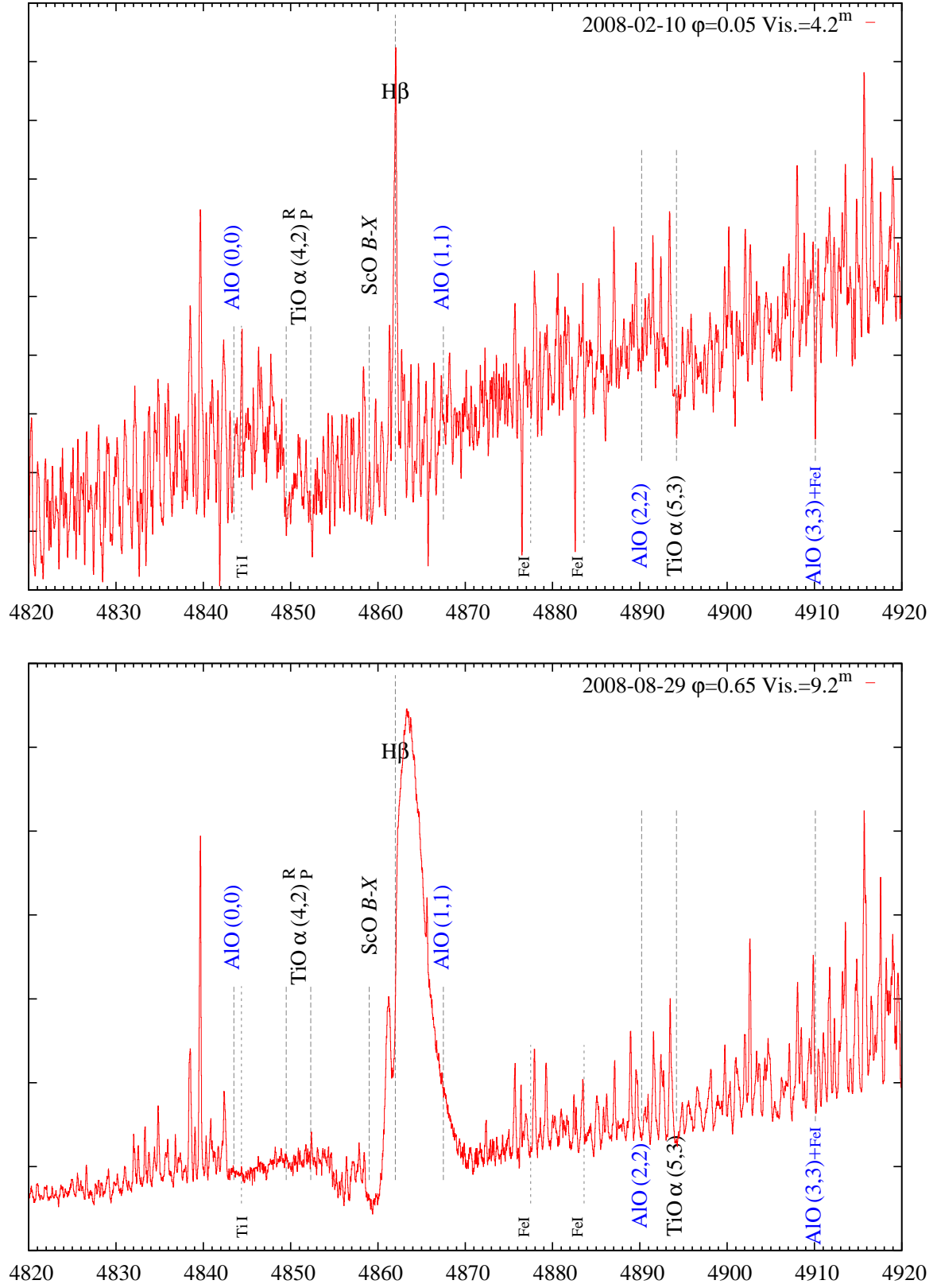


Fig. C.4. Continued.

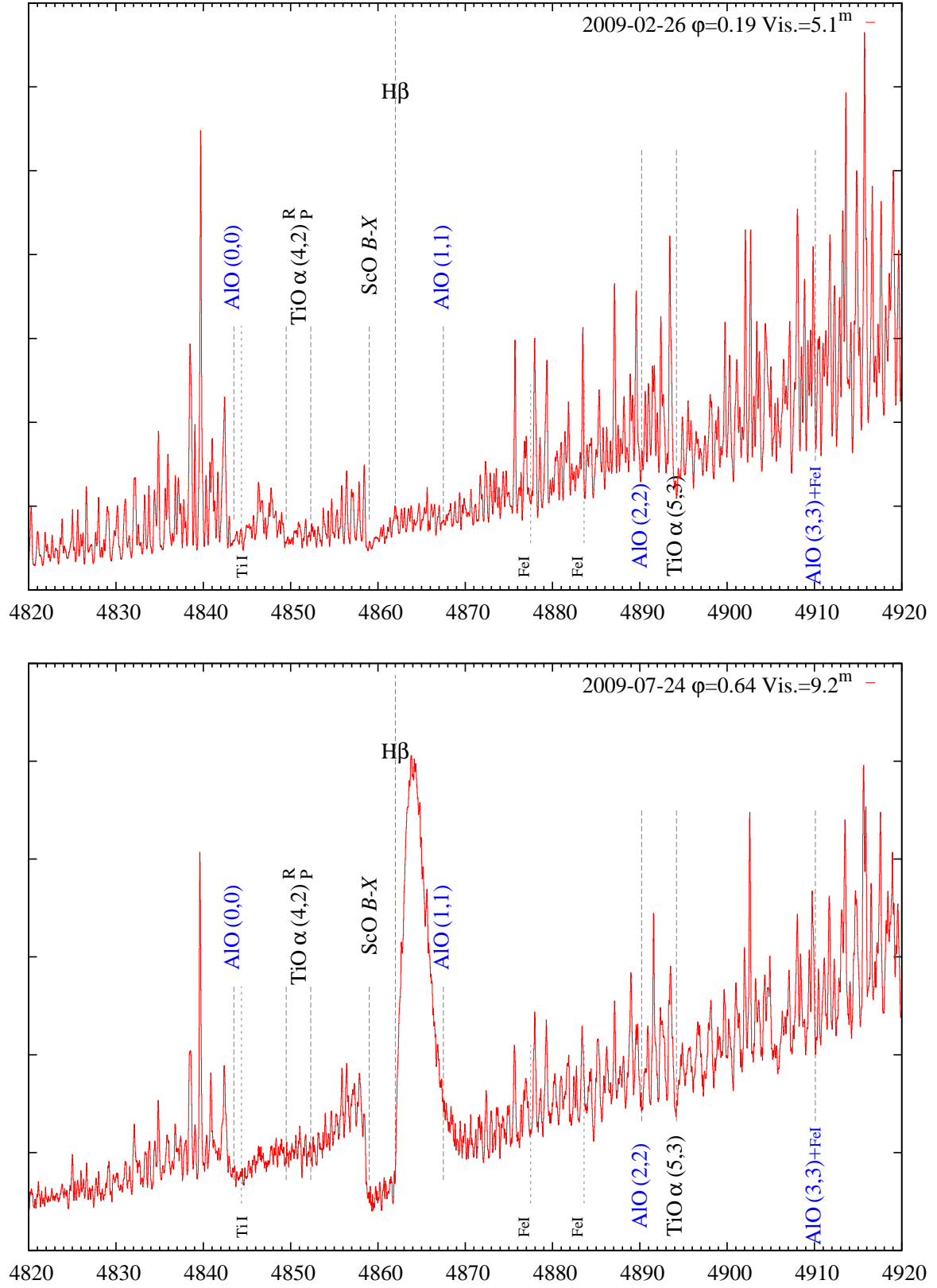
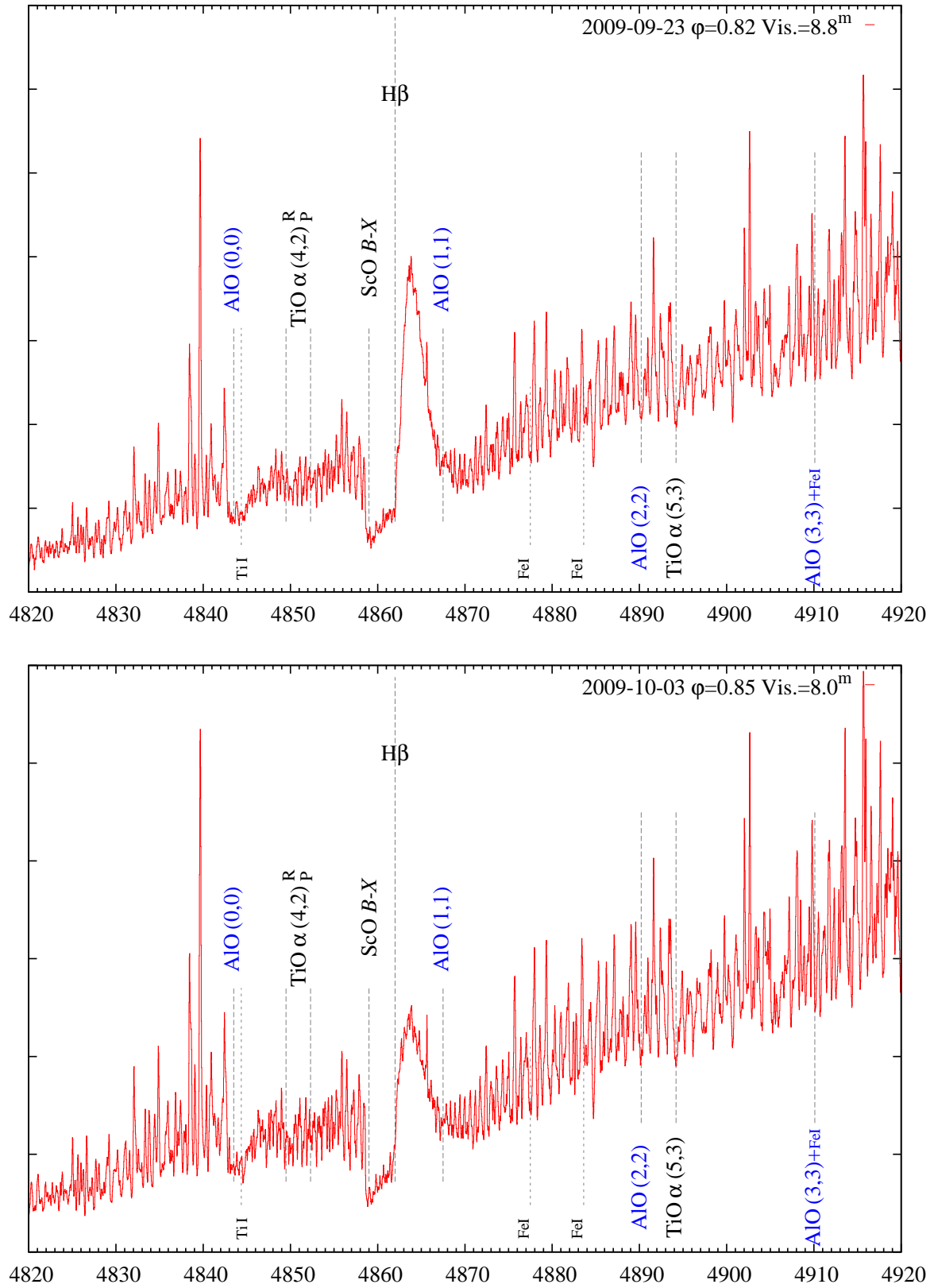


Fig. C.4. Continued.



**Fig. C.4.** Continued.

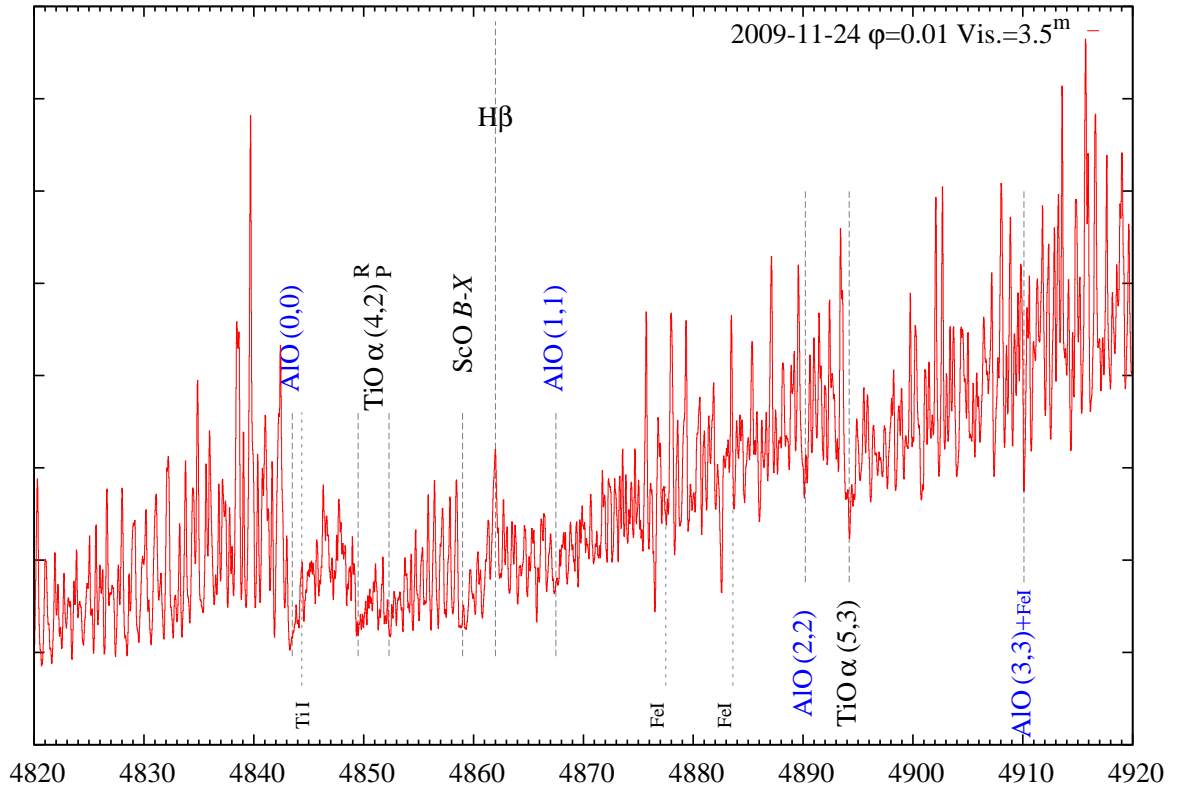
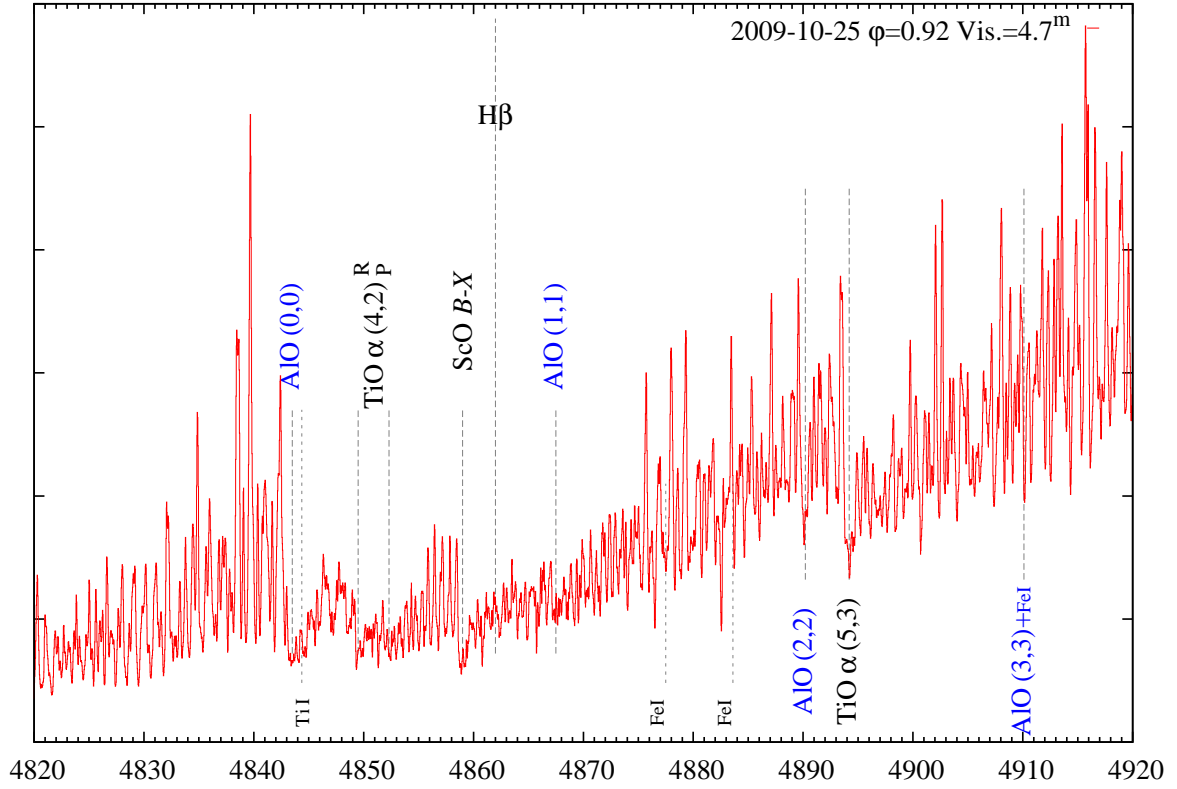


Fig. C.4. Continued.

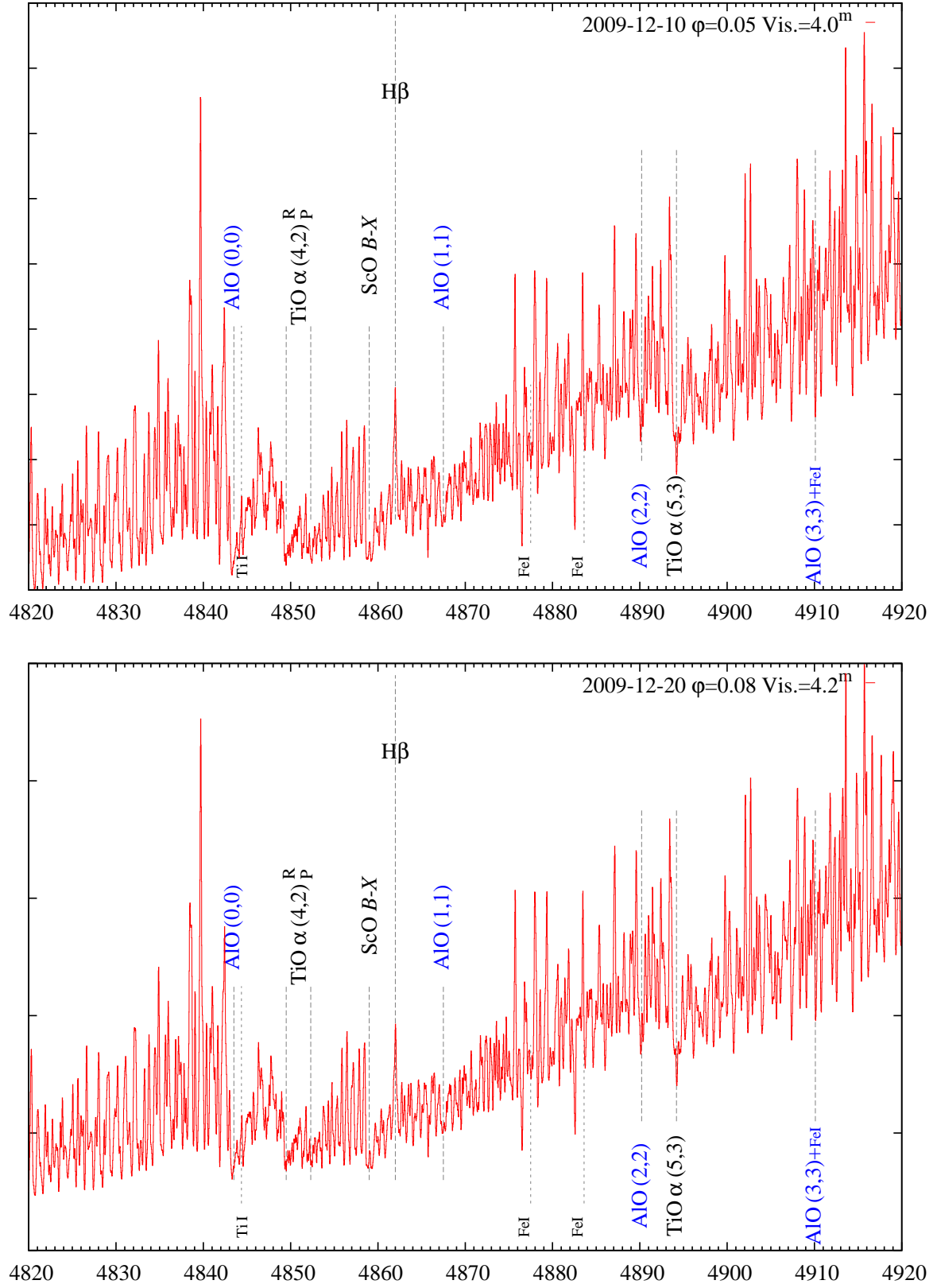


Fig. C.4. Continued.

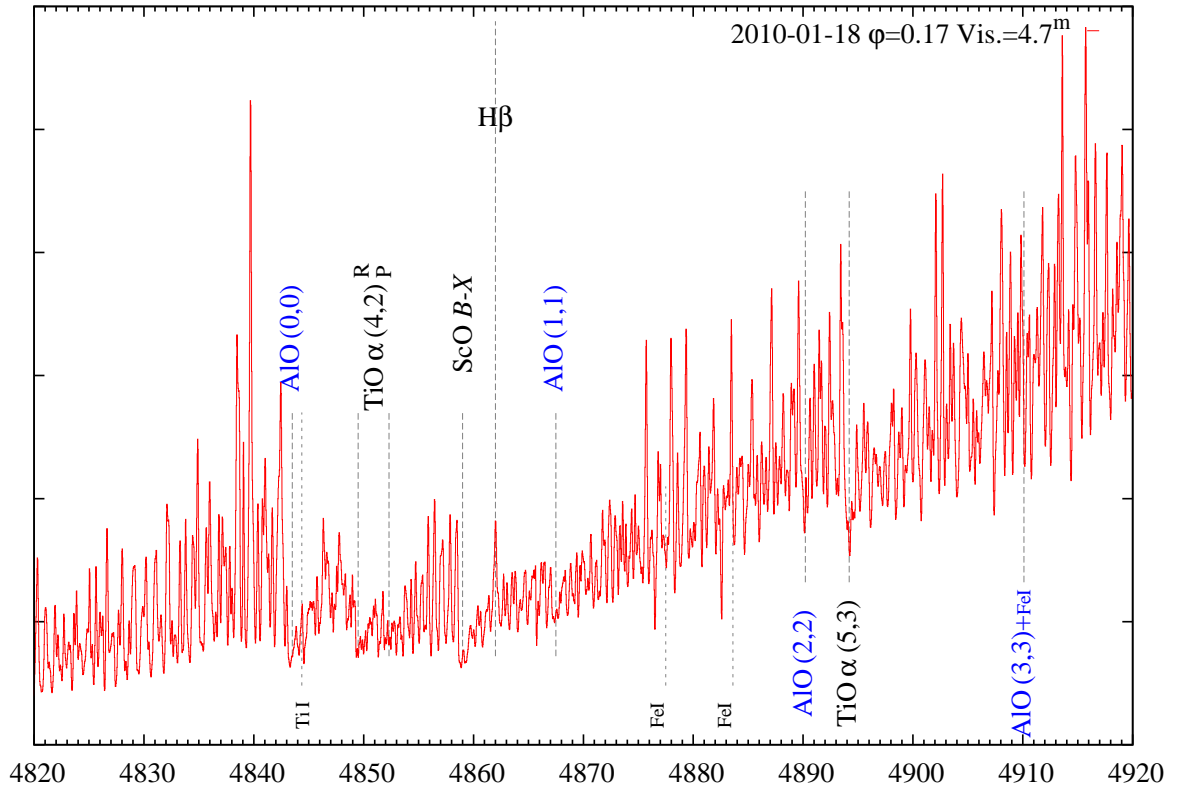
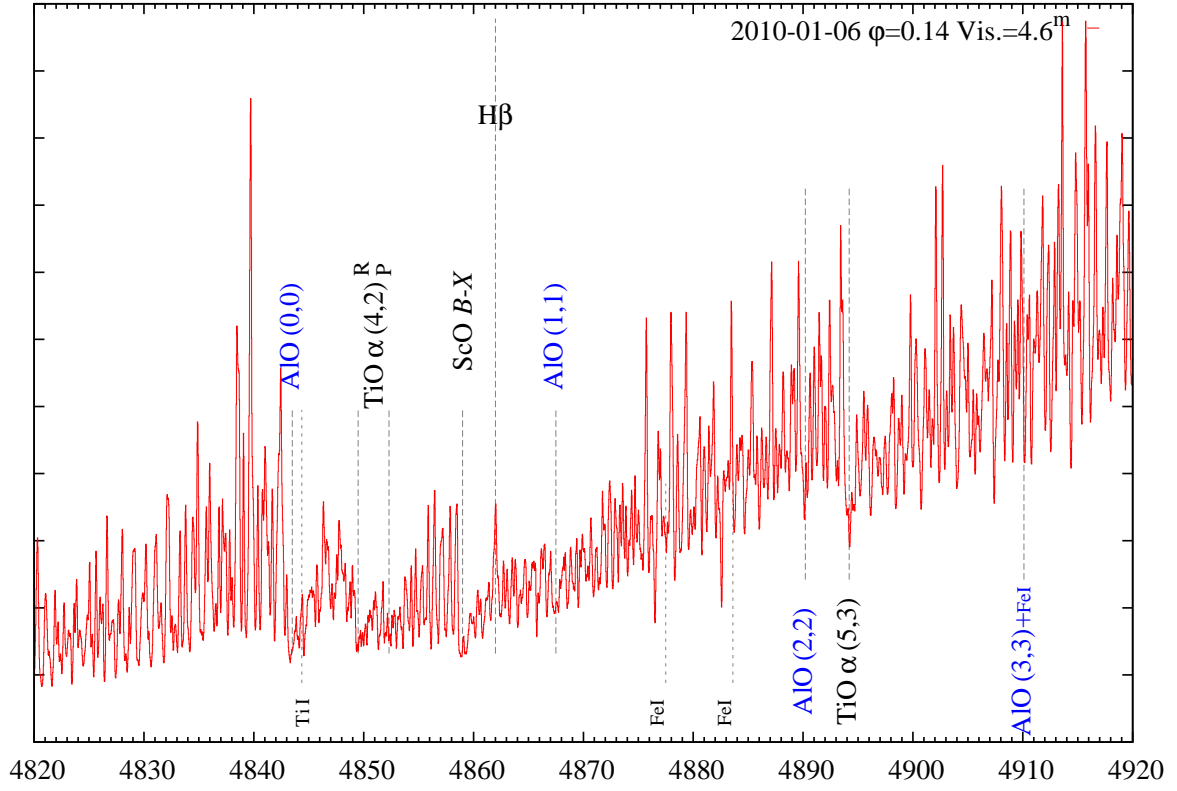


Fig. C.4. Continued.



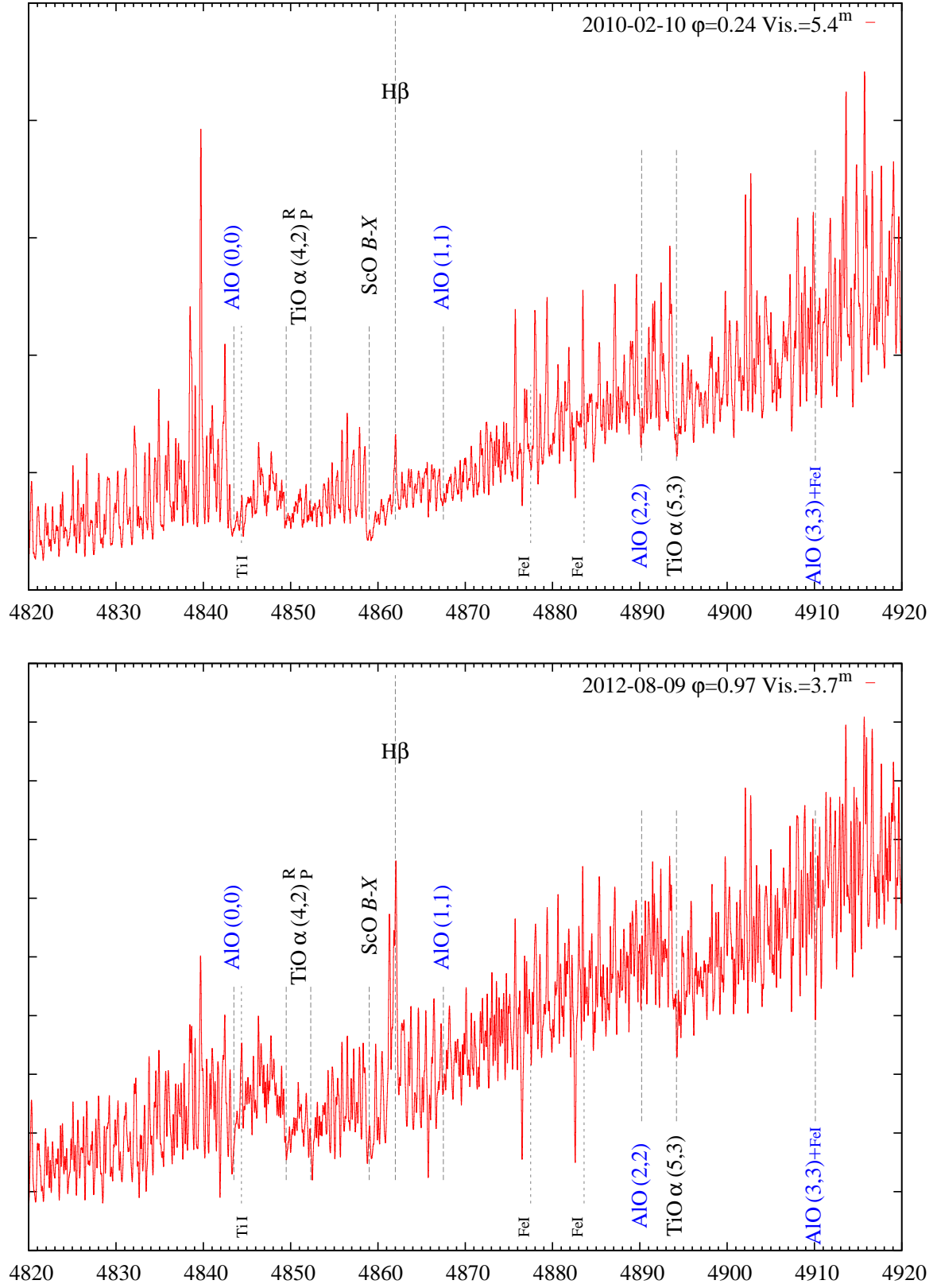
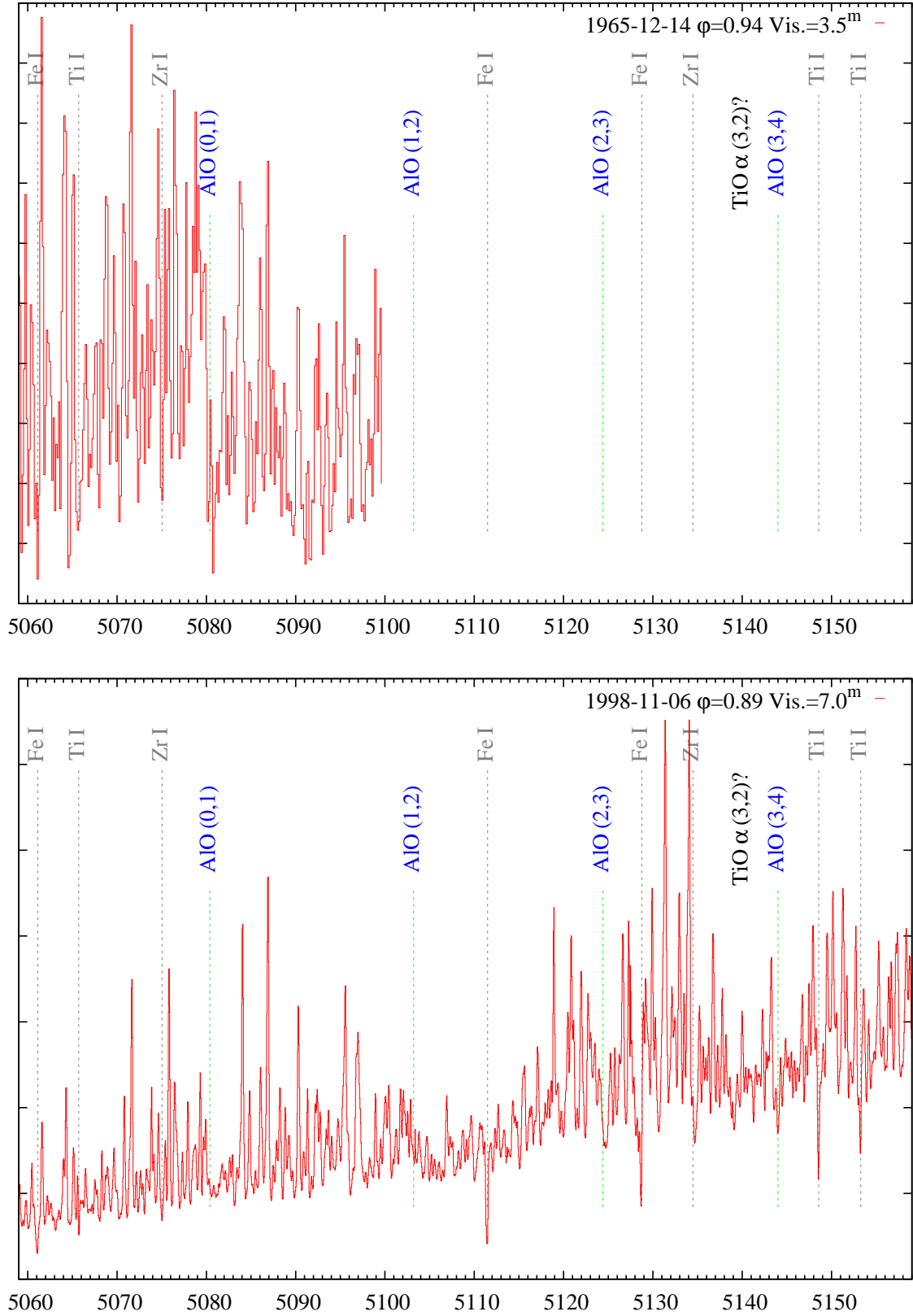


Fig. C.4. Continued.



**Fig. C.5.** The same as Fig. C.2 but for the  $\Delta\nu=-1$  sequence of AlO  $B-X$ . The spectrum from 2007-08-15 was divided by a high-order polynomial.

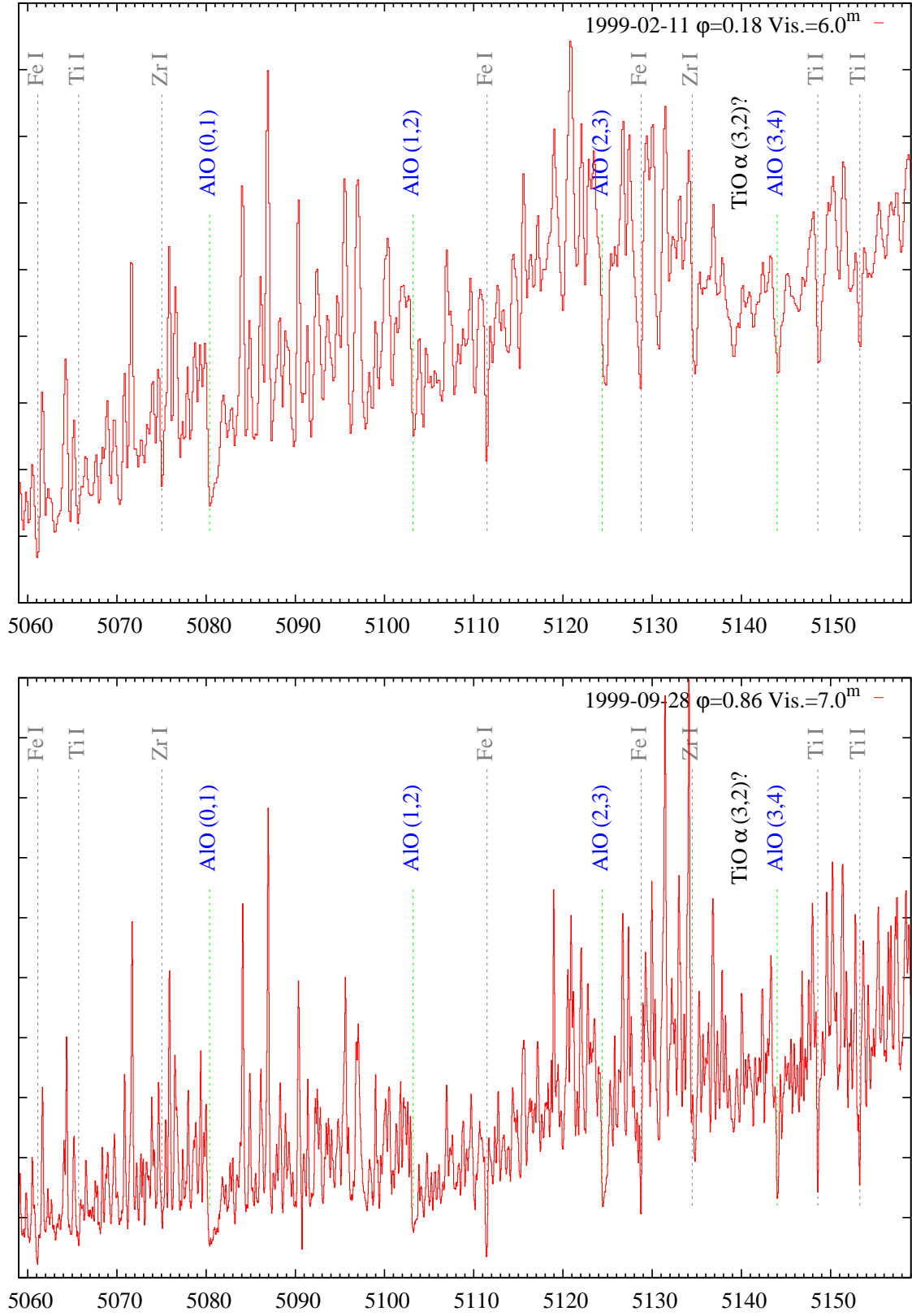


Fig. C.5. Continued.

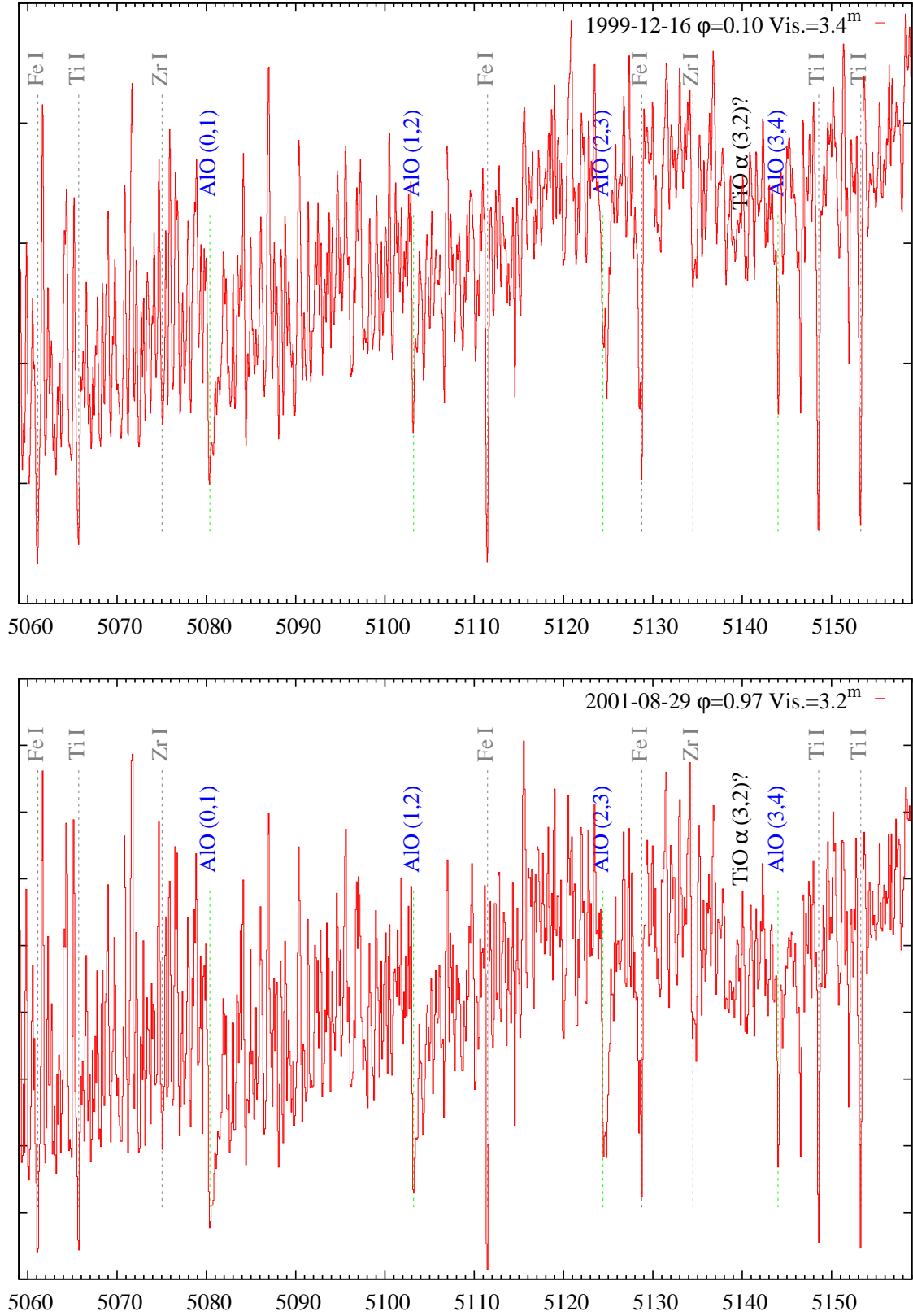


Fig. C.5. Continued.

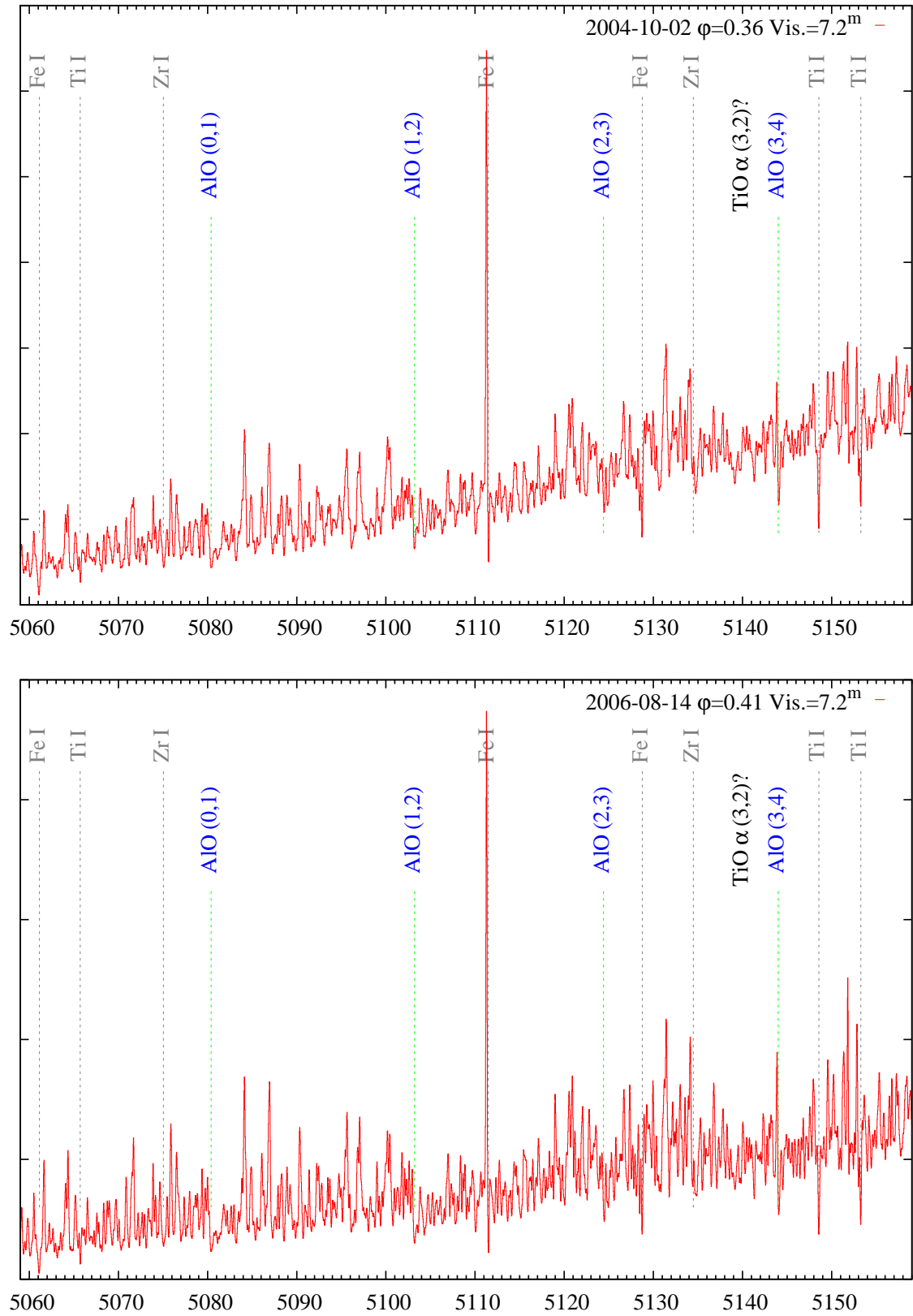


Fig. C.5. Continued.

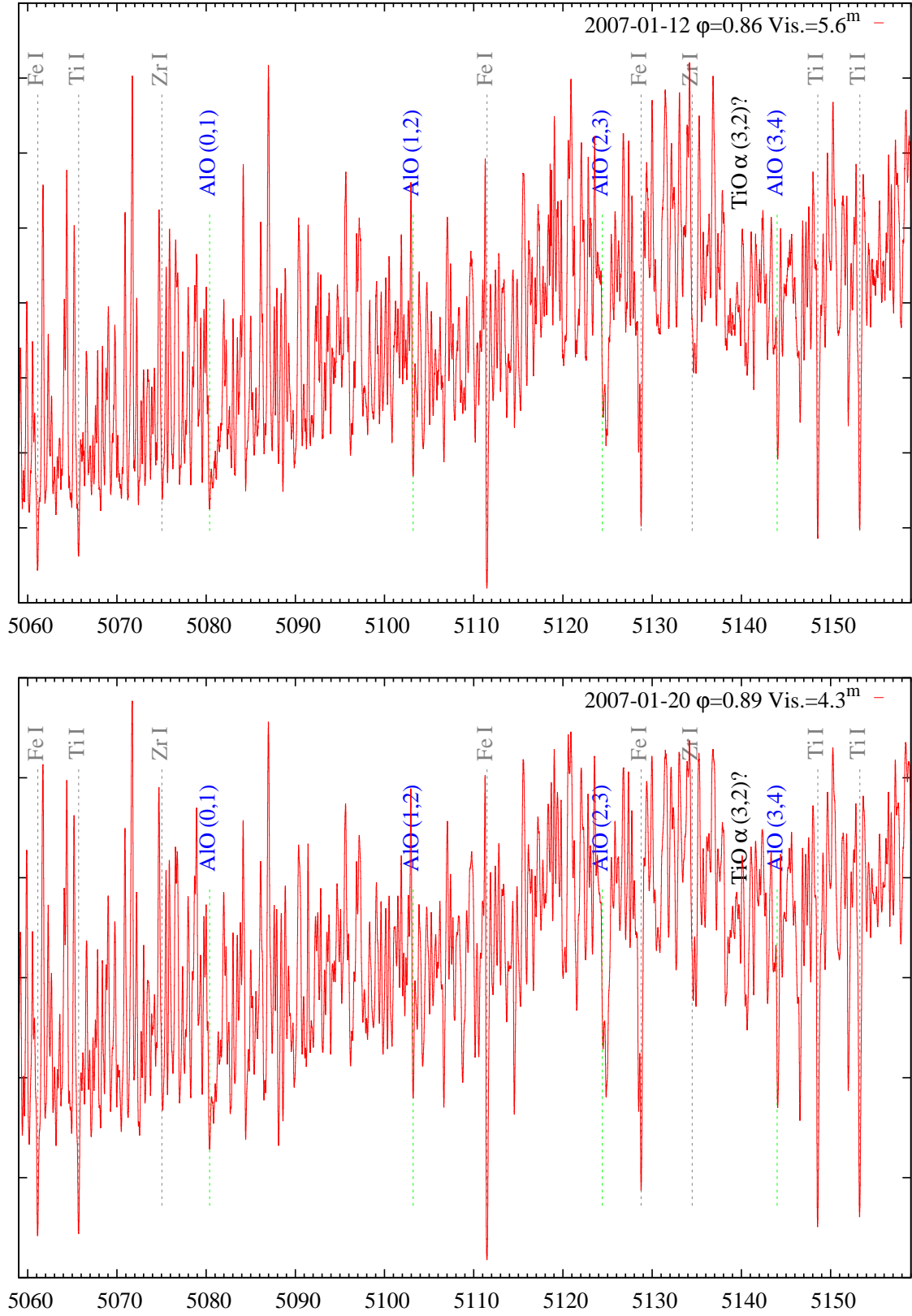


Fig. C.5. Continued.

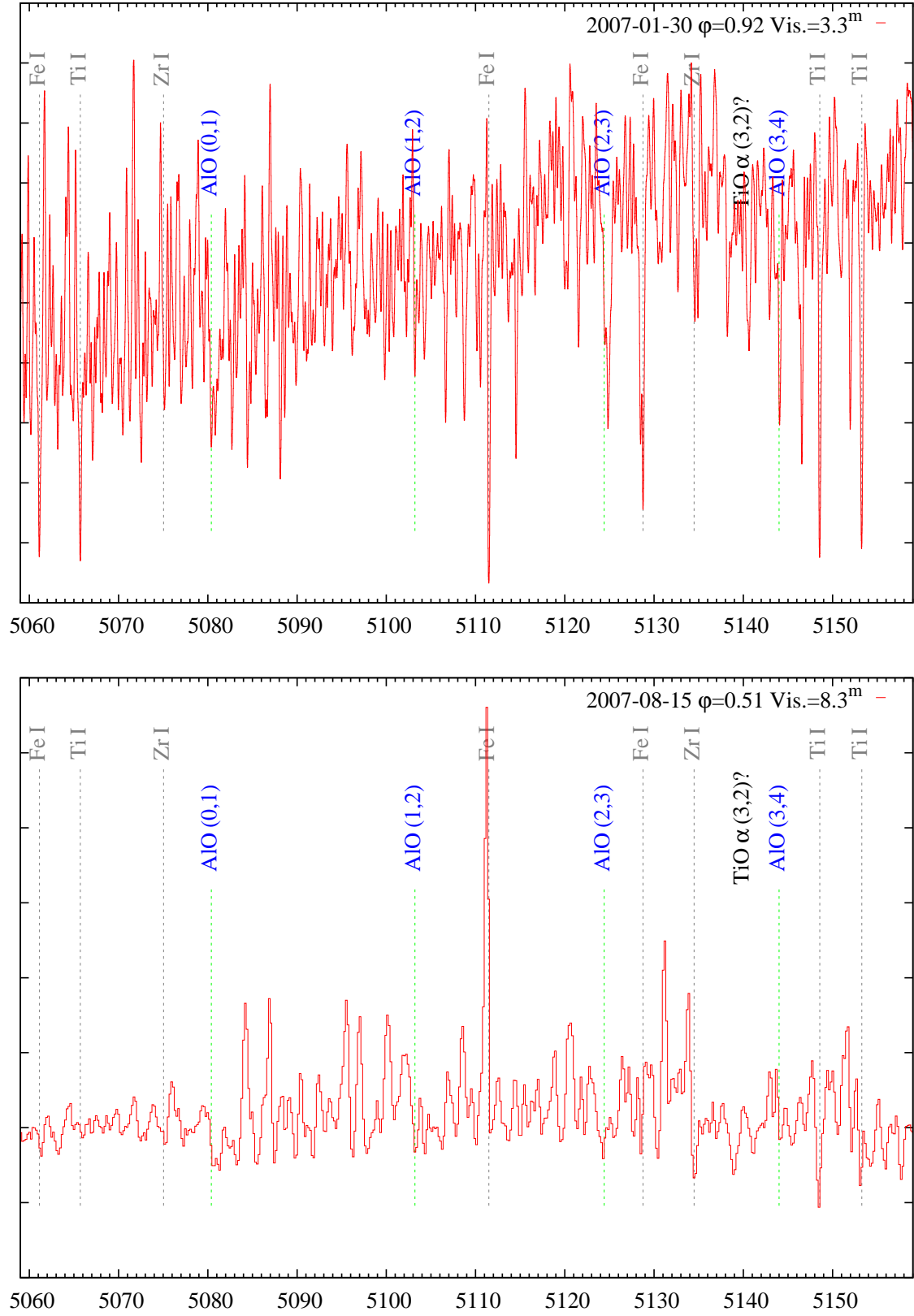


Fig. C.5. Continued.

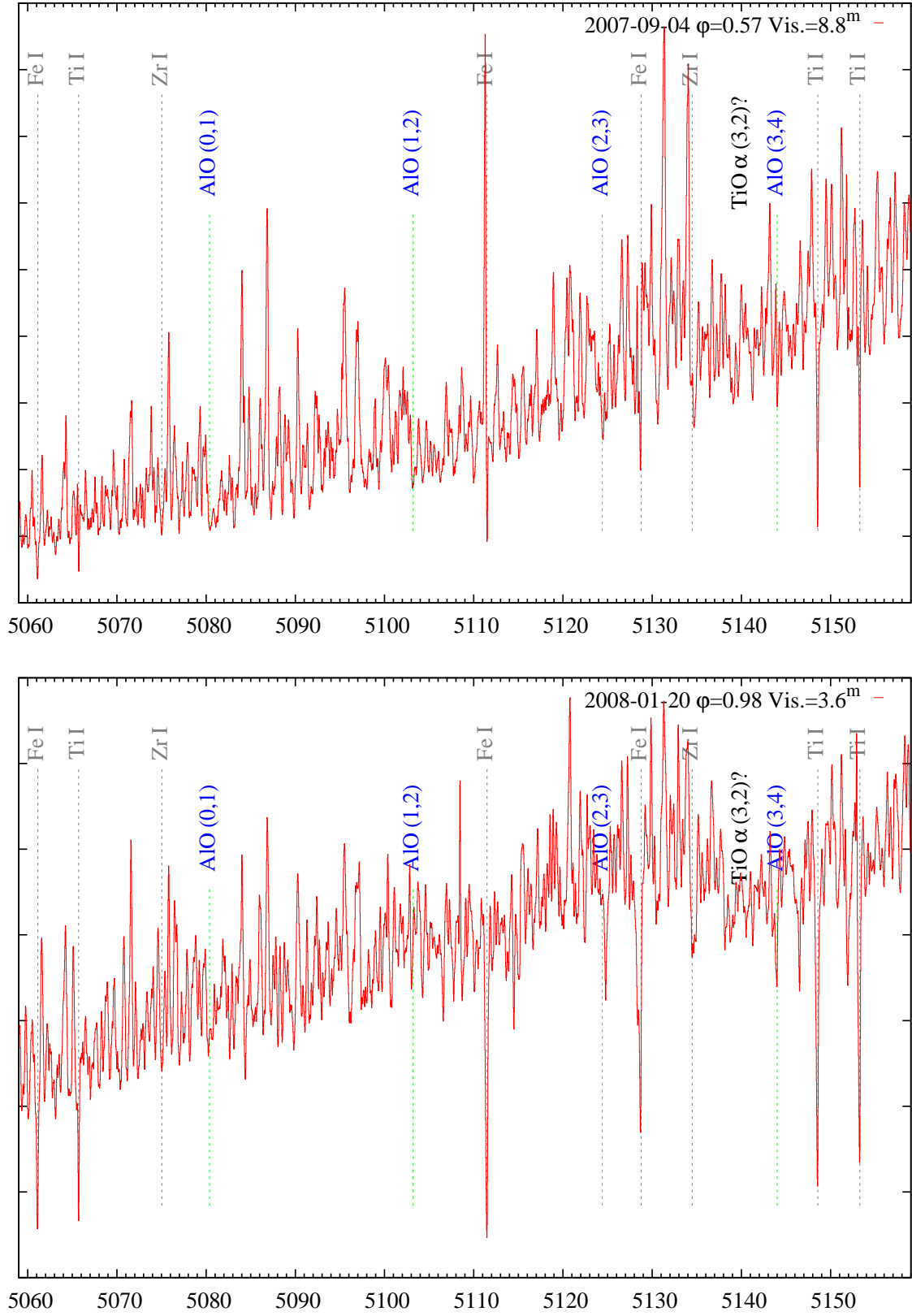
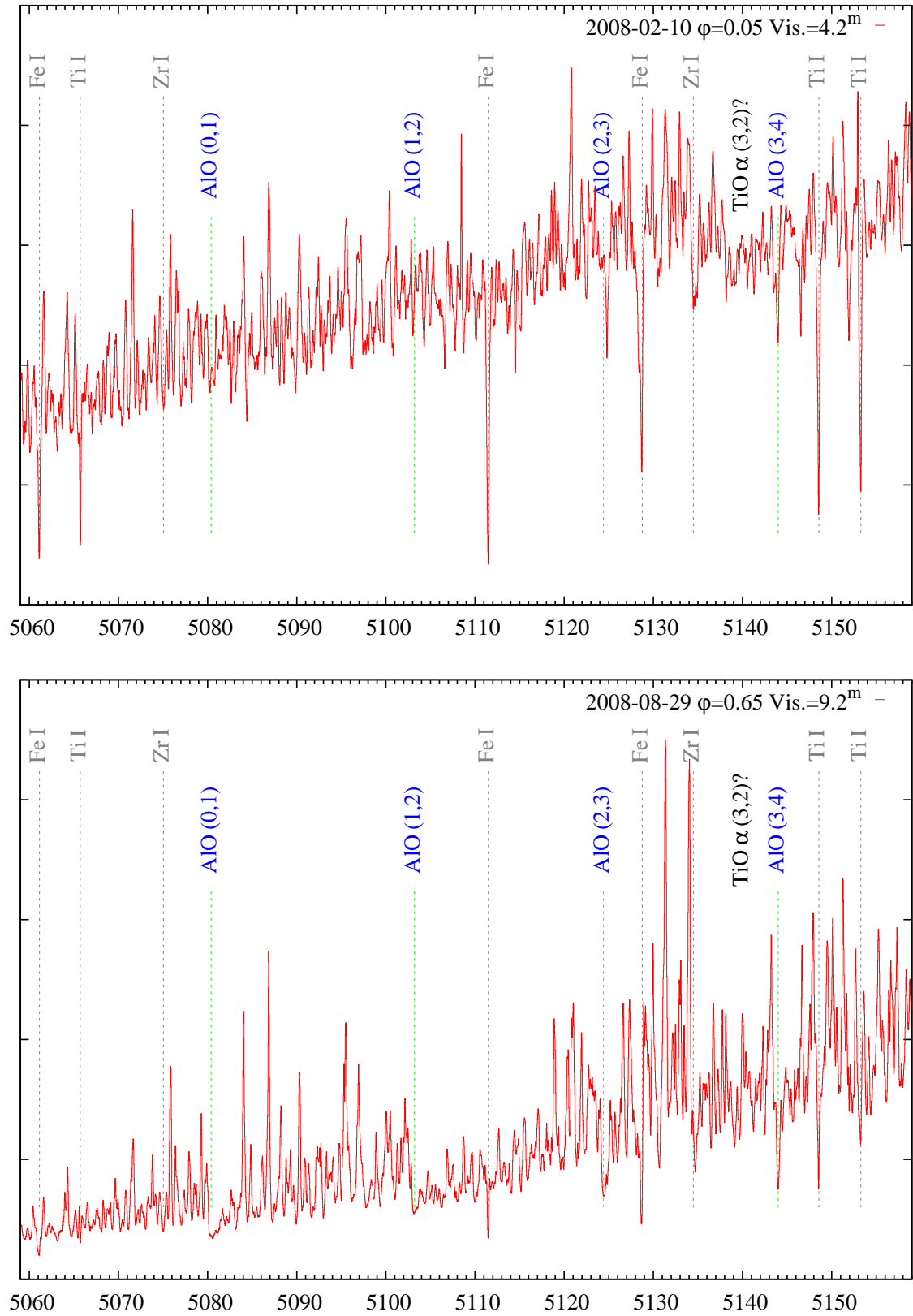


Fig. C.5. Continued.





**Fig. C.5.** Continued.

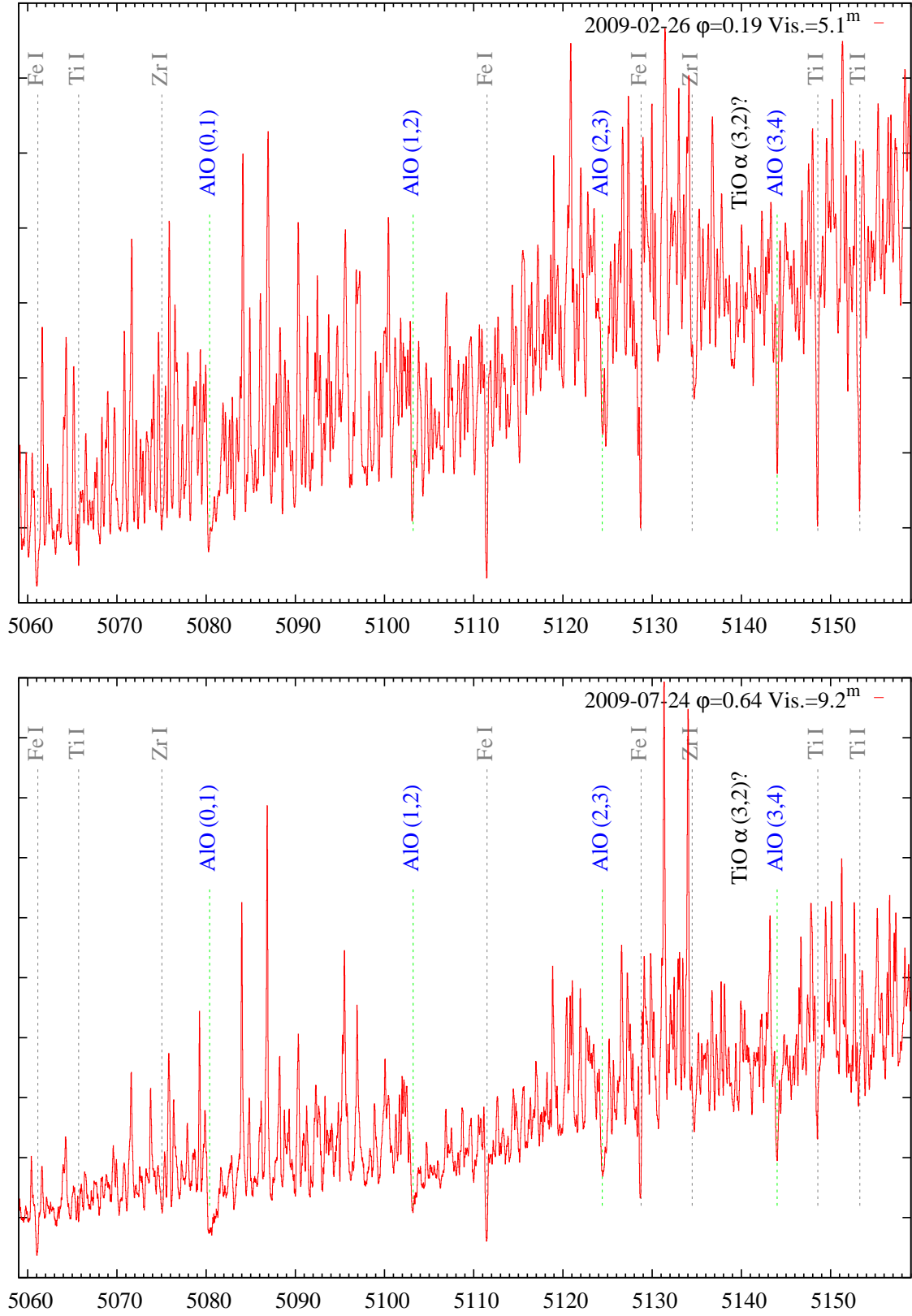


Fig. C.5. Continued.

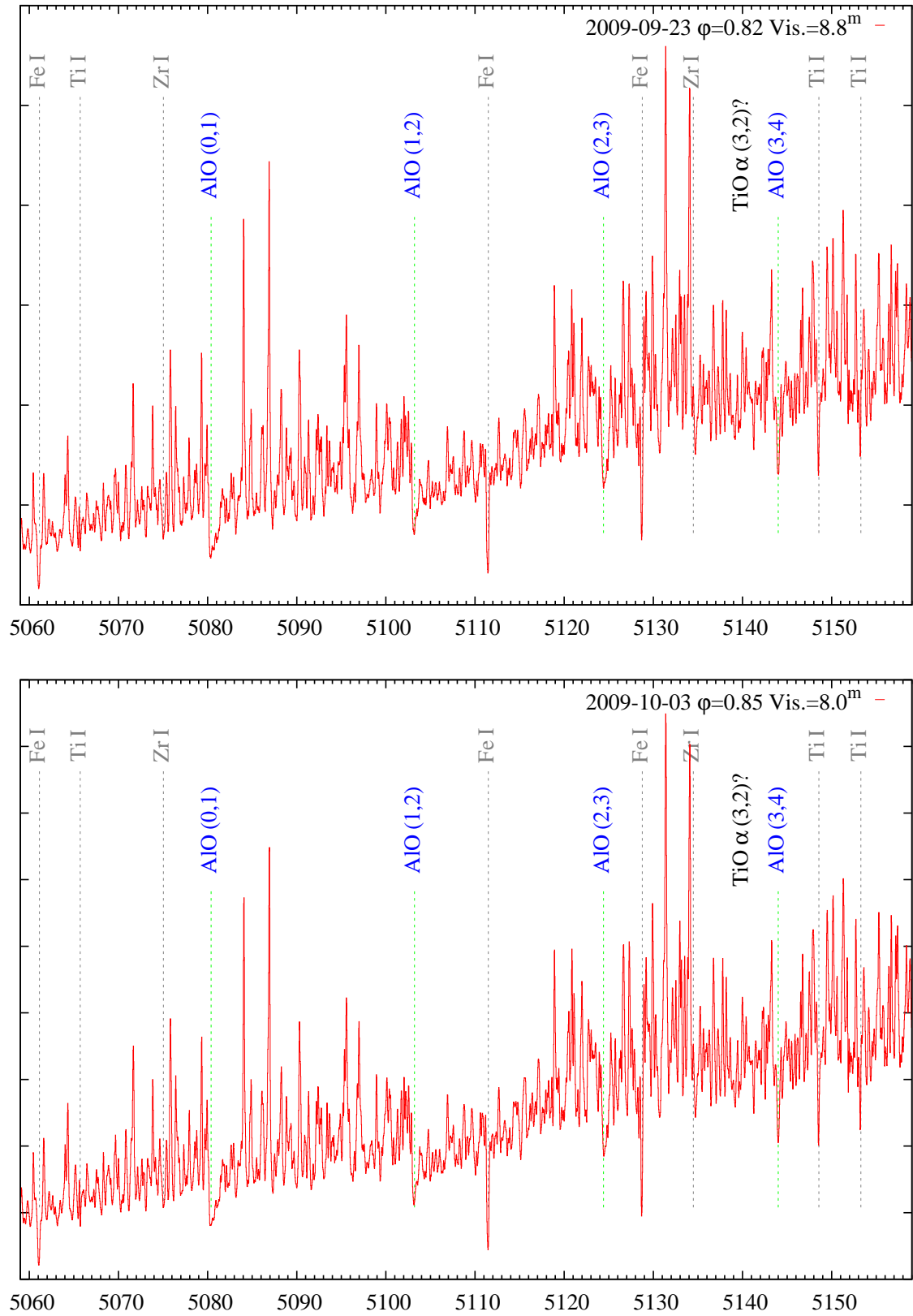


Fig. C.5. Continued.

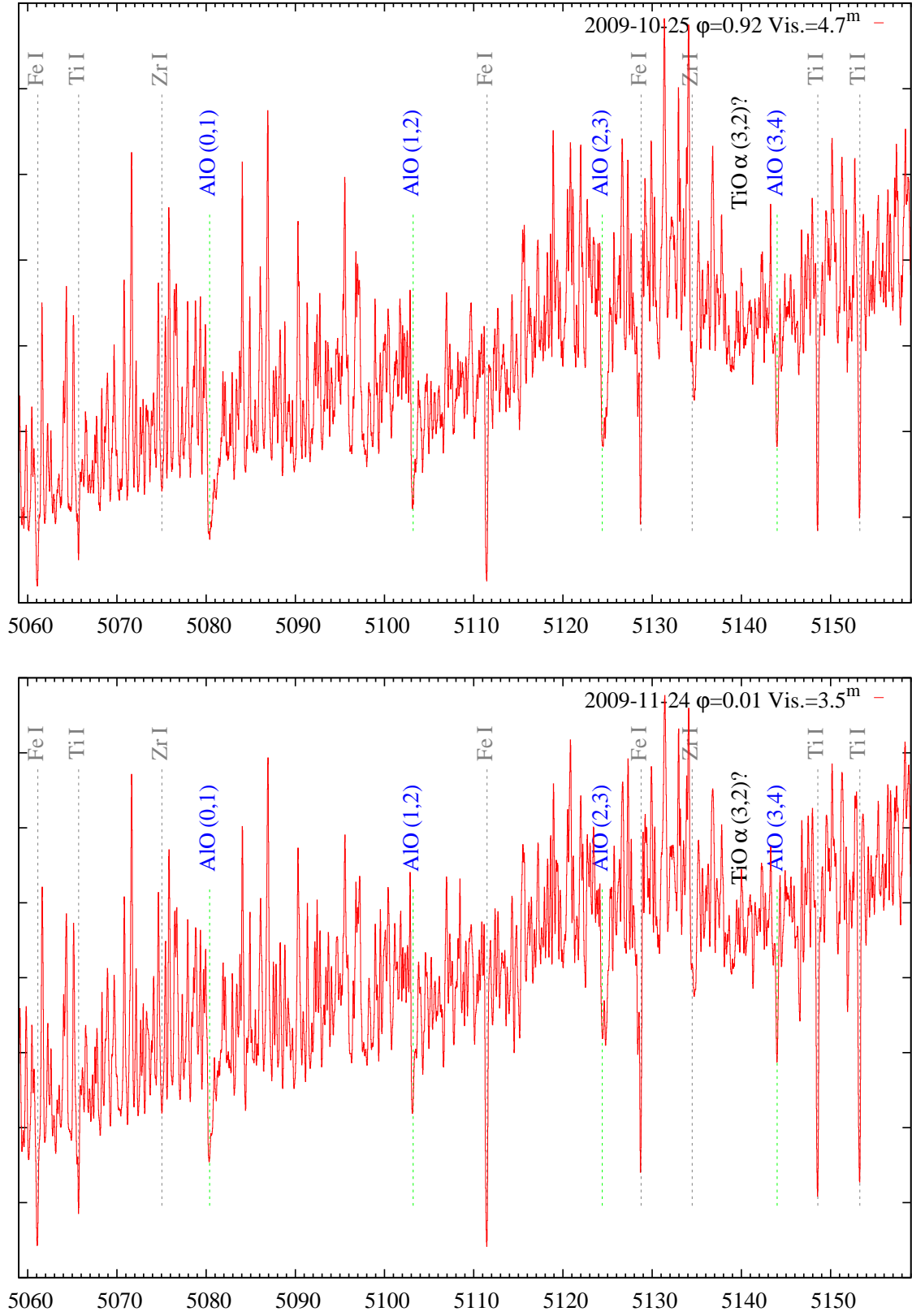


Fig. C.5. Continued.

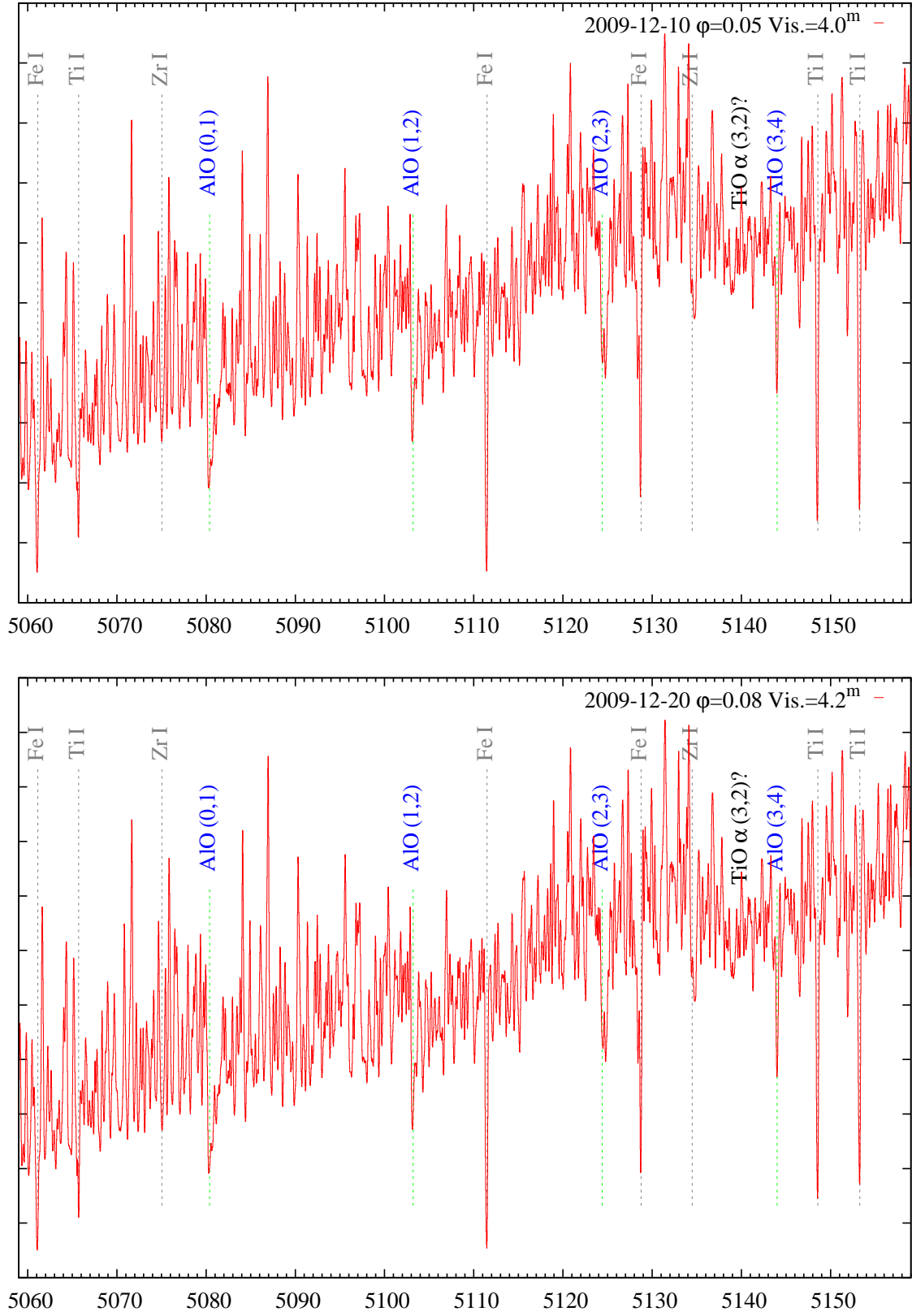


Fig. C.5. Continued.

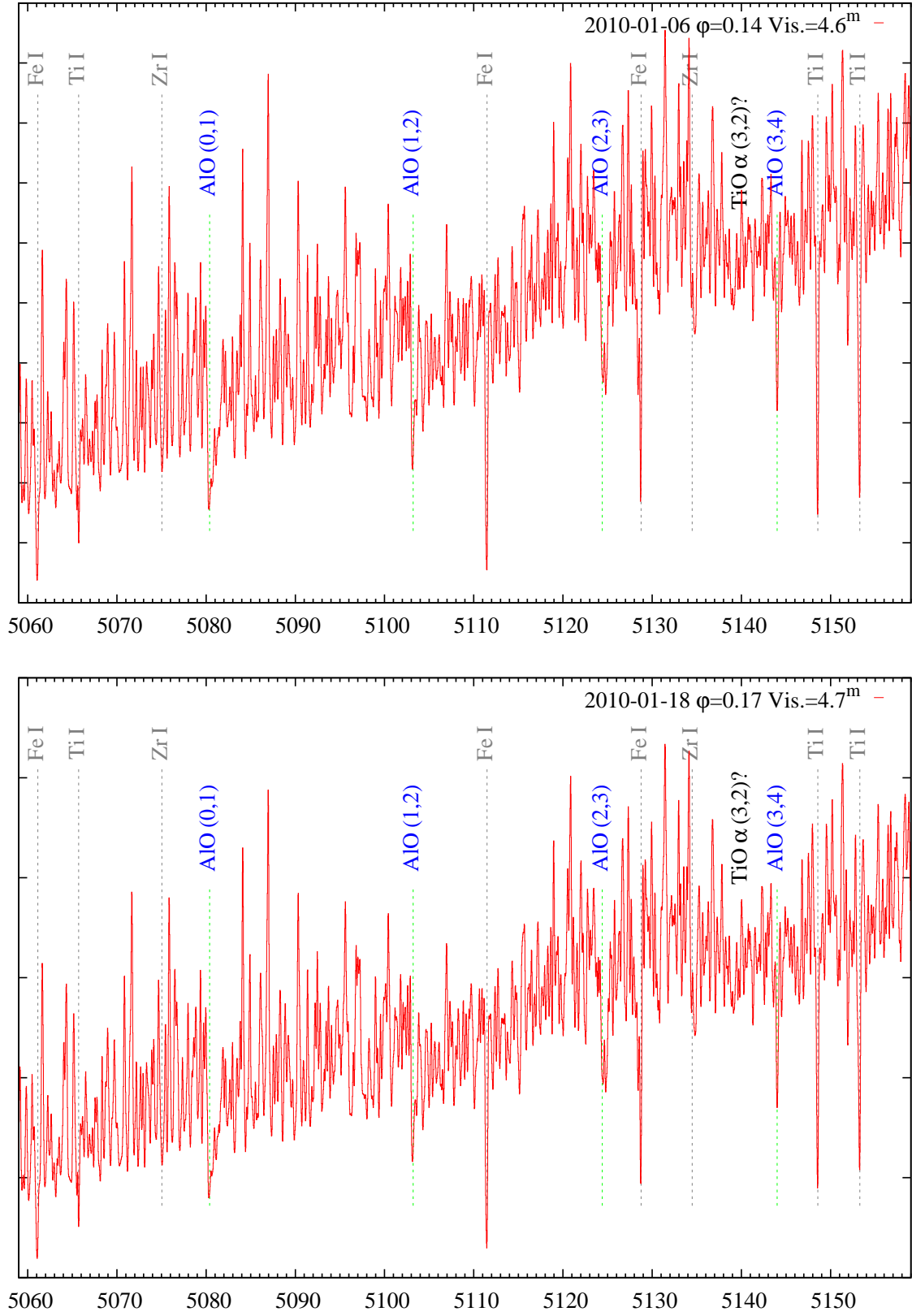


Fig. C.5. Continued.

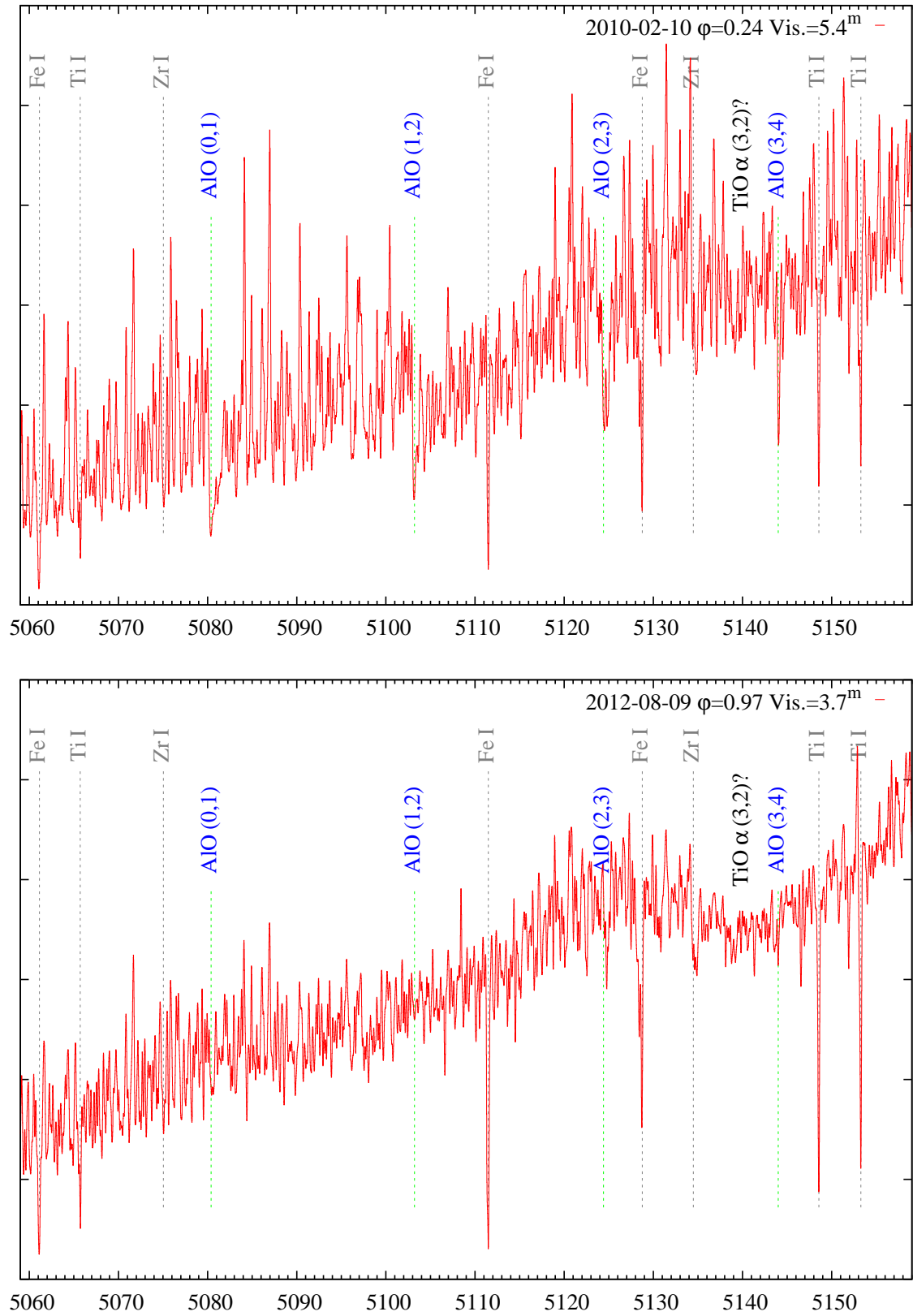


Fig. C.5. Continued.